

P
2 mix

MEASUREMENT OF SURFACE STAY TIMES
FOR PHYSICAL ADSORPTION OF GASES



A Dissertation
Presented To

the Faculty of the School of Engineering and Applied Science
University of Virginia

In Partial Fulfillment
of the Requirements for the Degree
Doctor of Philosophy in Engineering Physics

(NASA-TM-X-69001) MEASUREMENT OF SURFACE
STAY TIMES FOR PHYSICAL ADSORPTION OF
GASES Ph.D. Thesis - Va. Univ. (NASA)
143 p HC \$9.25 CSCI 201

N74-10691
Unclas
G3/26 20873

by
Richard Gordon Wilmoth
August 1973

APPROVAL SHEET

This dissertation is submitted in partial fulfillment of
the requirements for the degree of
Doctor of Philosophy in Engineering Physics

Author

Approved:

Faculty Advisor

Dean, School of Engineering
and Applied Science

August 1973

ABSTRACT

A molecular beam time-of-flight technique is studied as a means of determining surface stay times for physical adsorption. The experimental approach consists of pulsing a molecular beam, allowing the pulse to strike an adsorbing surface and detecting the molecular pulse after it has subsequently desorbed. The technique is also found to be useful for general studies of adsorption under non-equilibrium conditions including the study of adsorbate-adsorbate interactions.

The shape of the detected pulse is analyzed in detail for a first-order desorption process. For mean stay times, τ , less than the mean molecular transit times involved, the peak of the detected pulse is delayed by an amount approximately equal to τ . For τ much greater than these transit times, the detected pulse should decay as $\exp(-t/\tau)$. However, for stay times of the order of the transit times, both the molecular speed distributions and the incident pulse duration time must be taken into account.

Estimates of τ were obtained from the experimental results for Xe, Kr and CO₂ on nickel and for Xe on copper surfaces as a function of the surface temperature T_s . Xe and CO₂ were found to have mean stay times of about 10^{-5} to 10^{-3} sec over a range of T_s from 125 to 105°K. Observed

values of τ for Kr were about 10^{-5} to 10^{-4} sec in the range 99 to 92°K. The effect of He, Ar and Xe ion bombardment was to reduce the stay time for Xe on nickel by a factor of 10 to 100 at a given temperature. This is attributed to burial of neutralized ions near the surface.

Binding energies, E_0 , and preexponential factors, τ'_0 , are estimated by fitting the results to the expression $\tau = \tau'_0 \exp(E_0/kT)$. Values of τ'_0 are found to be about 10^{-17} sec in order-of-magnitude agreement with theoretically predicted values for a localized adsorption model. Values for E_0/k ranged from about 2600°K for Kr on nickel to about 3250°K for Xe on nickel.

ACKNOWLEDGMENTS

The author wishes to express his appreciation to Professor S. S. Fisher for the many helpful suggestions and criticisms received throughout this study.

Furthermore, he wishes to thank the National Aeronautics and Space Administration, Langley Research Center, who made the research program possible. In particular, the author would like to thank Mr. John P. Mugler, Jr. and Dr. L. R. Greenwood for their interest and support.

The author is indebted to Mr. Collis P. Moore, Jr. and his staff, M. G. Beasley, B. R. Emerson, Jr., C. H. Hudgins, C. D. King, J. R. Morris, and J. R. Smith for their assistance in the construction and operation of the equipment. J. R. Morris deserves special recognition for many hours spent on the experiments. In addition the author wishes to thank J. R. Nayadley, Sr. and C. C. Sibley for their innovative help with the design and assembly of the electronics.

He wishes to thank Mrs. Shirley Grice for her assistance in the preparation of the figures.

The author wishes to express his gratitude to his parents, Mr. and Mrs. Dewey E. Wilmoth, for their encouragement during all the years of his formal education.

Finally, he wishes to express special gratitude to his wife, Susan, who typed the final manuscript, and his

children, John and William, for their patience, help and understanding.

TABLE OF CONTENTS

	<u>PAGE</u>
ABSTRACT.....	iii
ACKNOWLEDGMENTS.....	v
TABLE OF CONTENTS.....	vii
LIST OF FIGURES.....	x
LIST OF TABLES.....	xii
LIST OF SYMBOLS.....	xiii
CHAPTER 1 INTRODUCTION.....	1
1.1 ADSORPTION AND STAY TIMES.....	1
1.2 STAY-TIME MEASUREMENT.....	3
1.3 THE PRESENT EXPERIMENTS.....	4
CHAPTER 2 THEORY AND BACKGROUND.....	6
2.1 THEORY.....	6
2.2 PREVIOUS EXPERIMENTS.....	12
CHAPTER 3 EXPERIMENTAL APPARATUS.....	15
3.1 MOLECULAR BEAM AND VACUUM SYSTEM... ..	15
3.2 TIME-OF-FLIGHT DETECTION SYSTEM... ..	22
3.3 TARGETS AND TEMPERATURE CONTROL... ..	24
3.4 TARGET PREPARATION.....	25
CHAPTER 4 RELATION OF DETECTOR SIGNAL TO MEAN STAY TIME FOR A FIRST-ORDER DESORPTION PROCESS.....	31
4.1 DETECTOR SIGNAL FOR A TRIANGULAR SHUTTER FUNCTION AND FIRST-ORDER DESORPTION.....	31

	<u>PAGE</u>
4.2 RELATIONSHIP BETWEEN τ AND PARAMETERS OF THE PREDICTED SIGNAL SHAPE.....	34
CHAPTER 5 EXPERIMENTAL PROCEDURES.....	39
5.1 STAY-TIME EXPERIMENTS.....	39
5.2 DATA REDUCTION.....	41
5.3 UNCERTAINTY ANALYSIS.....	47
CHAPTER 6 RESULTS.....	51
6.1 COMPARISON BETWEEN MEASURED AND PREDICTED DETECTOR SIGNAL SHAPES...	51
6.2 STAY-TIME PARAMETERS.....	57
6.3 RESULTS OF PARAMETER VARIATIONS....	60
6.3.1 Effect of Target Material for Xe Adsorption.....	60
6.3.2 Effect of Pre-Vacuum Surface Preparation for Xe Adsorption	60
6.3.3 Effect of Argon Ion Bombardment During Xe Adsorption....	63
6.3.4 Effect of Ion Bombarding Species for Xe Adsorption....	67
6.3.5 Effect of Incident Flux Variation for Xe Adsorption.....	69
6.3.6 Stay Times for CO ₂ and Kr Adsorption.....	71
6.3.7 Variation of Peak Shift with Time.....	71
6.4 BINDING ENERGY RESULTS.....	80
6.5 THE NEGATIVE DIPS IN THE DETECTOR SIGNAL.....	84

	<u>PAGE</u>
CHAPTER 7 SUMMARY AND CONCLUSIONS.....	92
BIBLIOGRAPHY.....	98
APPENDIX I PREDICTED STAY TIMES FOR ADSORBED GASES.	102
APPENDIX II CALIBRATION OF THE DETECTION SYSTEM AND CHARACTERIZATION OF THE MOLECULAR BEAM SOURCE.....	108
APPENDIX III DERIVATION OF THE EQUATIONS FOR THE SHAPE OF THE INCIDENT AND DESORPTION PULSES.....	118
APPENDIX IV TABULATION OF STAY-TIME PARAMETERS.....	127

LIST OF FIGURES

<u>FIGURE</u>		<u>PAGE</u>
3.1.1	Schematic of the Experimental Apparatus.....	16
3.1.2	Geometry of Beam-Target-Detector for Incident Beam and Stay-Time Experiments.....	17
3.1.3	Photograph of the Vacuum Chamber and Instrumentation.....	18
3.1.4	Photograph of Stay-Time Apparatus.....	19
3.1.5	Photograph of Multichannel Source.....	21
3.2.1	Schematic Diagram of the Time-of-Flight Instrumentation.....	23
3.3.1	Target Mount.....	26
3.4.1	Ion Gun.....	30
4.2.1	Predicted Detector Signals.....	36
4.2.2	Predicted Variation of Peak Shift and Time Constant with Stay Time.....	38
5.2.1	Comparison of Measured and Predicted Variation of Most Probable Time t_m with Target Temperature.....	44
6.1.1	Comparison of Measured and Predicted Detector Signals.....	52
6.2.1	Typical Variation of Measured Stay-Time Parameters with Target Temperature.....	58
6.3.1	Variation of Peak Shift with Target Temperature for Two Different Target Materials.....	61
6.3.2	Variation of Peak Shift with Target Temperature for Different Pre-Vacuum Surface Preparations.....	62
6.3.3	Variation of Peak Shift with Target Temperature with and without Argon Ion Bombardment.	64

<u>FIGURE</u>		<u>PAGE</u>
6.3.4	Variation of Peak Shift with Target Temperature for Different Ion Bombarding Species...	68
6.3.5	Variation of Peak Shift with Source Pressure	70
6.3.6	Variation of Peak Shift with Target Temperature for Different Incident Gas Species.....	72
6.3.7	Variation of Peak Shift with Time During Ion Bombardment for Different Initial Ion Dosages.....	73
6.3.8	Variation of Peak Shift with Time After Ion Bombardment for Different Background Pressures and Species.....	76
6.5.1	Comparisons of Empirical Model Predictions with Typical Detector Signals Showing Negative Dip.....	87
6.5.2	Example of Stay Time Obtained from Peak Shift Based on Empirical Model for the Negative Dip.....	90
AII.1	Variation of Detector Ion Current with Chamber Pressure.....	109
AII.2	Comparison of Measured to Predicted Incident Beam Time-of-Flight Distribution for a Single-Orifice Source.....	111
AII.3	Typical Measured Source Pressure Decay with Time Used for Multichannel Source Conductance Determination.....	115
AII.4	Comparison of Measured Incident Beam Time-of-Flight Distribution for Multichannel Source to Maxwellian Prediction.....	117
AIII.1	Comparison of Exact with Approximate Prediction for the Incident Pulse Shape.....	122
AIII.2	Predicted Shape of the Desorption Pulse for Different Ratios of Stay Time to Incident Pulse Duration Time.....	126

LIST OF TABLES

<u>TABLE</u>		<u>PAGE</u>
3.4.1	TARGET SURFACE PREPARATION STEPS.....	28
5.1.1	PARAMETERS FOR THE STAY-TIME EXPERIMENTS....	40
5.1.2	FIXED CONDITIONS FOR THE EXPERIMENTS.....	42
6.4.1	PREEXPONENTIAL FACTORS τ'_0 AND BINDING ENERGY TEMPERATURES E_0/k OBTAINED BY FITTING PEAK SHIFT DATA TO $\Delta t_s = \tau'_0 \exp(E_0/kT_s)$	81
6.4.2	BINDING ENERGY TEMPERATURES OBTAINED FROM $\Delta t_s = \tau'_0 \exp(E_0/kT_s)$ USING THEORETICAL τ'_0 BASED ON MOBILE AND LOCALIZED ADSORPTION MODELS.....	83
AIV.1	TABULATION OF STAY-TIME PARAMETERS.....	128

LIST OF SYMBOLS

A	Intercept, Eq. (5.2.1)
A_s	Surface area, cm^2
B	Slope, Eq. (5.2.1)
C	Multichannel source conductance, ℓ/sec
E_0	Binding energy per molecule, ergs
F	Flux, molecules $\cdot \text{cm}^{-2} \cdot \text{sec}^{-1}$
$f_0(v)$	Incident molecular beam speed distribution, Eq. (AIII.1)
$g(t)$	Shutter function, Eq. (AIII.2)
\hbar	Planck's constant/ 2π , erg \cdot sec
I_0	Incident beam intensity, molecules $\cdot \text{ster}^{-1} \cdot \text{sec}^{-1}$
K	Empirical parameter, Eq. (6.5.1)
Kn	Knudsen number
k	Boltzmann constant, erg/ $^\circ\text{K}$
L	Flight path length for direct beam measurements (Fig. 3.1.2), cm
\dot{Q}	Total flow rate, molecules/sec
m_g	Mass of gas molecule, gm
N	Total number of molecules
P	Probability
n	Molecular density, molecules/ cm^3
P_0	Source pressure, torr
Q	Single particle partition function
S(t)	Detector signal

T	Temperature, $^{\circ}\text{K}$
t	Time, sec
t_m	Time at which detector signal reaches maximum, sec
t_s	Effective shutter open time, sec
t_2	Time at which detector signal reaches second half-maximum, sec
t_{o1}	Most probable transit time from chopper to target, sec
Δt_s	Peak shift in detector signal, sec
V	Volume of gas-solid system
v	Molecular speed, cm/sec
x_1	Flight path length from chopper to target, cm
x_2	Flight path length from target to detector, cm
β	$= \sqrt{m_g/2kT}$, sec/cm
δ	$= \beta_o x_1$, sec
θ_D	Debye temperature of solid, $^{\circ}\text{K}$
σ	Surface coverage, molecules/cm ²
τ	Mean stay time
τ_o	Vibrational period ($=2\pi/\omega_o$), sec
τ_o'	Preexponential factor, sec
τ_2	Decay time constant of detector signal, sec
X	Peaking factor
$\omega_o, \omega_{\perp}, \omega_{\parallel}$	Vibrational frequencies of surface atoms, rad/sec

SUBSCRIPTS

a	Adsorbed
c	Critical
d	Desorbed
g	Gas
i	Incident
m	Monolayer
max	Maximum
min	Minimum
o	Source condition or condition in unperturbed molecular beam
s	Surface

SUPERSCRIPTS

tr	Translational
vib	Vibrational

CHAPTER 1

INTRODUCTION

1.1 Adsorption and Stay Times

The adsorption of molecules by solid surfaces has been the subject of a large number of investigations for many years. Molecular adsorption from the gas or liquid phase plays an important role in technical processes such as the purification of gases and liquids, dyeing of materials, and surface catalysis. Adsorption from the gas phase, in particular, is an essential mechanism for the operation of cryogenic vacuum pumps. However, adsorption is not always a desirable process. The presence of even a monolayer of adsorbed gas can sometimes lead to significant degradation of a device whose performance is strongly dependent on its surface properties, e.g., thermionic emitters and optical coatings. Designers of vehicles operating in the space environment as well as designers of ultra-high vacuum systems are especially concerned with preventing contamination of critical surfaces. Thus, a strong interest exists in the adsorptive behavior of a variety of gas-surface combinations under conditions where the adsorbate coverage constitutes one monolayer or less.

Adsorption may be defined as that process which causes

the molecular density near the surface to be higher than the density in the gas phase. Adsorption is classified according to the nature of the forces which cause it. If the adsorption is caused by weak, van der Waals forces, it is known as physical adsorption or, simply, physisorption. If the adsorption involves the transfer or sharing of electrons between the gas and solid atoms, it is then known as chemical adsorption or, simply, chemisorption. Physical adsorption is characterized by the fact that the resulting binding energies between the gas and solid are usually of the same order of magnitude as the heat of liquefaction of the gas.

Adsorption, in general, is the result of competition between the adsorption rate (rate of deposition) and desorption rate (rate of evaporation). When the adsorption rate exceeds the desorption rate, the surface coverage increases with time; conversely, when the desorption rate is greater, the surface coverage decreases. Of course, once the gas-solid system has achieved a state of thermodynamic equilibrium, the adsorption and desorption rates must be equal and the surface coverage remains constant.

The majority of experimental studies of adsorption have been carried out under conditions where the gas-solid system was allowed to reach a state of equilibrium. In most cases, the approach to equilibrium was quite rapid and adsorption

was considered to occur spontaneously⁽¹⁾. While this type of study gives useful information on equilibrium surface coverage, more information can be obtained about the adsorption history of a given molecule from non-equilibrium experiments. For example, the time and surface coverage dependence of adsorption and desorption probabilities can be determined, in principle at least, from a detailed knowledge of the adsorption and desorption rates.

One approach to obtaining the non-equilibrium information is to measure the mean stay time (sometimes called dwell time, residence time, or sticking time) that adsorbed molecules spend on the surface. The idea that a molecule striking a surface spends a finite time on the surface was first proposed by Langmuir⁽²⁾ and later was developed by Frenkel⁽³⁾ from statistical mechanics. The stay time concept has been examined at length by deBoer⁽⁴⁾ to show its usefulness in understanding both the equilibrium properties of adsorption and the mechanisms which govern the rate at which equilibrium is reached. Therefore, knowledge of the stay time is of considerable value in the study of adsorption.

1.2 Stay-Time Measurement

In order to determine the requirements for measuring

the stay time, it is necessary to examine the expected behavior. For a first-order desorption process (desorption flux proportional to surface coverage), the Frenkel model predicts that the mean stay time is proportional to $\exp(E_0/kT_s)$ where E_0 is the binding energy, k is the Boltzmann constant, and T_s is the temperature of the solid at its surface. For physisorption, where E_0 is comparable to the heat of vaporization, stay times become measurable only as the temperature approaches the liquefaction temperature of the gas which, for many gases of interest, is below room temperature. Also, based on the predicted exponential dependence, the stay time will increase rapidly with decreasing temperature. While large stay times (of the order of seconds) are more easily measured, they in turn lead to large surface coverage. Thus, if low surface coverage is of interest, stay-time magnitudes must be limited.

1.3 The Present Experiments

The purpose of the present experiments was to examine a method suited to the measurement of stay times greater than a few microseconds. The technique was one in which a thermal energy, molecular beam was pulsed and the pulse of molecules was directed onto the surface. The subsequent

desorption rate was detected and the time evolution of the detected pulse was used to infer a mean stay time. For this technique, molecular transit times were important, but they were measured as part of the experiment and their effects on the shape of the detected pulse were taken into account.

The experiments were conducted over a range of surface temperatures such that the stay time varied by at least an order of magnitude about the mean molecular transit time. Methods for estimating the stay time from the detected pulse were evaluated over this range of stay times. The effects of varying the gas species, the incident-pulse duration, the incident molecular flux, the surface material and means of preparation, and ion bombardment of the surface have been studied.

CHAPTER 2
THEORY AND BACKGROUND

2.1 Theory

As mentioned in the introduction, it was Langmuir⁽²⁾ who first proposed that a gas molecule striking a surface would spend a finite time before departing. Prior to his proposal, it was thought that a critical temperature T_c existed such that, for $T > T_c$, molecules were reflected instantaneously and, for $T < T_c$, atoms were permanently adsorbed.

The stay-time concept was first developed quantitatively by Frenkel⁽³⁾ using the methods of classical statistical mechanics. He assumed that:

- (1) an individual gas molecule is bound to a surface with energy E_0 ;
- (2) the number of molecules adsorbed is sufficiently small that interactions among themselves are negligible;
- (3) adsorbed molecules retain two translational degrees of freedom parallel to the surface;
- (4) internal degrees of freedom can be ignored;
- (5) an adsorbed molecule is bound as a simple one-dimensional harmonic oscillator vibrating

perpendicular to the surface with frequency

ω_0 (period $\tau_0 = 2\pi/\omega_0$);

(6) the gas-solid system is in thermodynamic equilibrium.

Frenkel's derived result for the mean stay time τ is:

$$\tau = \tau_0 \exp(E_0/kT) \quad (2.1.1)$$

where T is the temperature of the gas-solid system and k is the Boltzmann constant. This relation has been widely used to predict mean stay times as well as to infer values of τ_0 and E_0 from experimental observations of the temperature dependence of τ .

The physical significance of the mean stay time may be illustrated by considering the desorption of an ensemble of molecules by a first-order rate process. If σ_a is the number of molecules adsorbed per unit area at any time t and P_d is the probability of desorption per unit time, then

$$\frac{d\sigma_a}{dt} = -P_d \sigma_a \quad (2.1.2)$$

If P_d is constant, Eq. (2.1.2) may be integrated to give

$$\sigma_a(t) = \sigma_a(0) \exp(-P_d t) \quad (2.1.3)$$

The mean stay time for the ensemble is

$$\tau \equiv \left| \frac{1}{\sigma_a(0)} \int_0^{\infty} t \left(\frac{d\sigma_a}{dt} \right) dt \right| \quad (2.1.4)$$

Substituting for $\sigma_a(t)$ from Eq. (2.1.3) and integrating yields

$$\tau = 1/P_d \quad (2.1.5)$$

This interpretation of the mean stay time is usually valid as long as the surface coverage is much less than a monolayer. At higher surface coverages, adsorbate-adsorbate interactions become significant and the process is no longer first order. In this case, a mean stay time is still defined by Eq. (2.1.4), but it is meaningful only when the coverage history is also specified.

Although the Frenkel relation, Eq. (2.1.1), is widely used, more general predictions of theoretical stay times have been presented by deBoer^(4,5). The initial development of these predictions is similar to that of Frenkel and follows directly from consideration of steady-state conditions, i.e., where the desorption rate equals the adsorption rate. If F_i is the incident flux and P_a is the

adsorption probability (sometimes called sticking probability), it follows for first-order desorption that

$$\sigma_a = P_a F_i \tau \quad (2.1.6)$$

The flux F_i is usually known from the state of the system (e.g., temperature and pressure). For example, for a gas in equilibrium with the surface, the kinetic theory of gases predicts

$$F_i = n_g \left(\frac{kT}{2\pi m_g} \right)^{\frac{1}{2}} \quad (2.1.7)$$

for a gas of number density n_g and molecular mass m_g . Substituting this into Eq. (2.1.6) and solving for τ , one obtains

$$\tau = \frac{1}{P_a} \left(\frac{2\pi m_g}{kT} \right)^{\frac{1}{2}} \frac{\sigma_a}{n_g} \quad (2.1.8)$$

For a system of volume V and adsorbing surface of area A_s ,

$$\frac{\sigma_a}{n_g} = \frac{V}{A_s} \left(\frac{N_a}{N_g} \right) \quad (2.1.9)$$

where N_a and N_g are the total number of molecules in the adsorbed phase and gas phase, respectively. Eq. (2.1.8) can then be written as

$$\tau = \frac{1}{P_a} \left(\frac{2\pi m_g}{kT} \right)^{\frac{1}{2}} V \frac{1}{A_s} \left(\frac{N_a}{N_g} \right) \quad (2.1.10)$$

This relation provides a convenient starting point for the prediction of τ by the methods of equilibrium statistical mechanics.

The evaluation of τ from Eq. (2.1.10) has been treated by deBoer⁽³⁾ using classical statistical mechanics. The results for mobile and localized adsorption are of particular interest. Mobile adsorption refers to the case where molecules are bound to the surface but move freely in directions parallel to the surface. Localized adsorption refers to the case where molecules are bound so strongly in local sites that their translational motion parallel to the surface is negligible. The development for these two cases is given in Appendix I, and a simple extension of deBoer's approach is proposed which includes some quantum-mechanical effects.

For a mobile adsorbed gas, the result is

$$\tau = \frac{\theta_D/4T}{\sinh(\theta_D/4T)} \tau_o \exp(E_o/kT) \quad (2.1.11)$$

where θ_D is the Debye temperature of the solid. In the high-temperature limit ($T \gg \theta_D$), Frenkel's result is obtained. However, for $T < \theta_D$, the predicted values for τ are substantially less than those predicted by the Frenkel expression.

The result for localized adsorption is given by

$$\tau = \frac{4\pi h^2 \sigma_m}{m_g k \theta_D} \frac{(\theta_D/2T)^2}{[2\sinh(\theta_D/4T)]^3} \tau_o \exp(E_o/kT) \quad (2.1.12)$$

where σ_m is the monolayer surface coverage and $2\pi h$ is Planck's constant. The high-temperature limit for this expression is of course altogether different from the Frenkel expression.

The quantitative differences in stay times predicted by Eqs. (2.1.11) and (2.1.12) may be illustrated by writing these equations in the form

$$\tau = \tau_o' \exp(E_o/kT) \quad (2.1.13)$$

Thus, for a given binding energy and temperature, one need only investigate the behavior of the preexponential factor τ'_0 . Sample calculations given in Appendix I for xenon on nickel at 100°K show that τ'_0 for mobile adsorption is only slightly less than τ_0 , both being of the order of 10^{-13} sec. However, for localized adsorption, τ'_0 is of the order of 10^{-17} sec. Therefore, stay times are expected to depend considerably on the type of adsorption process.

The general form of Eq. (2.1.10) allows a natural extension of the theory to include such effects as restriction of internal and rotational degrees of freedom as well as a more exact quantum-mechanical treatment of bound states⁽⁶⁻⁹⁾.

An analysis of first-order non-equilibrium adsorption has been carried out by Pagni⁽¹⁰⁾ using a classical molecular collision model and non-equilibrium statistical mechanics. His results for steady-state adsorption point out the explicit dependence of τ'_0 on the binding energy. While the time-dependent case is also formulated, no solutions for τ are presented.

2.2 Previous Experiments

A number of stay-time measurements have been made prior to the present work. Clausing⁽¹¹⁾, in the first

attempt to measure stay times, directed a stream of Cd vapor onto a rotating disk maintained at a constant temperature. The atoms then desorbed and were collected by a condensation plate. It was expected that the mean stay time could be inferred from the angular displacement of the condensate. However, the stay times encountered in these experiments were less than the time-resolution of the apparatus ($\sim 10^{-6}$ sec). Clausing later devised a technique where the time for a gas pulse to diffuse through a capillary tube⁽¹²⁾ was measured. Stay times as large as $\sim 10^{-3}$ sec were measured for Ar, Ne and N₂ on glass. Recent experiments of this same general type have been conducted for He on Cu near liquid helium temperature⁽¹³⁾.

Recent measurements of stay times have mainly involved the use of modulated molecular beams⁽¹⁴⁻²²⁾. Most of these studies⁽¹⁶⁻²²⁾ have been conducted for chemisorbed gases. For all such measurements, a molecular beam is interrupted in some manner by a shutter prior to striking the surface of interest. If the shutter is opened (or closed) in a time that is short compared to the stay time, the desorption rate is that for a step-like increase (or decrease) in the deposition rate. If the beam is pulsed (shutter opened and closed) and if the pulse time-width is small compared to the stay time, then the desorption rate is that for an instantaneously deposited ensemble. For either type of fast

shutter behavior, the desorption rate for a first-order process is simply a function of the mean stay time. Otherwise, the desorption rate depends on the deposition history. Also, if shutter-to-surface transit times are not negligible, they must be taken into account. The desorbing molecules are usually detected by some sort of flux- or density-sensitive detector placed in the desorption path. If surface-detector transit times are not small compared to times of interest, then these too must be taken into account. In only two of these studies^(15, 20) were shutter duration and transit-time effects evaluated in detail. In the other cases, they were either negligible or were accounted for approximately.

Stay times have also been measured by the technique commonly known as flash desorption. The technique and its results have been reviewed by Ehrlich⁽²³⁾. Although it is used primarily for determining binding energies, it has been used to estimate chemisorption stay times. The disadvantage of this technique is that the temperature dependence of the stay time must be known a priori.

Physisorption stay times have not been studied nearly so thoroughly as those for chemisorption. This is due in large part to the experimental difficulties. The present study investigates these difficulties and, under selected conditions, resolves them to a point where meaningful data are obtained.

CHAPTER 3

EXPERIMENTAL APPARATUS

In this chapter, the molecular-beam and vacuum system, the time-of-flight detection system, and the target and target preparation techniques are described. The arrangement of the various components is shown schematically in Fig. 3.1.1. The geometry of the beam-defining elements and the time-of-flight (TOF) detection system is shown in Fig. 3.1.2. The vacuum system and instrumentation and the stay-time apparatus are further described by the photographs of Figs. 3.1.3 and 3.1.4.

3.1 Molecular Beam and Vacuum System

The experiments were conducted in a stainless-steel vacuum chamber evacuated by a liquid-nitrogen-trapped, oil-diffusion pump. The chamber pressure was typically 2×10^{-8} torr with no molecular-beam flow and about 2×10^{-7} torr with the beam on. (All test chamber pressures reported herein were measured using an ionization gauge calibrated for nitrogen, and the quoted values are as-read gauge values.)

High-purity (nominally 99.995%) gas was inlet to the molecular beam source chamber through a variable leak valve.

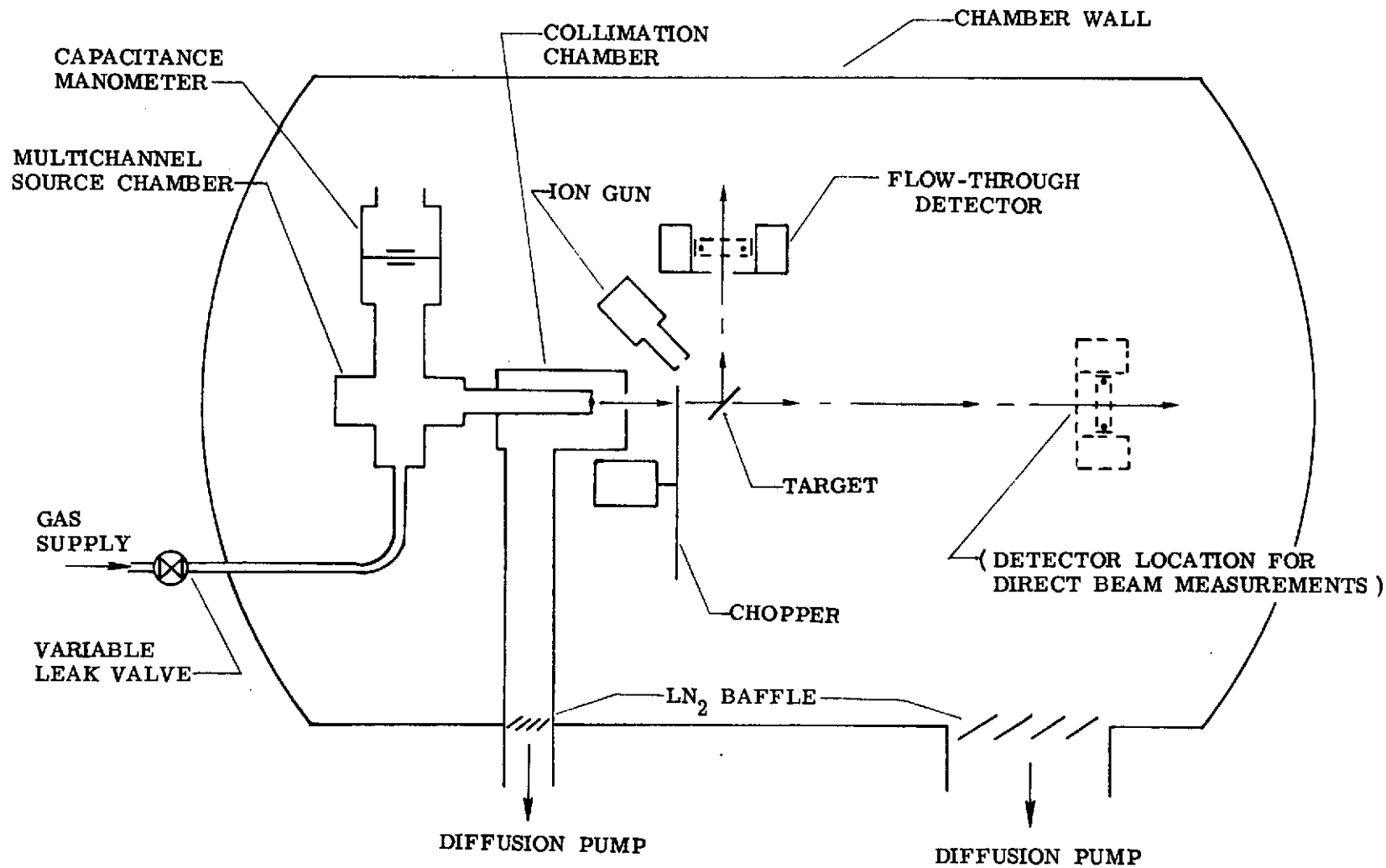
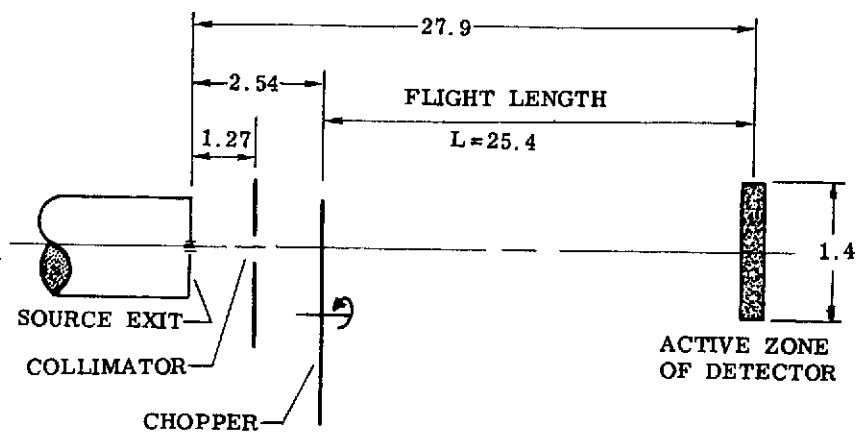
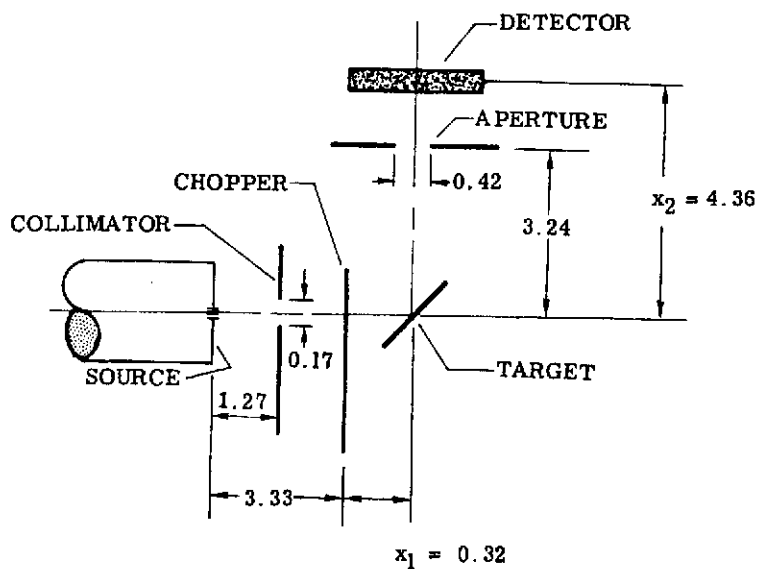


Figure 3.1.1 Schematic of the Experimental Apparatus



DETECTOR POSITION A

(All dimensions in centimeters)



DETECTOR POSITION B

Figure 3.1.2 Geometry of Beam-Target-Detector for Incident Beam and Stay-Time Measurements

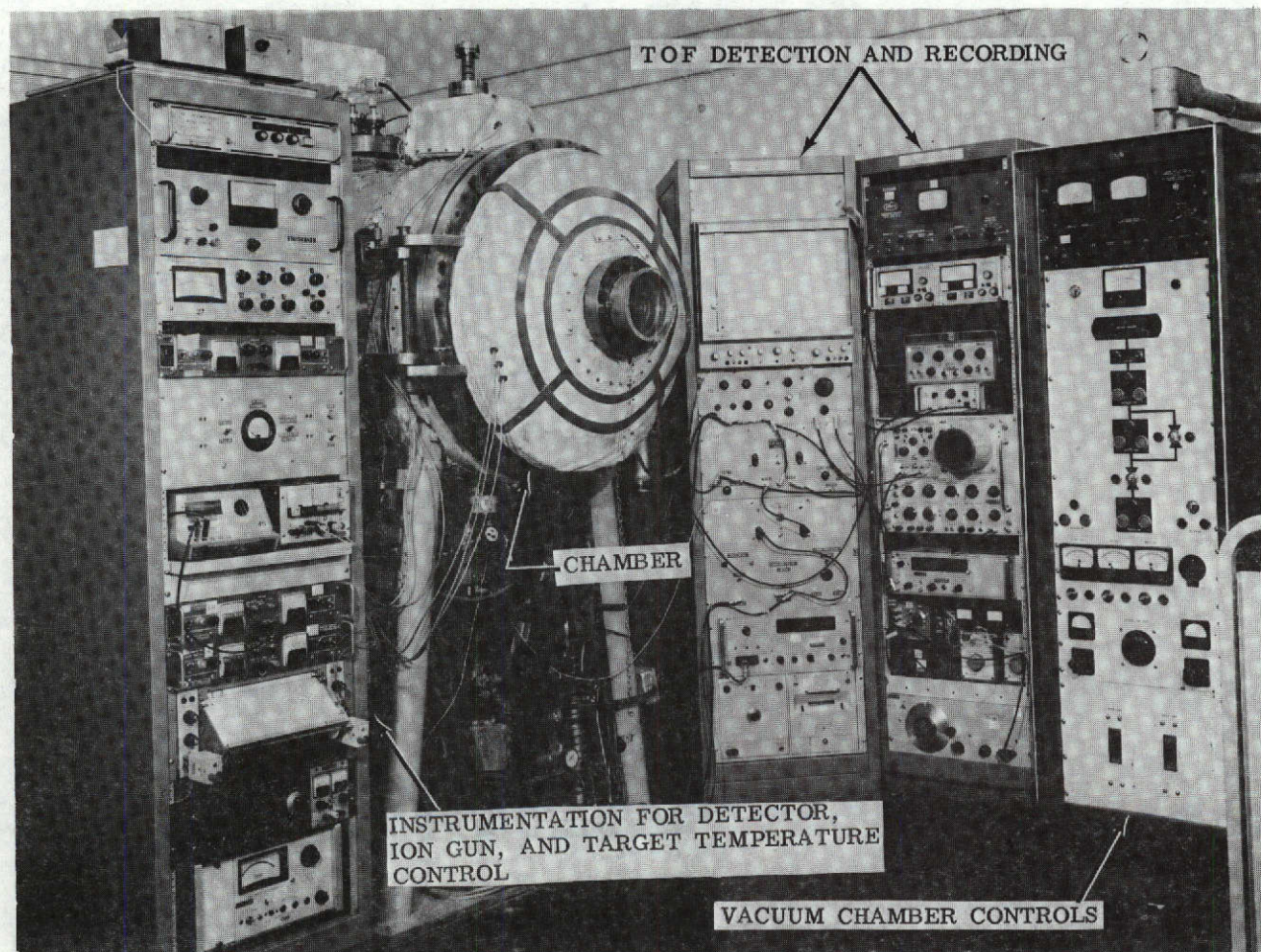


Figure 3.1.3 Photograph of the Vacuum Chamber and Instrumentation

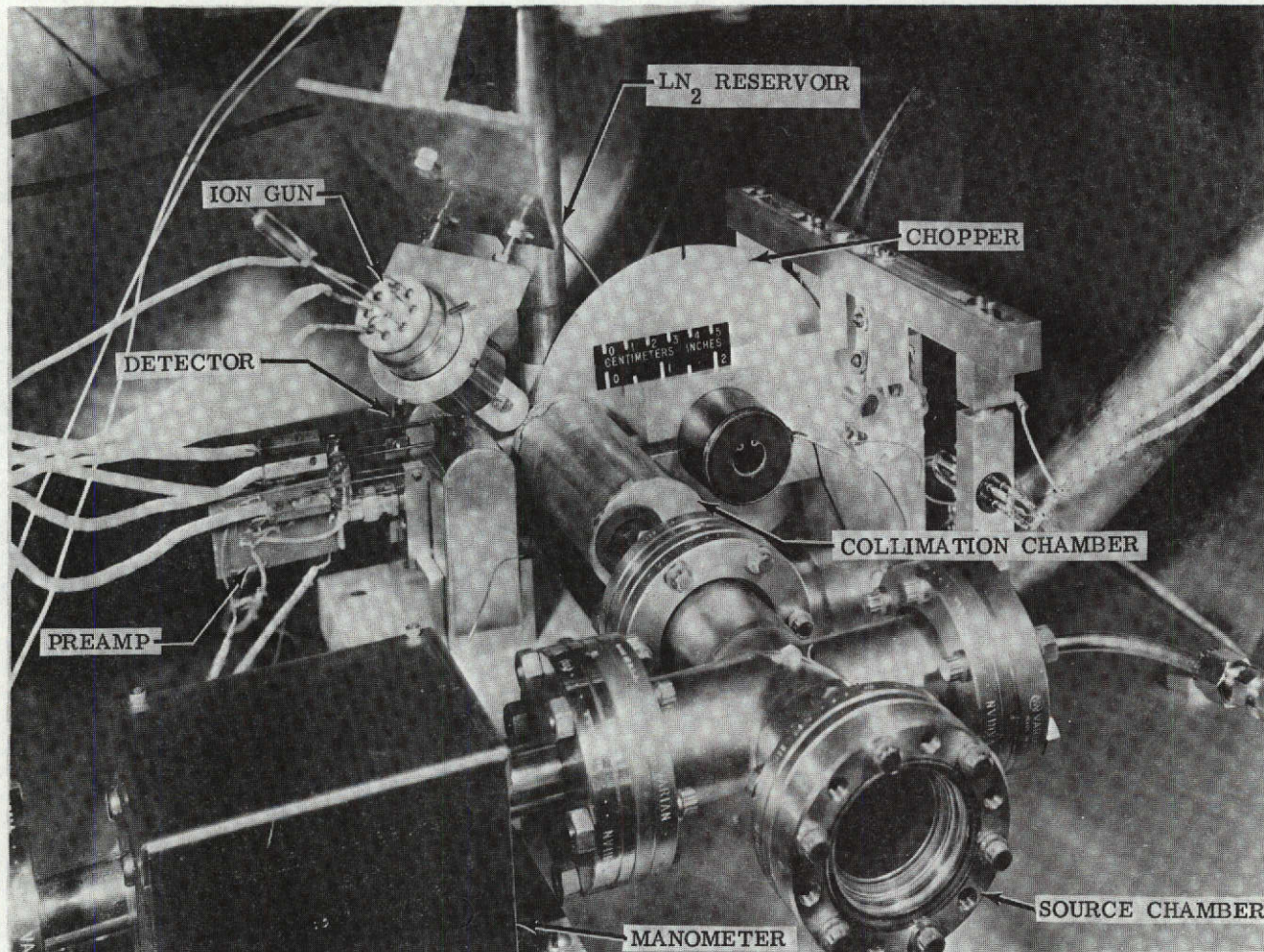


Figure 3.1.4 Photograph of Stay-Time Apparatus

The source chamber was maintained at ambient temperature ($\approx 295^\circ\text{K}$) and the source-chamber pressure p_0 was measured with a capacitance-type electronic manometer.

The molecular beam was formed by a multichannel source, a photograph of which is shown in Fig. 3.1.5. This source is composed of a large number ($\approx 1.7 \times 10^4$) of quartz capillary tubes fused into an array and in turn fused in the center of the end plate of a 1.9 cm diameter glass tube. Each individual channel has a nominal diameter of 5×10^{-4} cm and a length of 0.15 cm. The channels are assembled in a hexagonal pattern with a nominal overall diameter of 0.1 cm. The molecular beam thus formed is then collimated by an orifice as shown in Fig. 3.1.2.

The characteristics of the molecular beam formed by this source were the subject of a separate investigation⁽²⁴⁾ and are described in some detail in Appendix II. From measurements of the beam centerline flux and speed obtained in that study (with the detector in position A of Fig. 3.1.2), the flux and energy of the beam striking the target (as shown by position B of Fig. 3.1.2) can be estimated. For example, for Xe gas with $p_0 = 10$ torr, the intensity of the beam at the target is estimated to be 3.4×10^{15} atoms $\cdot \text{cm}^{-2} \cdot \text{sec}^{-1}$. The measured mean energy per atom for Ar was about 0.064 eV (some 25% higher than that for an effusive beam at the source temperature); Xe is expected to

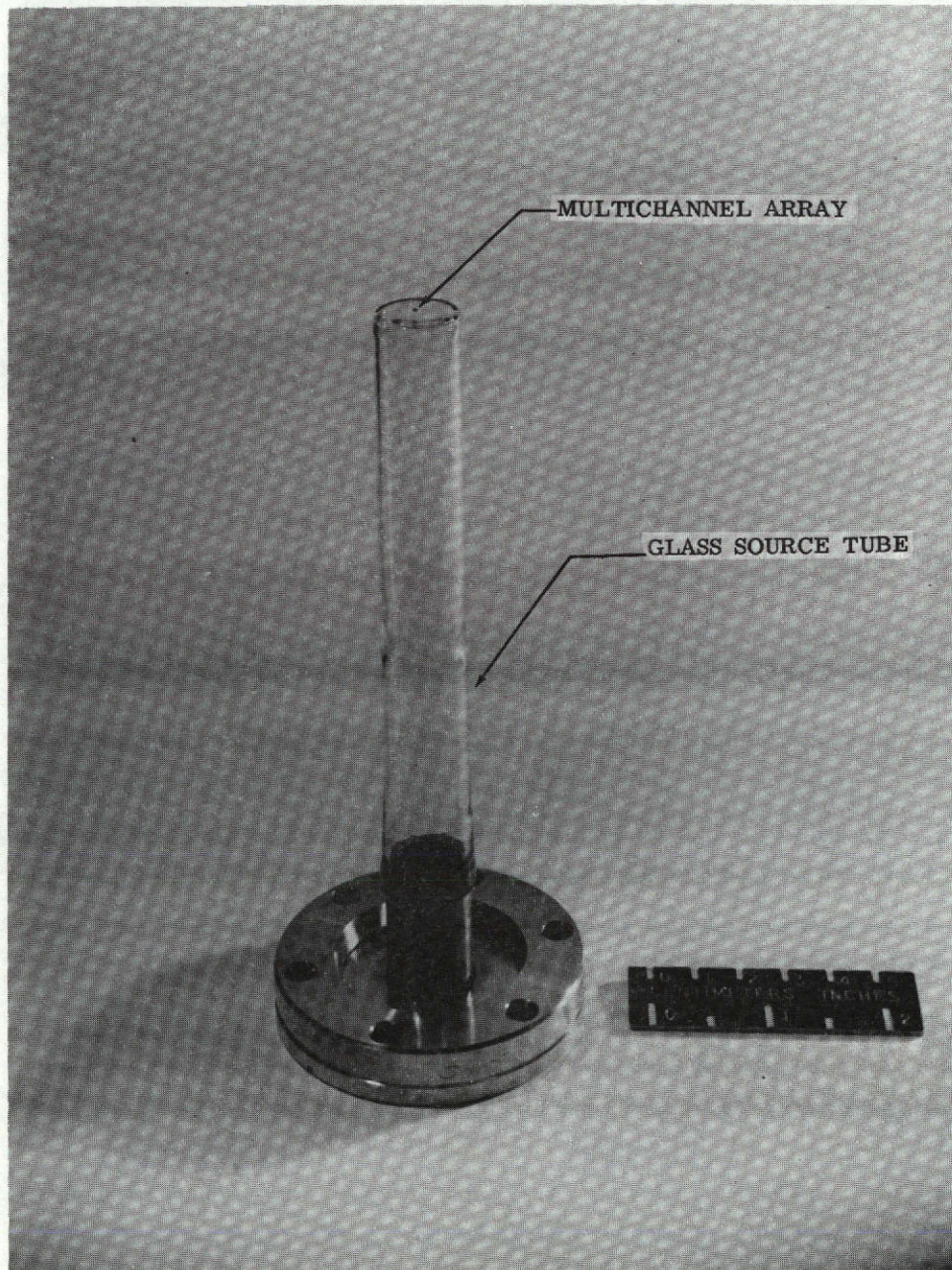


Figure 3.1.5 Photograph of Multichannel Source

have the same mean energy as Ar since Ref. (24) indicates that, for the source pressures used in the present experiments, the multichannel source is operating in the limit of isentropic expansion. Although the angular distribution of beam flux was not measured, based on Ref. (25), it is estimated that 75% of the molecules diverged less than $\pm 6^\circ$ from the beam axis. For completely free molecular flow through the beam defining elements, the maximum beam divergence should not exceed $\pm 4^\circ$.

3.2 Time-of-Flight Detection System

The time-of-flight (TOF) detection system was designed after that of Hagen, Scott and Varma⁽²⁶⁾ and is shown schematically in Fig. 3.2.1. The system includes a chopper, a detector, and detector signal processing instrumentation. The chopper is a thin 15.2 cm diameter disk with 0.16 cm radial slots cut 0.64 cm deep at 90° intervals around its periphery and is driven by a synchronous motor. For the stay-time experiments, the chopper rotational speed is held constant at about 1200 rpm. Direct beam speed distributions were determined at a chopper speed of about 3000 rpm to obtain reasonable time-of-flight resolution⁽²⁶⁾. As a slot passes across the molecular beam, a molecular pulse passes through and the "start time" for this pulse is sensed by a

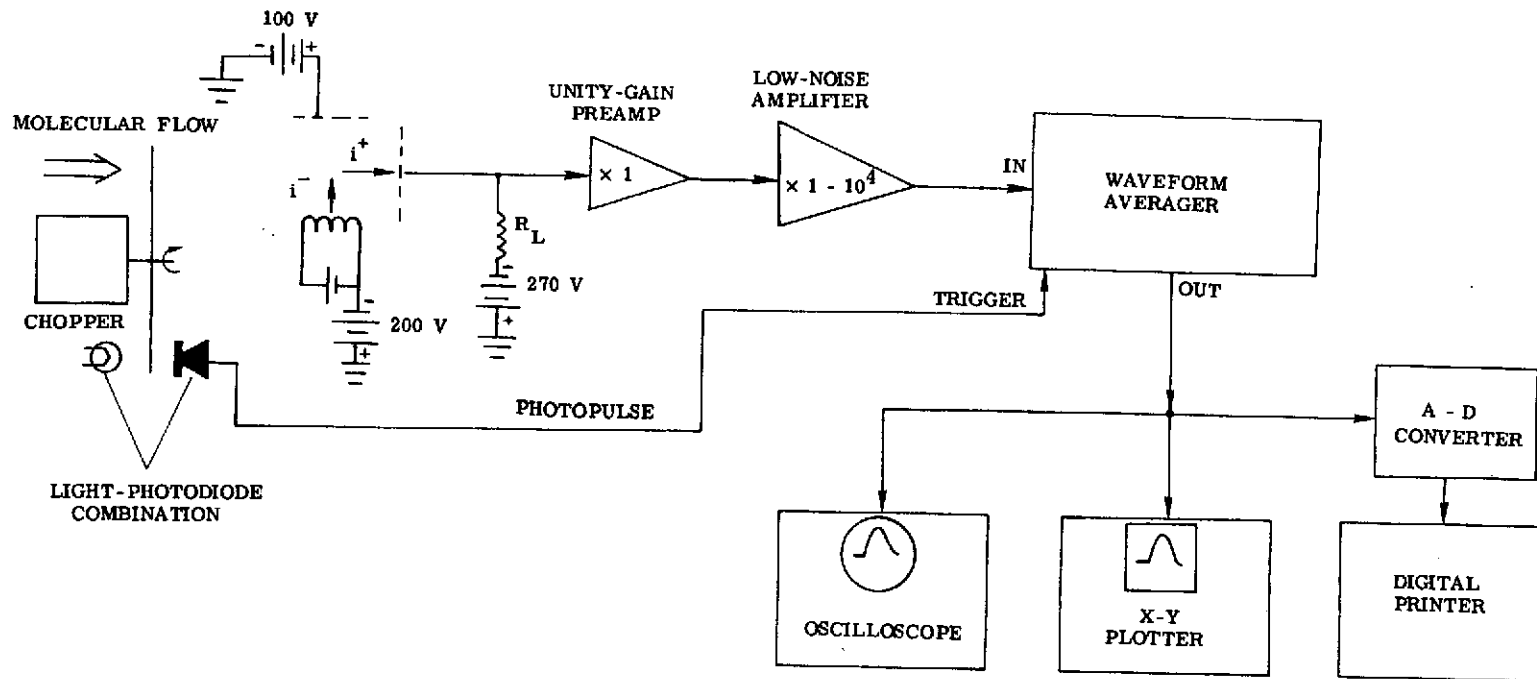


Figure 3.2.1 Schematic Diagram of the Time-of-Flight Instrumentation

light-photodiode combination located diametrically opposite the molecular beam. For analyzing the direct beam, the pulse travels directly to a flow-through type ionization detector as shown by Position A of Fig. 3.1.2. For stay-time measurements, the pulse first travels to a target and then to the detector as shown by Position B. The signal from the ionization detector, proportional to instantaneous number density within its active zone, is amplified and then fed into a signal averager. The averager divides the signal into 100 consecutive channels of equal time width and averages the signal over many pulses to improve the signal-to-noise ratio. The averaged signal is then recorded in analog and/or digital form.

The time evolution of the detector signal depends on the initial shape of the pulse, the speed distribution of beam molecules, the experimental geometry, and for stay-time measurements, the distribution of molecular stay times on the surface and the speed distribution of molecules leaving the surface. The dependence of the signal shape on these factors is analyzed in Chapter 4.

3.3 Targets and Temperature Control

Three targets were employed. One was high purity (99.999%) copper and two were high purity (99.995%) nickel.

Each was 0.64 cm diam x 0.16 cm thick and was mounted on a copper holder as shown in Fig. 3.3.1. The copper holder was attached to a liquid-nitrogen-filled reservoir by means of a boron nitride spacer. This spacer electrically insulated the target (to allow measurement of the ion current during ion bombardment) and still provided adequate thermal conductance for cooling the target. A tungsten filament was inserted inside the holder to allow heating of the target and was electrically insulated from the holder by a ceramic tube. A chromel-constantan thermocouple was mounted on the holder just below the target for measuring the target temperature. The output of this thermocouple was recorded on a continuous recording potentiometer and was also used in a feedback loop to control the voltage across the heater filament and thereby control the target temperature. With this arrangement, the target temperature could be varied from 90°K to 450°K and could be maintained constant within $\pm 0.5^{\circ}\text{K}$.

3.4 Target Preparation

All targets were first polished to a mirror finish, following standard metallurgical practice, finishing with No. 600 diamond paste. The Cu target and one Ni target (hereafter referred to as Ni A) were then cleaned by rinsing

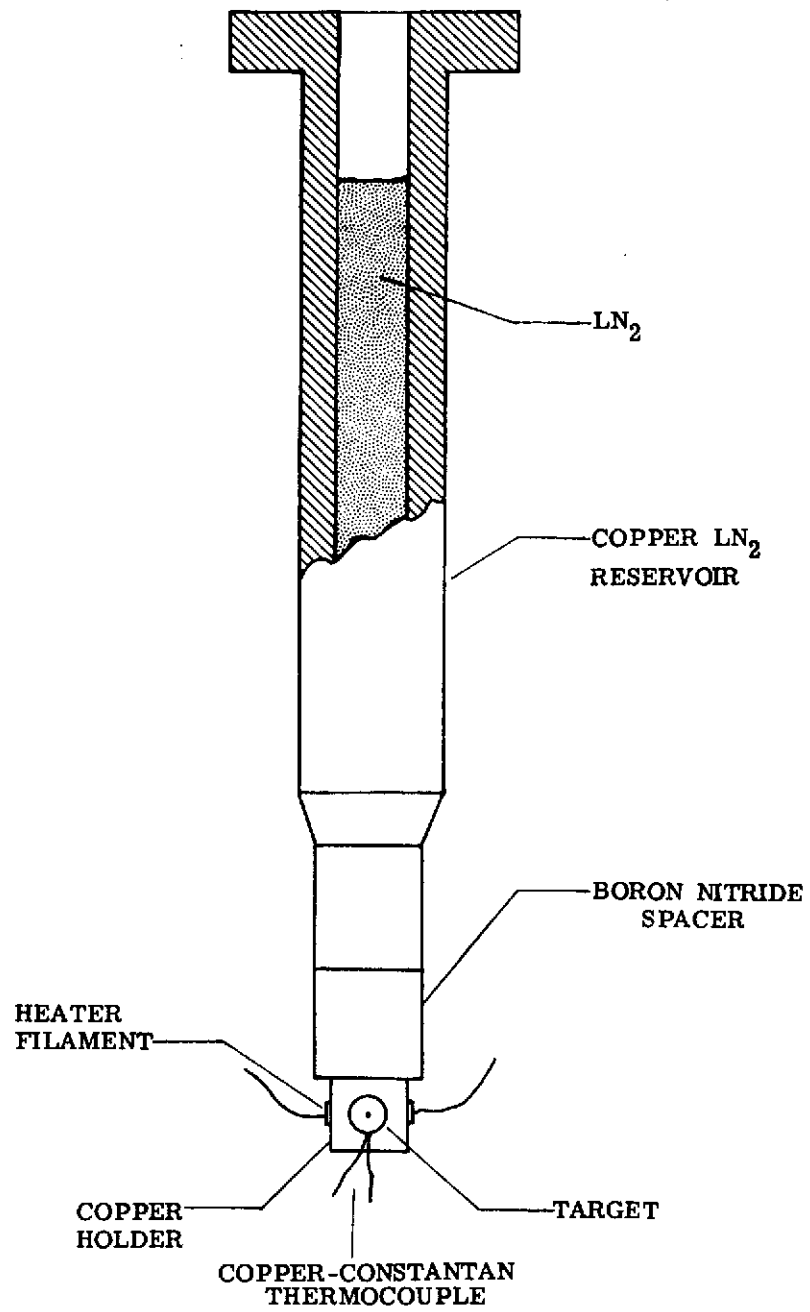


Figure 3.3.1 Target Mount

in acetone followed by distilled water. After mounting the target in the vacuum chamber and evacuation of the chamber, the target was heated to about 450°K and held there for 3 hours. The target was then cooled and stay-time experiments were performed. The second Ni target (hereafter referred to as Ni B) was heated in a vacuum oven to 1300°K for 30 minutes, removed, and then subjected to a series of cleaning steps known as the "Diversey" process. Although the detailed compositions of the cleaning agents used in this process are proprietary to the Diversey Company, they consist basically of (a) a degreaser, (b) an oxidizer, (c) an oxide remover, (d) an etchant and finally (e) a distilled water rinse. This process has been used successfully in other experiments⁽²⁷⁾ on nickel to remove all but a few atomic layers of oxide from the surface. The Ni B target was then subjected to vacuum heating and stay-time experiments similar to those for the Cu and Ni A targets. After a number of experiments with Ni A, it was removed and cleaned by the Diversey process.

For clarity, the steps to which each target was subjected are listed in Table 3.4.1. In this table, specific target preparation procedures are denoted by a shorthand notation. An observable difference between Ni A (or Ni A+D) and Ni B + D was the larger grain size for the Ni B + D resulting from the vacuum firing. An observable difference

TABLE 3.4.1
TARGET SURFACE PREPARATION STEPS

STEP	TARGET DESIGNATION			
	Cu	NI A	NI B + D	NI A + D
Vacuum Heat to 1300 °K			★	
Diversey Clean			★	★
Solvent Rinse (Acetone)	★	★		
Distilled Water Rinse	★	★	★	★
Vacuum Heat to 450 °K	★	★	★	★

between Ni A and Ni A + D resulted from the etching part of the Diversey process.

In addition to the above preparations, some of the targets were subjected to ion bombardment. The ion gun is shown in Fig. 3.4.1. In this gun, high purity (99.995%), inert gas (He, Ar, or Xe) is injected into the gun's ionization region. Positive ions are then accelerated out of this region, pass through a series of focusing rings, and emerge with an energy of 300 eV. The ion beam strikes the target at an angle of incidence of about 45° . From the results of preliminary measurements with this gun in a vacuum bell jar, the ion beam size at the target is estimated to be no greater than 1.0 cm diameter. Ion currents to the target were measured by appropriately connecting the thermocouple leads through an electrometer. Using argon gas in the gun, ion currents were typically 2×10^{-9} amps. The gas injection rate was such as to cause the test chamber pressure to rise by 2×10^{-7} torr.

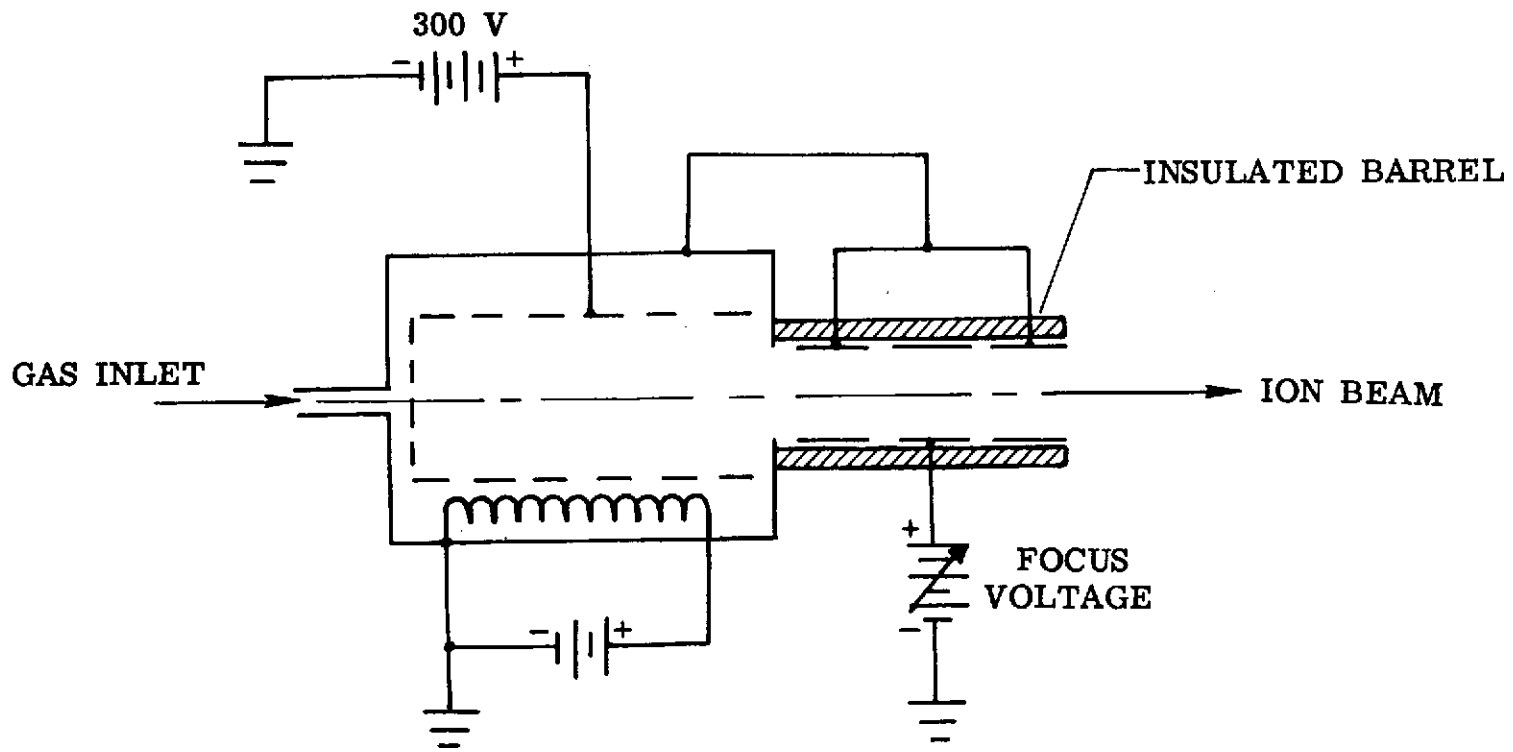


Figure 3.4.1 Ion Gun

CHAPTER 4

RELATION OF DETECTOR SIGNAL TO MEAN STAY TIME FOR A FIRST-ORDER DESORPTION PROCESS

The shape of the detector signal for a distribution of stay times corresponding to a first-order desorption process is examined in this chapter. The effects of finite shutter open time and finite molecular transit times from chopper-to-target and target-to-detector are included in this examination for the geometry and experimental conditions of the present study. For the assumed first-order desorption process, a method is presented for deducing mean stay times from certain parameters of the detector signal. The analysis is a generalization of that presented by Bailey⁽¹⁵⁾ to include the effects of finite shutter open time and incident beam speed distribution.

4.1 Detector Signal for a Triangular Shutter Function and First-Order Desorption

Consider the case of unsteady adsorption followed by desorption at a rate proportional to the surface coverage (first-order desorption). The total rate of change in

surface coverage is then

$$\frac{d\sigma_a}{dt} = P_a F_i - \frac{\sigma_a}{\tau} \quad (4.1.1)$$

If the adsorption rate, given by $P_a F_i(t)$, is known, then the solution of Eq. (4.1.1) is

$$\sigma_a(t) = \exp(-t/\tau) \int_{-\infty}^t P_a F_i(t') \exp(t'/\tau) dt' \quad (4.1.2)$$

The stay time τ is the mean stay time for the ensemble $P_a F_i(t') dt'$. The desorption flux $F_d(t)$, of course, is simply

$$F_d(t) = \sigma_a(t) / \tau \quad (4.1.3)$$

The effects of shutter open time and transit times can now be added to determine the expected shape of the detector signal. The shutter time and transit time from chopper-to-target are contained implicitly in the incident pulse $F_i(t)$.

The shape of this pulse is dependent upon the speed distribution for the incident beam and upon the shutter function $g(t)$. (The shutter function describes the shape of the pulse as it emerges from the chopper slot and depends on the rotational speed of the chopper and the beam-chopper-target geometry.) In the present experiments, the effective open time of the shutter is much larger than the mean transit time from the chopper to target. In Appendix III, it is shown that in this limit

$$F_i(t) \sim g(t-t_{o1}) \quad (4.1.4)$$

where t_{o1} is the most probable time of flight from the chopper to the target. If $g(t)$ is approximated by a symmetric triangle of basewidth $2t_s$, then

$$\frac{F_i(t)}{F_o} = \begin{cases} 1+(t-t_{o1})/t_s & \text{for } -t_s < t-t_{o1} < 0 \\ 1-(t-t_{o1})/t_s & \text{for } 0 < t-t_{o1} < t_s \\ 0 & \text{otherwise} \end{cases} \quad (4.1.5)$$

where F_o is an appropriate proportionality factor (approximately equal to the steady-state beam flux striking the

target if the chopper were removed).

If the desorbing molecules have a Maxwellian speed distribution corresponding to the surface temperature, it can be shown⁽¹⁵⁾ that the detector signal $S(t)$ will have the form

$$S(t) = S_0 \int_{-t_s + t_{o1}}^t \frac{\sigma_a(t')}{\tau} \left(\frac{1}{t-t'} \right)^4 \exp \left[- \left(\frac{\beta_s x_2}{t-t'} \right)^2 \right] dt' \quad (4.1.6)$$

where $\beta_s = \sqrt{m_g/2kT_s}$, x_2 is the target-detector distance and S_0 is an appropriate proportionality factor (since only the time-wise shape of the signal is of interest, the proportionality factor is unimportant). The time $\beta_s x_2 / \sqrt{2}$ is the most probable transit time from target to detector. In the present experiments, t_s and $\beta_s x_2$ were about the same magnitude and both were greater than t_{o1} by a factor of 15 to 20.

4.2 Relationship Between τ and Parameters of the Predicted Signal Shape

The shape of the detector signal is now obtained by combining Eqs. (4.1.2), (4.1.5) and (4.1.6). At this point, it will be further assumed that $P_a = 1$. Substituting $F_i(t)$ from Eq. (4.1.5) into Eq. (4.1.2) and integrating, one

obtains $\sigma_a(t)$. (The exact result of this integration is given in Appendix III along with some typical shapes for $\sigma_a(t)$ calculated from this expression.) Then substituting this result for $\sigma_a(t)$ into Eq. (4.1.6) yields an integral expression for $S(t)$.

Some typical predicted signals, obtained by numerical integration of the above described expression of $S(t)$, are shown in Fig. 4.2.1. All times shown in this figure are non-dimensionalized by the quantity $\delta = \sqrt{2}t_{01}$. The values of t_s/δ and $\beta_s x_2/\delta$ are typical for the experiments. The time t_m at which $S(t)$ is a maximum and the time t_2 at which $S(t) = \frac{1}{2}S(t_m)$ are used to characterize the signal shape. For non-zero stay time, a "peak shift"

$$\Delta t_s \equiv t_m - t_{m,\tau=0} \quad (4.2.1)$$

and a "time constant"

$$\tau_2 \equiv - \left. \frac{dt}{d[\ln S(t)]} \right|_{t=t_2} \quad (4.2.2)$$

are more direct measures of the stay time. For small τ ($< t_{m,\tau=0} \approx \beta_s x_2$), it may be shown, as might have been expected, that the detector signal is simply delayed by τ , and therefore the peak shift Δt_s is equal to the mean stay

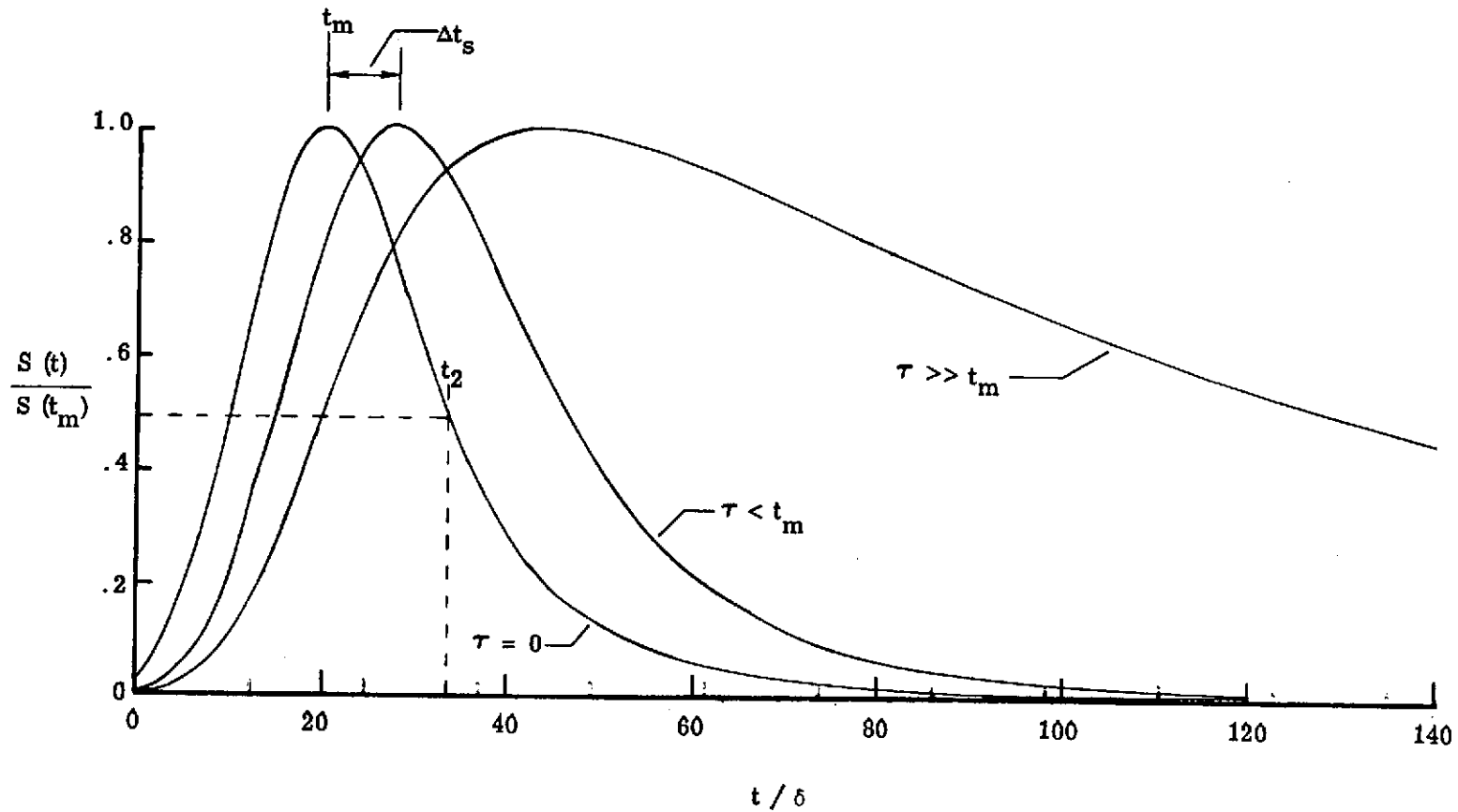


Figure 4.2.1 Predicted Detector Signals,
 $t_s/\delta = 14.9$, $\beta_s x_2/\delta = 23.7$

time. For $\tau \gg t_{m,\tau=0}$ and for $t \gg t_{m,\tau=0}$, the detector signal simply decays as $\exp(-t/\tau)$ and the time constant τ_2 equals the mean stay time. The behavior of Δt_s and τ_2 as functions of τ is illustrated in Fig. 4.2.2 for typical values of t_s and $\beta_s x_2$ (all times are again normalized by δ). This figure shows that, for intermediate values of τ , neither Δt_s nor τ_2 is a good measure of the stay time. By observing the slope of Δt_s versus τ , it is also seen that even though the shutter open time is finite or even large compared to τ (i.e., $t_s \gg \tau$), the peak shift Δt_s is still equal to the stay time for small τ .

In general, the predicted expression for $S(t)$ and the quantities Δt_s and τ_2 are functions of the parameters t_s , t_{o1} , $\beta_s x_2$ and τ . For a given detector signal, all except τ will be known from other experimental information. Thus, if the derived model for $S(t)$ were sufficiently accurate, τ could be determined either by some sort of curve fit of the predicted function to the measured signal shape or by comparisons of predicted to measured Δt_s or τ_2 . Of course, the assumptions made in deriving this model are only approximations, and some disagreement between measured and predicted signal behavior is expected. At least in principle, the validity of these assumptions can be assessed by comparisons of the predicted behavior to that observed experimentally.

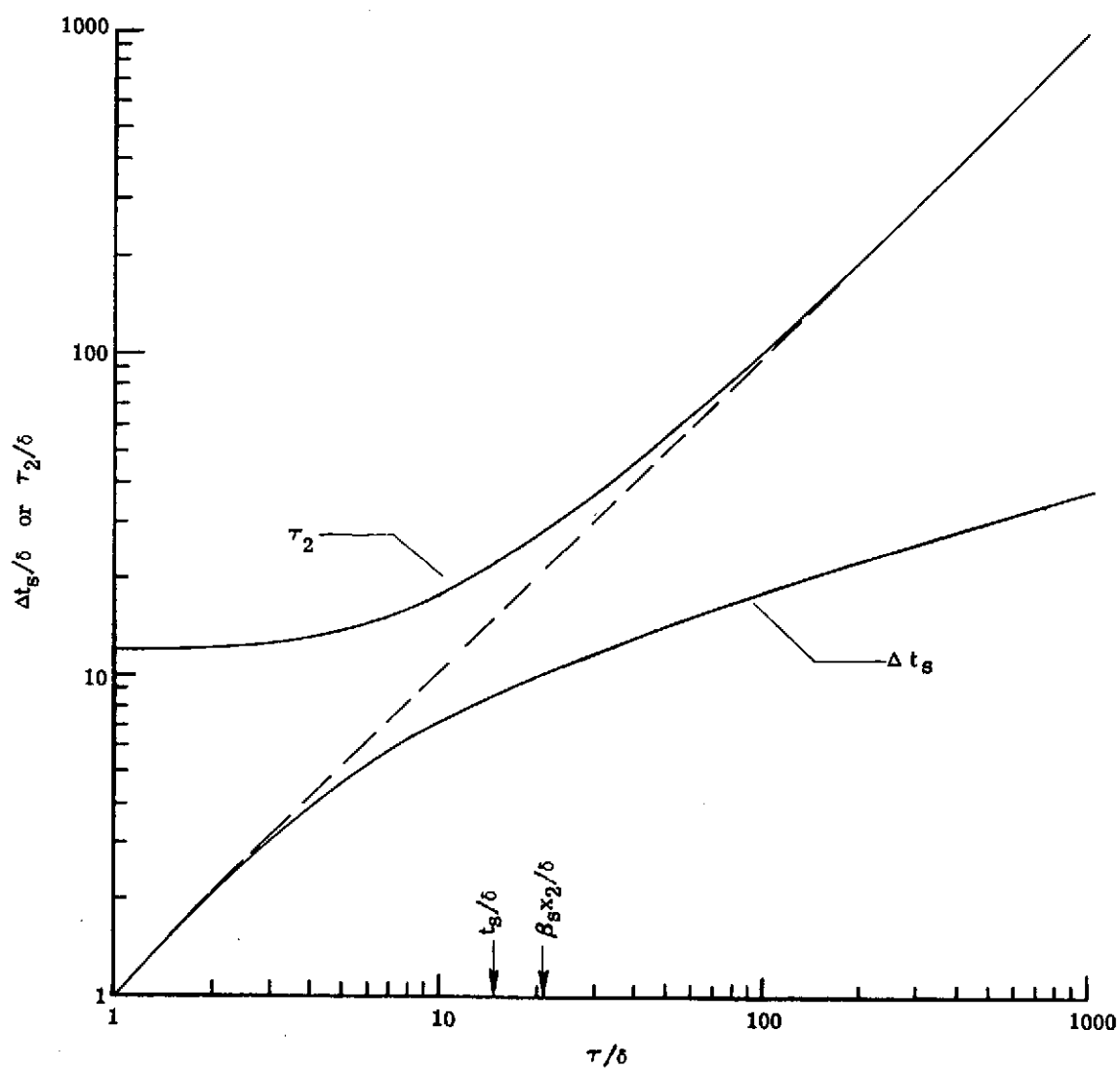


Figure 4.2.2 Predicted Variation of Peak Shift Δt_s and Time Constant τ_2 with Stay Time τ ,
 $t_s/\delta = 14.9$, $\beta_s x_2/\delta = 23.7$

CHAPTER 5

EXPERIMENTAL PROCEDURES

The discussion of the experimental program will be divided into two parts: (a) calibrations and (b) stay-time experiments. Detector calibration and characterization of the molecular beam and TOF detection system are described in Appendix II. The stay-time measurements and the variables involved are described in Sec. 5.1. The techniques for extracting stay times and related parameters from the recorded detector signals are described in Sec. 5.2. An analysis of the uncertainties associated with the measurements and the data reduction techniques is given in Sec. 5.3.

5.1 Stay-Time Experiments

The primary stay-time experiments are listed in Table 5.1.1 along with the experimental conditions for each run. The target designations are those given in Table 3.4.1. The ranges of target temperatures listed are those for which significant peak shifts were observed. For calibration purposes (see Sec. 5.2), detector signals were also recorded at a number of temperatures between the upper limits listed and room temperature. Each recorded signal represents an average over about 10^4 repetitive pulses (a period of about 2

TABLE 5.1.1
PARAMETERS FOR THE STAY-TIME EXPERIMENTS

RUN DESIGNATION	GAS SPECIES	TARGET	TARGET TEMPERATURE °K	ION BOMBARDMENT SPECIES	ION DOSAGE PRIOR TO RUN, C	ION CURRENT DURING RUN, A
Xe → Cu	Xe	Cu	117 → 102	None	0	0
Xe → Ni A	Xe	Ni A	123 → 105	None	0	0
Xe → Ni A + D	Xe	Ni A + D	117 → 105	None	0	0
Xe → Ni A + D + He ⁺	Xe	Ni A + D	111 → 99	He	5×10^{-6}	2×10^{-9}
Xe → Ni A + D + Ar ⁺	Xe	Ni A + D	117 → 99	Ar	5×10^{-6}	3×10^{-9}
Xe → Ni A + D + Xe ⁺	Xe	Ni A + D	105 → 99	Xe	5×10^{-6}	2×10^{-9}
Xe → Ni B + D	Xe	Ni B + D	123 → 102	None	0	0
Xe → Ni B + D + Ar ⁺	Xe	Ni B + D	114 → 95	Ar	5×10^{-6}	2×10^{-9}
Kr → Ni A + D	Kr	Ni A + D	99 → 92	None	0	0
CO ₂ → Ni A + D	CO ₂	Ni A + D	123 → 108	None	0	0

minutes) during which time the target temperature was held constant.

In addition to the experiments listed in Table 5.1.1, detector signals were recorded for $\text{Xe} \rightarrow \text{NiA}$ at $T_s = 111^\circ\text{K}$ at various source pressures between 1 to 10 torr. Detector signals were also recorded as a function of exposure of the surface to various gases for $\text{Xe} \rightarrow \text{NiA} + \text{D} + \text{Ar}^+$ at $T_s = 108^\circ\text{K}$. Other experimental conditions were the same for all experiments listed in Table 5.1.1 and are listed in Table 5.1.2.

5.2 Data Reduction

Peak Shifts. In order to find the previously defined peak shift for a measured detector signal, it is necessary to determine the peak location t_m for that signal and the time $t_{m,\tau=0}$ corresponding to the temperature at which the signal was measured. The time t_m for each recorded signal was determined from a least-squares-polynomial fit to the recorded signal in the neighborhood of the apparent maximum. To establish the quantity $t_{m,\tau=0}$, the expected variation in this quantity with surface temperature was used. Experimentally, it has been found that, for T_s at or below room temperature, most gases thermally accommodate themselves to the solid before leaving the surface. Thus, in the range of T_s where τ is negligible and with negligible shutter open

TABLE 5.1.2

FIXED CONDITIONS FOR THE EXPERIMENTS

SOURCE PRESSURE, p_0	10 ± 0.1 torr
SOURCE TEMPERATURE, T_0	295 ± 3 °K
SHUTTER OPEN TIME, t_s	$2.4 \pm 0.4 \times 10^{-4}$ sec
SHUTTER-TO-TARGET DISTANCE, x_1	0.32 ± 0.05 cm
TARGET-TO-DETECTOR DISTANCE, x_2	4.36 ± 0.1 cm
ANGLE BETWEEN INCIDENT BEAM AND TARGET NORMAL	45 ± 5 °
ANGLE OF REFLECTION INTO DETECTOR	45 ± 5 °
MOST PROBABLE TRANSIT TIME FROM SHUTTER TO TARGET, $\beta_0 x_1 / \sqrt{2}$ (Calculated for Xe)	$1.1 \pm 0.2 \times 10^{-5}$ sec

time, one would expect

$$t_{m,\tau=0} = A + B/\sqrt{T_s} \quad (5.2.1)$$

where A and B are constants. However, for finite shutter open time, it is not obvious that $t_{m,\tau=0}$ predicted from Eq. (4.1.6) will show precisely the above behavior. Therefore, t_m was measured for three gases, Xe, Kr and CO₂, over a range of T_s where τ was expected to be negligible. Corresponding values of $t_{m,\tau=0}$ were also determined for detector signals predicted by Eq. (4.1.6). Both sets of results are shown in Fig. 5.2.1 and $t_{m,\tau=0}$ is seen to vary linearly with $1/\sqrt{T_s}$. The indicated quantitative agreement between measured and predicted values is an artifact to some extent. The measured values had a fixed uncertainty due to a time displacement between $g(t)$ and the chopper photopulse. (This uncertainty was virtually unimportant in determining peak shifts, since the displacement was presumedly constant for a given data run.) Thus, the measured t_m 's shown in Fig. 5.2.1 have been adjusted such that the respective best-fit straight lines through measured and predicted values have the same intercept A at $1/\sqrt{T_s} = 0$. Nevertheless, the temperature dependence of Eq. (5.2.1) is quite close to that observed and therefore provided satisfactorily accurate estimates of $t_{m,\tau=0}$. Values of A and B were determined from

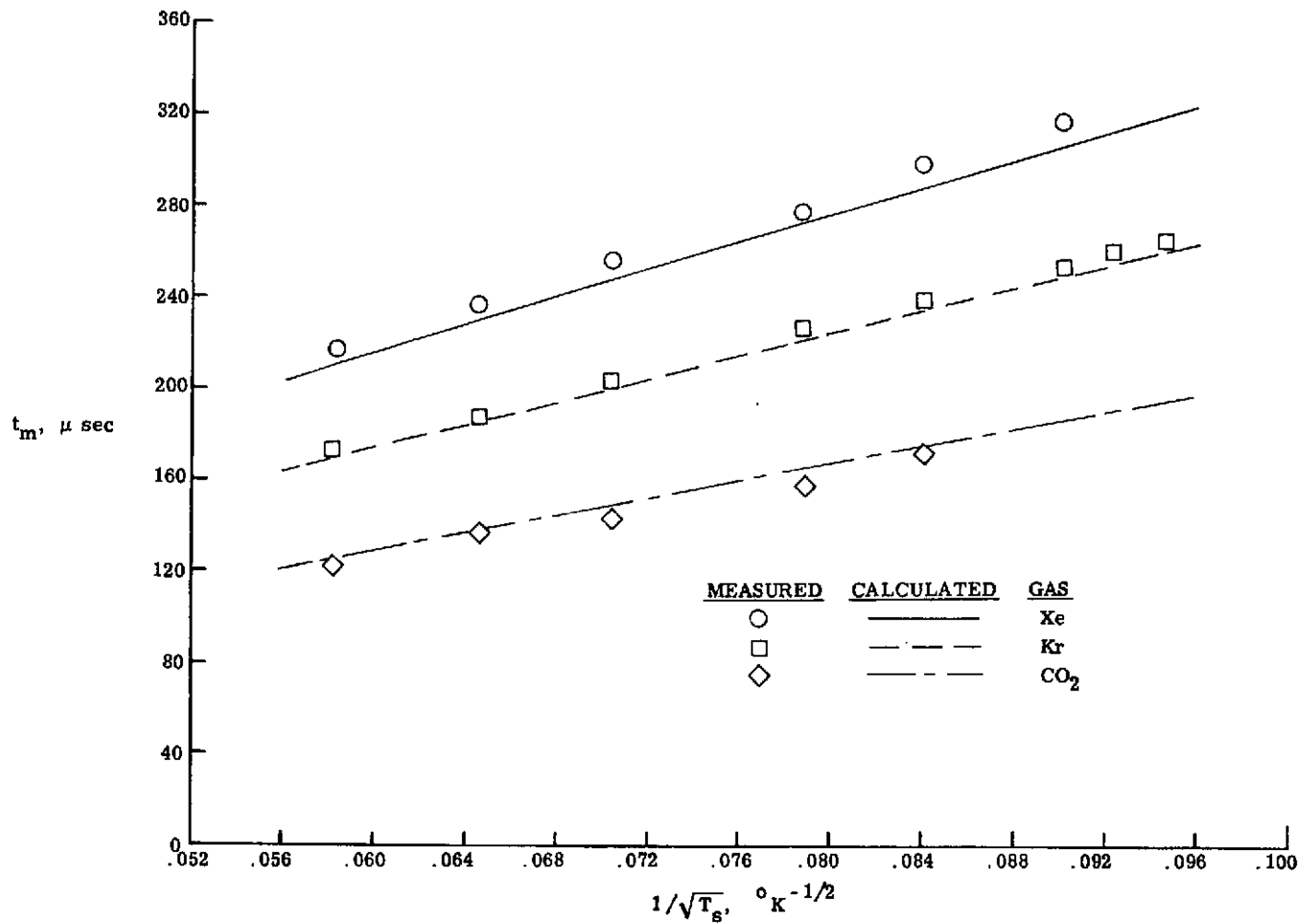


Figure 5.2.1 Comparison of Measured and Predicted Variation of Most Probable Time t_m with Target Temperature, Target Ni A

data for each run similar to that shown in Fig. 5.2.1.

Time Constants. The time constant, τ_2 , was determined by fitting the expression

$$S(t) = Ce^{-t/\tau_2} \quad (5.2.2)$$

to the detector signal in the neighborhood of $t = t_2$. The above form, equivalent to the definition given in Eq. (4.2.2), was more convenient to use in computerized data processing.

Mean Stay Time. The stay-time τ was estimated from Δt_s using the detector signal model given in Chapter 4. Given values of t_s , t_{o1} , and $\beta_s x_2$, an initial value for τ was assumed and used to calculate $S(t)$ from Eq. (4.1.6). The value of Δt_s for this $S(t)$ was determined and compared to the experimental value. Iteration on τ was continued until the calculated and experimental values of Δt_s agreed. The quantities t_{o1} and $\beta_s x_2$ used in the above were calculated using the measured source and target temperatures, respectively, and the flight lengths x_1 and x_2 . The effective shutter open time t_s was determined from a separate series of measurements in which detector signals were recorded as a function of chopper speed. In the limit of large shutter open time ($t_s \gg \beta_s x_2$ and τ), it can be

shown⁽²⁶⁾ that the detector signal shape will approach that of the shutter function $g(t)$. For a triangular shutter function, t_s is just the width at half-maximum and should be linearly proportional to the chopper period. The observed variation of the detector signal width at $\frac{1}{2}S(t_m)$ was also found to be linear with chopper period at slow chopper speeds. Thus, this variation was used to estimate the effective open time at higher chopper speeds of the triangular shutter function used in the stay-time estimations.

Binding Energy and Preexponential Factor. If the stay time obeyed a Frenkel-type relation and if the first-order detector signal model were perfectly accurate, then the measured dependence of the above determined τ with T_s could be used to obtain the binding energy E_0 and preexponential factor τ'_0 . However, as will be seen in Chapter 6, disagreement between measured and predicted detector signals gave reason to question some of the model assumptions. As a result of this disagreement, the stay times calculated from the peak shifts are considerably in error at the lower surface temperatures. Therefore, the qualitative behavior of the factors E_0 and τ'_0 was determined directly from the peak shift data assuming

$$\Delta t_s = \tau'_0 \exp(E_0/kT_s) \quad (5.2.3)$$

The parameters, E_0 and τ'_0 , were estimated for each data set by the following procedures:

- (1) Direct curve-fit of Eq. (5.2.3) to peak shift data;
- (2) Calculate E_0 for each data point based on mobile-adsorption prediction, Eq. (2.1.11), assuming $\tau = \Delta t_s$;
- (3) Calculate E_0 for each data point based on localized-adsorption prediction, Eq. (2.1.12), again assuming $\tau = \Delta t_s$.

The quantities θ_D and σ_m required in procedures (2) and (3) were taken from Refs. (28) and (29) respectively.

5.3 Uncertainty Analysis

Uncertainties in the results are concerned mainly with the following quantities. First are the uncertainties in the experimental parameters, particularly the surface temperature. Second are the uncertainties in stay-time parameters deduced directly from the recorded detector signals; these errors are introduced both by the actual measurement process and the associated data reduction techniques. Next are the uncertainties in stay times, binding energies and preexponential factors that are derived from the measured stay-time parameters and experimental parameters. These latter errors

depend on the parameter uncertainties but are expected to be mainly due to approximations in the detector-signal model and adsorption model employed in deducing said quantities. Finally are uncertainties in the nature of the surface which make data interpretation more difficult.

Uncertainties in experimental conditions. The primary experimental variable which affects the stay time is the target temperature. Systematic error in reported values of the absolute target temperature is less than 3°K (based on calibration of the target thermocouple at the boiling point of liquid nitrogen). However, from the reproducibility of the indicated temperature at different constant heat inputs, errors in temperature differences are estimated to be less than $\pm 0.5^{\circ}\text{K}$. Target temperature fluctuations during the averaging of a given detector signal were typically $\pm 0.5^{\circ}\text{K}$. Other parameter uncertainties which affect the detector signal are listed in Table 5.1.2.

Uncertainties in measured stay-time parameters. Errors in Δt_s and τ_2 result due to timing errors in the signal measurement and due to extraction of these parameters from the recorded signals. The time response of the detector and its signal processing instrumentation was determined from time-of-flight measurements with a single-orifice molecular beam source (see Appendix II). Based on these measurements,

timing errors due to signal shape distortion by the detection system are estimated to be less than 10^{-5} sec. The accuracy of the data reduction for Δt_s and τ_2 depends primarily on the signal-to-noise (S/N) ratio of the recorded signal. Since the S/N generally decreased with decreasing temperature, the absolute uncertainty in these parameters is larger at the lower temperatures. The uncertainty in determining t_m for a given recorded signal varied typically from about $\pm 10^{-5}$ to $\pm 10^{-4}$ sec (or ± 3 to $\pm 6\%$ of measured t_m). Based strictly on the observed linearity (and deviations from linearity) of t_m with $1/\sqrt{T_s}$ at temperatures where τ was negligible, the uncertainty in predicting $t_{m,\tau=0}$ at lower temperatures by Eq. (5.2.1) was about $\pm 10^{-5}$ sec (or $\pm 2\%$ of measured $t_{m,\tau=0}$). These uncertainties in t_m and $t_{m,\tau=0}$ represent the limits of 95% confidence in the data reduction techniques employed. The resulting uncertainties in the data reduction for the peak shift, estimated from the rms sum of the above, varied from about $\pm 2 \times 10^{-5}$ to $\pm 10^{-4}$ sec. The 95% confidence limits in determining τ_2 were more sensitive to the S/N ratio and varied from about $\pm 4 \times 10^{-5}$ sec at the higher temperatures to about $\pm 10^{-3}$ sec at the lowest temperatures for these experiments (corresponding to ± 10 to $\pm 25\%$ of measured τ_2).

Uncertainties in τ , E_0 and τ_0' . The accuracy of the stay time estimated from Δt_s is primarily dependent on the

validity of the detector-signal model. The approximations employed for the incident and desorbed beam speed distributions are expected to be sufficiently accurate for determining τ in this way. The accuracy of the triangular shutter function approximation and the validity of the first-order desorption model will be discussed in the next chapter. Geometrical effects not considered in the model, such as the finite size of the target and detector aperture, are estimated to have negligible effect on the signal shape and thus negligible effect on τ .

The uncertainties in the parameters, τ'_0 and E_0 , are dependent on the validity of the adsorption model and will be discussed in Chapter 6 along with those results.

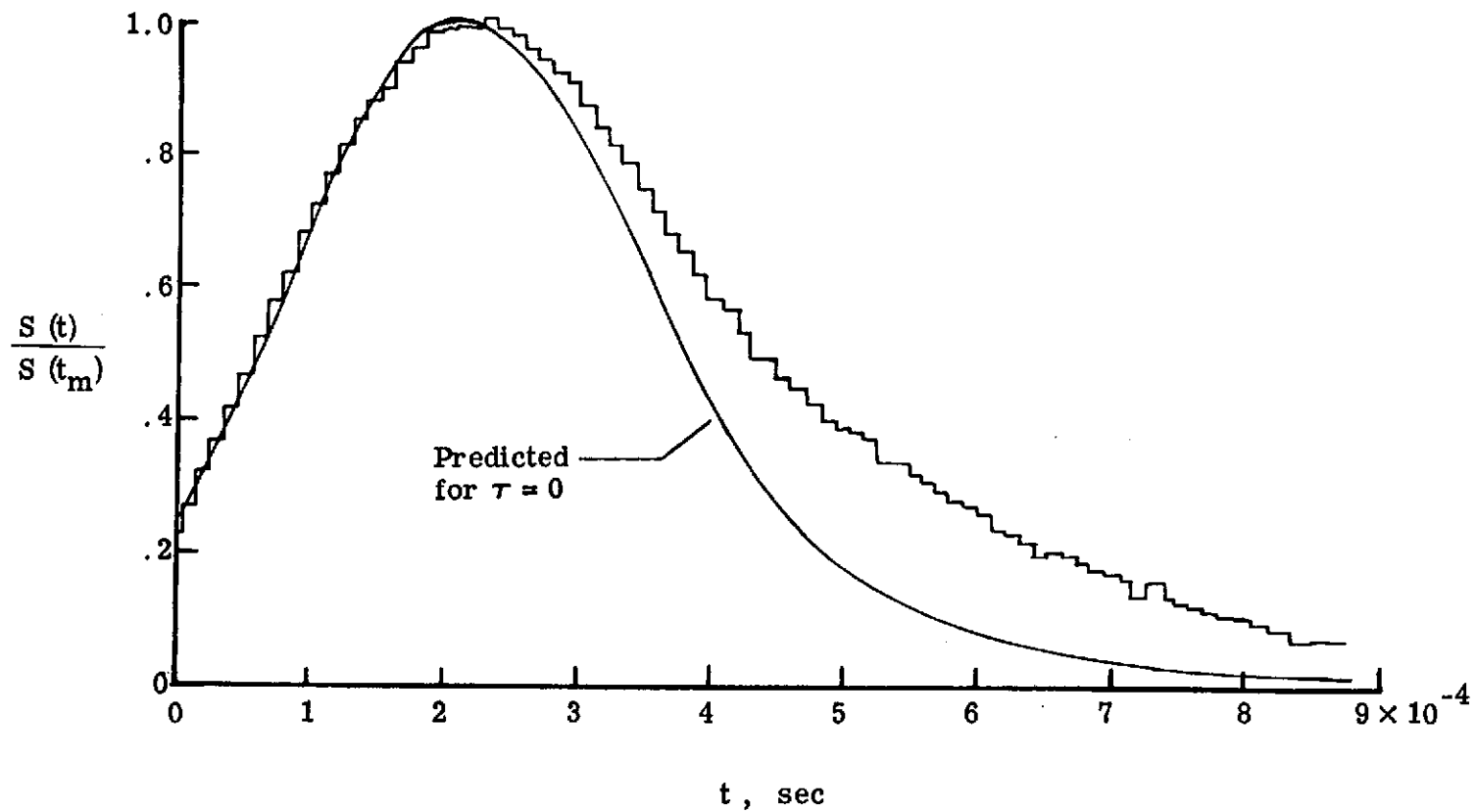
Uncertainties in surface conditions. The composition and physical structure of the surfaces of the various targets is subject to considerable uncertainty. The coverage due to gases (other than the beam species) adsorbing from the test chamber background was probably significant particularly at the lower temperatures. Nevertheless, the reproducibility of these conditions is verified to some extent at least by the reproducibility of the experimental results presented in Chapter 6.

CHAPTER 6

RESULTS

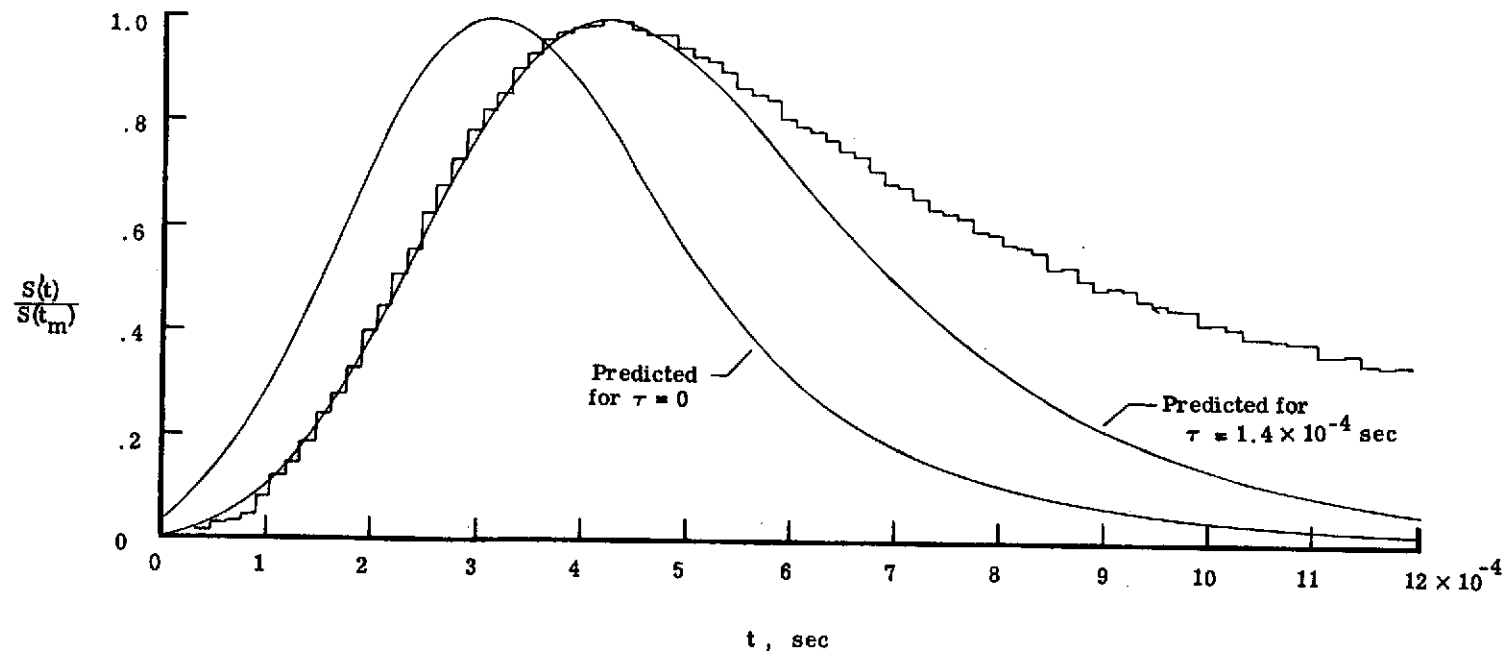
6.1 Comparison Between Measured and Predicted Detector Signal Shapes

Three typical recorded detector signals are shown in Fig. 6.1.1. For part (a) of this figure, the detector signal was recorded with the target at room temperature where the stay time should be very small. The signal shape predicted by Eq. (4.1.6) for $\tau = 0$ is shown here for comparison. The agreement between measured and predicted signals is good up to $t \approx t_m$, but for $t > t_m$, the measured signal decays at a rate smaller than predicted. The disagreement at large times may be due in large part to errors in the approximate shutter function used in generating the theoretical curve. The assumed shutter function is symmetric about its midpoint. Calculations by Olander⁽³⁰⁾ indicate that the symmetry of the angular flux distribution and therefore the symmetry of the shutter function are sensitive to source-collimator alignment. Some additional calculations of signal shapes were performed using an asymmetrical triangular shutter function. By varying the degree of asymmetry in this function, a shutter function was found which predicted the measured signal shape up to $t \approx t_2$. Comparing this



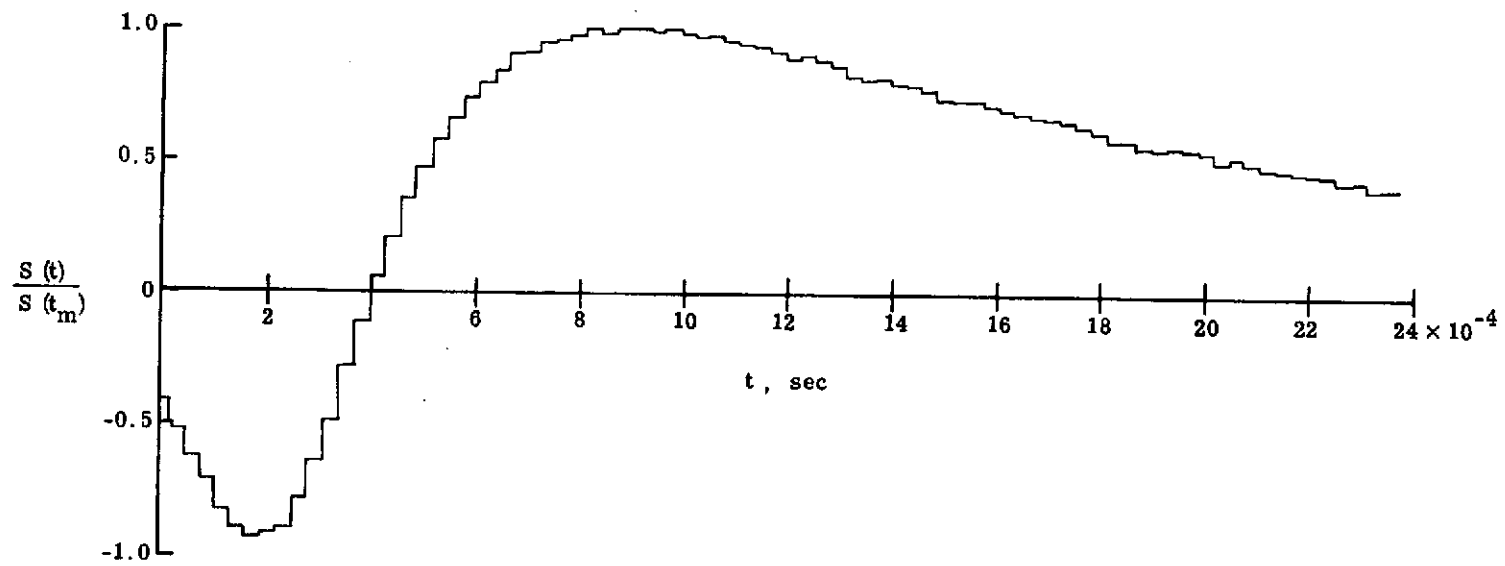
(a) $T_s = 293^\circ\text{K}$

Figure 6.1.1 Comparison of Measured and Predicted Detector Signals, Xe \rightarrow Ni A



(b) $T_s = 114^\circ\text{K}$

Figure 6.1.1 continued



(c) $T_g = 108^\circ\text{K}$

Figure 6.1.1 concluded

asymmetry to predictions of Olander, it is estimated that either a source displacement of about 0.5 source-diameters from the nominal beam axis or a source-exit-plane tilt of 6° could explain the discrepancies in Fig. 6.1.1(a). Such errors are within the misalignment uncertainties for the present beam geometry.

In principle, any measured signal for $\tau = 0$ could be used to solve for the exact shutter function. However, for small τ , it is the shift in the peak with increasing stay time that is of interest. The observed variation in t_m with target temperature for negligible τ is that expected. Thus, to first approximation, the disagreement between theory and experiment at large t should introduce negligible error in the determination of τ from peak-shift data. Of course, estimation of τ from the observed decay rate of the signal at large t (i.e., $t = t_2$) will be affected. Even so, as τ becomes large compared to the discrepancy in time, the error introduced in τ_2 will approach zero.

A second typical signal, measured at a target temperature where the peak shift is finite due to stay time, is shown in Fig. 6.1.1(b). Also shown here are the predicted signal for $\tau = 0$ and the predicted signal for that value of τ which fits the measured signal at t_m . To first order, the predicted ($\tau \neq 0$) curve is delayed approximately by τ up to $t \approx t_m$, but beyond t_m the time delay becomes increasingly

greater. The predicted ($\tau \neq 0$) curve agrees with the measured curve up to $t \approx t_m$. However, for $t > t_m$, the measured curve decays at a lower rate than the predicted ($\tau \neq 0$) curve. This discrepancy at large t is similar to that observed at room temperature for negligible stay time.

At even lower target temperatures (larger stay times) the measured detector signals take on a shape that was altogether unexpected. An example of this shape is shown in Fig. 6.1.1(c). It is seen that the signal exhibits a "negative" dip at small times. To understand a negative signal, it must be recalled that the detector's ion-collector current includes a component due to background gas in the chamber as well as a component due to the pulsed molecular beam. During detector signal processing, only the relatively fast, time-varying components are amplified. That is, the low-frequency (below about 10 Hz) components are intentionally filtered out. Moreover, signal averaging eliminates any background fluctuation which does not occur repetitively at the chopper frequency. Thus, under normal conditions, the background component does not appear in the recorded signal. However, the background gas is composed, in large part, of the same gas as in the beam and is steadily adsorbing and desorbing along with the beam pulses. Since it is impossible for the beam pulses to give rise to the negative dips, it is most likely that the beam pulse in some way

temporarily reduces the rate of desorption of background molecules from the target.

Signals exhibiting the negative dip obviously cannot be described by the detector-signal model for first-order desorption. Still, it was observed that both Δt_s and τ_2 for this type of signal increased with decreasing surface temperature in a reproducible manner for a given data run. In addition, the signal at long times ($t \sim t_2$) seems to decay exponentially as for a first-order process at least to the extent that can be determined by curve-fit techniques. Thus, Δt_s and τ_2 appear to be indicative of at least the qualitative behavior of the stay time even for this type of signal. The behavior of signals exhibiting the negative dip is discussed further in Sec. 6.5.

6.2 Stay-Time Parameters

Stay-time parameters Δt_s and τ_2 deduced from the set of detector signals from which the ones in Fig. 6.1.1 were taken are shown in Fig. 6.2.1. Also shown are values of τ derived from the Δt_s data using procedures described in Chapter 5. The error flags shown represent the limits of 95% confidence for determining Δt_s and τ_2 from the recorded signals by the data reduction techniques described in Chapter 5. (Note that the scatter in the plotted data generally falls well within these limits.) If the stay time varied as

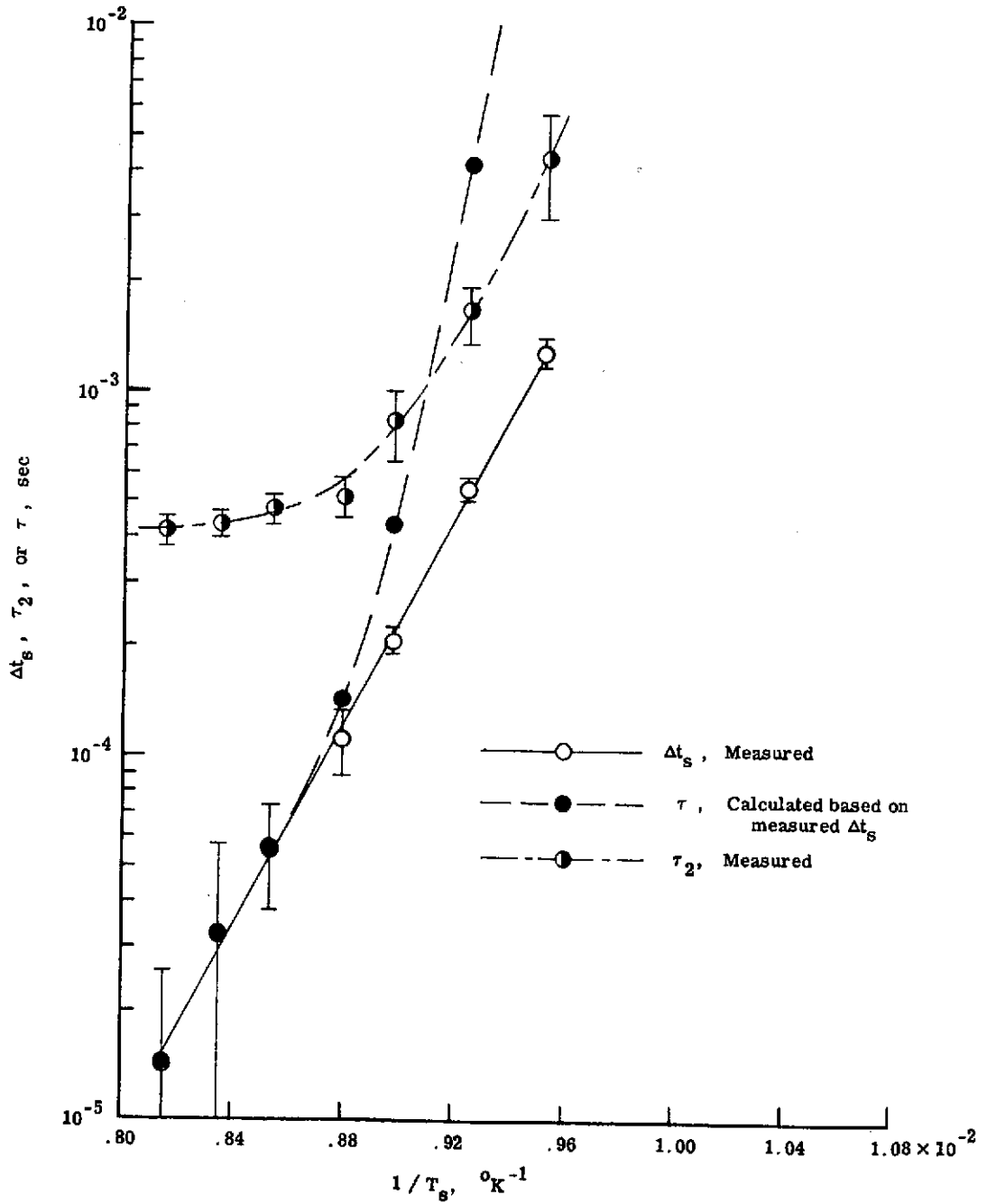


Figure 6.2.1 Typical Variation of Measured Stay-Time Parameters with Target Temperature, Xe \rightarrow Ni A, Error Flags Denote 95% Confidence Intervals in Data Reduction

$\exp(E_0/kT_s)$ and the negative dip did not occur, Δt_s and τ_2 should exhibit variations with T_s^{-1} similar to the variation with τ shown in Fig. 4.2.2. For $\Delta t_s < 10^{-4}$ sec, this is the case. However, for $\Delta t_s \geq 10^{-4}$ sec, τ derived from Δt_s shows a rapid increase as T_s^{-1} increases and eventually exceeds τ_2 . Since in theory one expects $\tau_2/\tau \geq 1$, these τ values are clearly too high at large T_s^{-1} .

The linearity of $\ln \Delta t_s$ with T_s^{-1} noted here was also observed in all other experimental data. At small τ , the slope of $\ln \Delta t_s$ must be the slope of $\ln \tau$ with T_s^{-1} . At large τ , the τ_2 data indicate that the actual stay time is no more than a factor of 4 greater than Δt_s . Thus, it seems that the Δt_s data are better representations of the variation of the actual stay time over the temperature range than one should expect. For this reason, only the peak-shift (Δt_s) data will be considered in the following presentation of the effects of other parameter variations. However, τ_2 and τ data comparable to those shown here have been determined for each recorded signal and are tabulated in Appendix IV.

6.3 Results of Parameter Variations

6.3.1 Effect of Target Material for Xe Adsorption

Peak shift data for Xe adsorption on Cu and NiA are plotted in Fig. 6.3.1. It is seen that the peak shifts obtained with NiA are about twice those for Cu at any given T_s . Since both targets are probably covered to some extent by other physisorbed or chemisorbed species, the differences may be due as much to differences in adsorbates as to differences in the target bulk material. At least one other run for each target reproduced the data shown within approximately the symbol size shown in this figure. Thus, the observed peak shift differences are outside the repeatability of the data.

6.3.2 Effect of Pre-Vacuum Surface Preparation for Xe Adsorption

The effects of the previously described pre-vacuum surface preparations for the nickel samples are illustrated in Fig. 6.3.2. The variation of Δt_s with T_s^{-1} for Xe \rightarrow NiA and Xe \rightarrow NiB+D are almost identical. The best-fit line for Xe \rightarrow NiA+D data intersects the best-fit lines for the other data but has a larger slope. This may be related to the known roughening of the NiA surface by the etchant in the

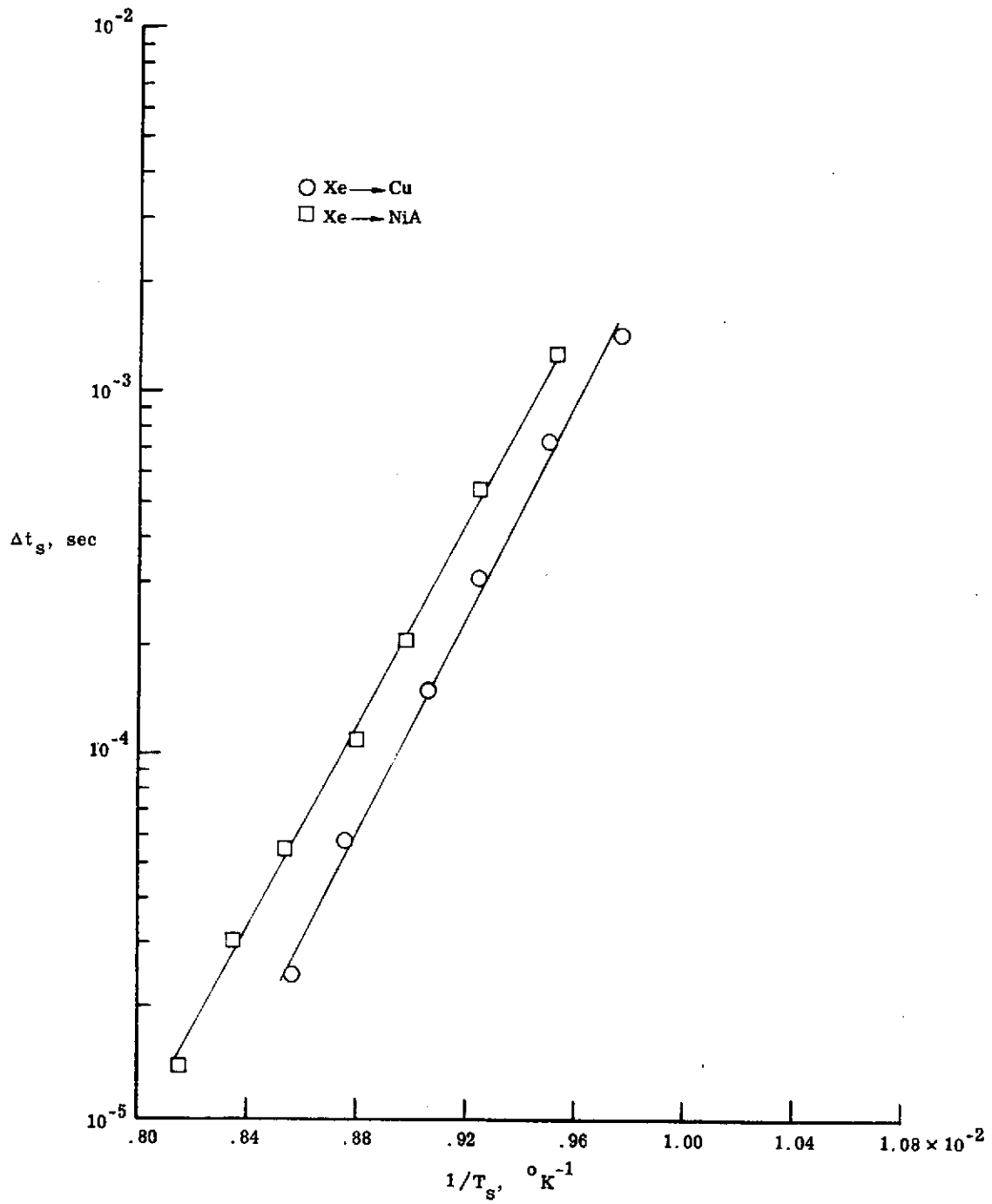


Figure 6.3.1 Variation of Peak Shift with Target Temperature for Two Different Target Materials

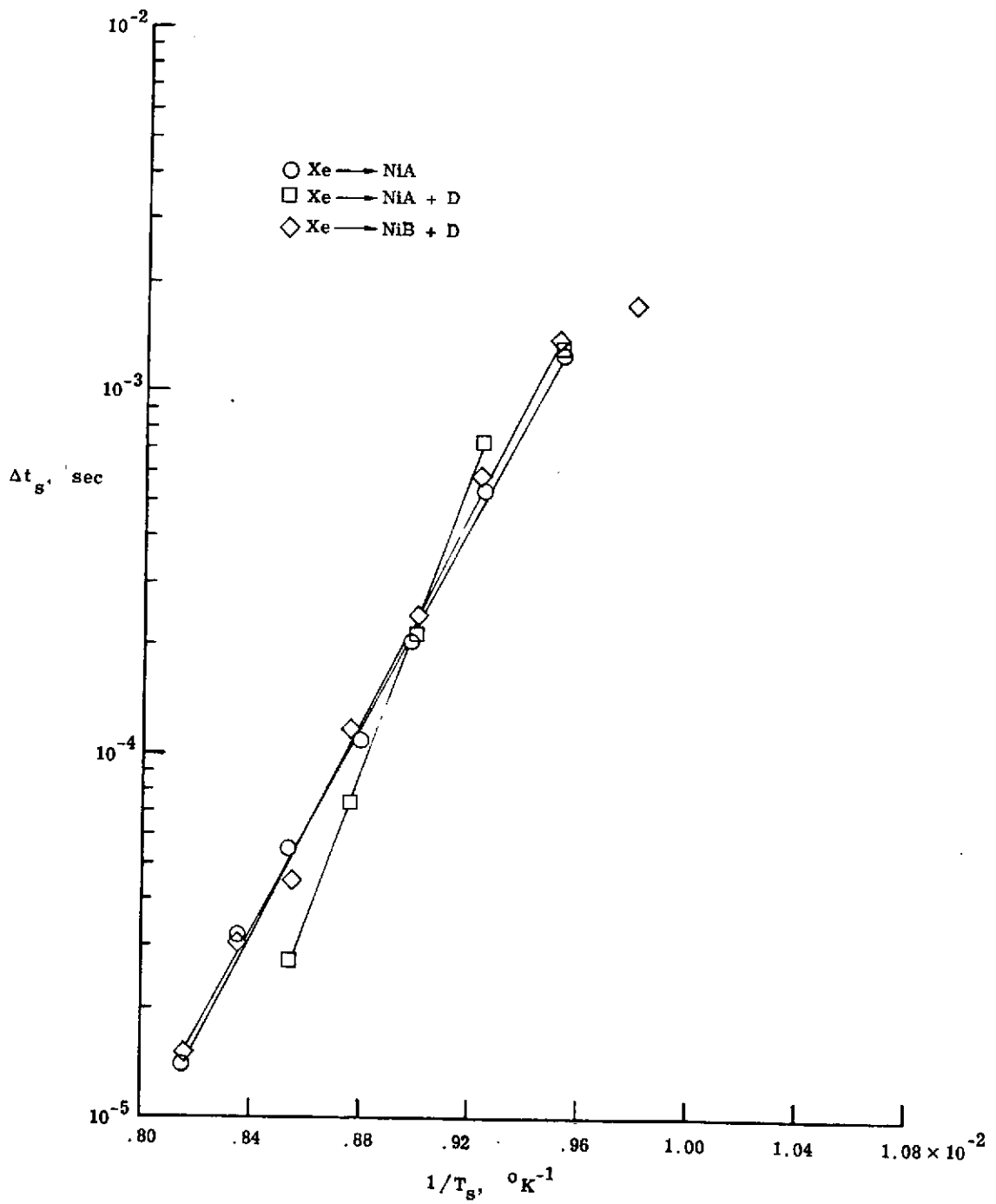


Figure 6.3.2 Variation of Peak Shift with Target Temperature for Different Pre-Vacuum Surface Preparations

Diversey process. (While the NiB+D was also etched, its grain size prior to etching was much larger than NiA due to grain growth during vacuum firing. Therefore, both NiA and NiB+D were smoother to the eye than NiA+D.) The higher slope for NiA+D implies a higher heat of adsorption and this is in qualitative agreement with other work (see for example the discussion of surface non-uniformity by Young and Crowell⁽¹⁾).

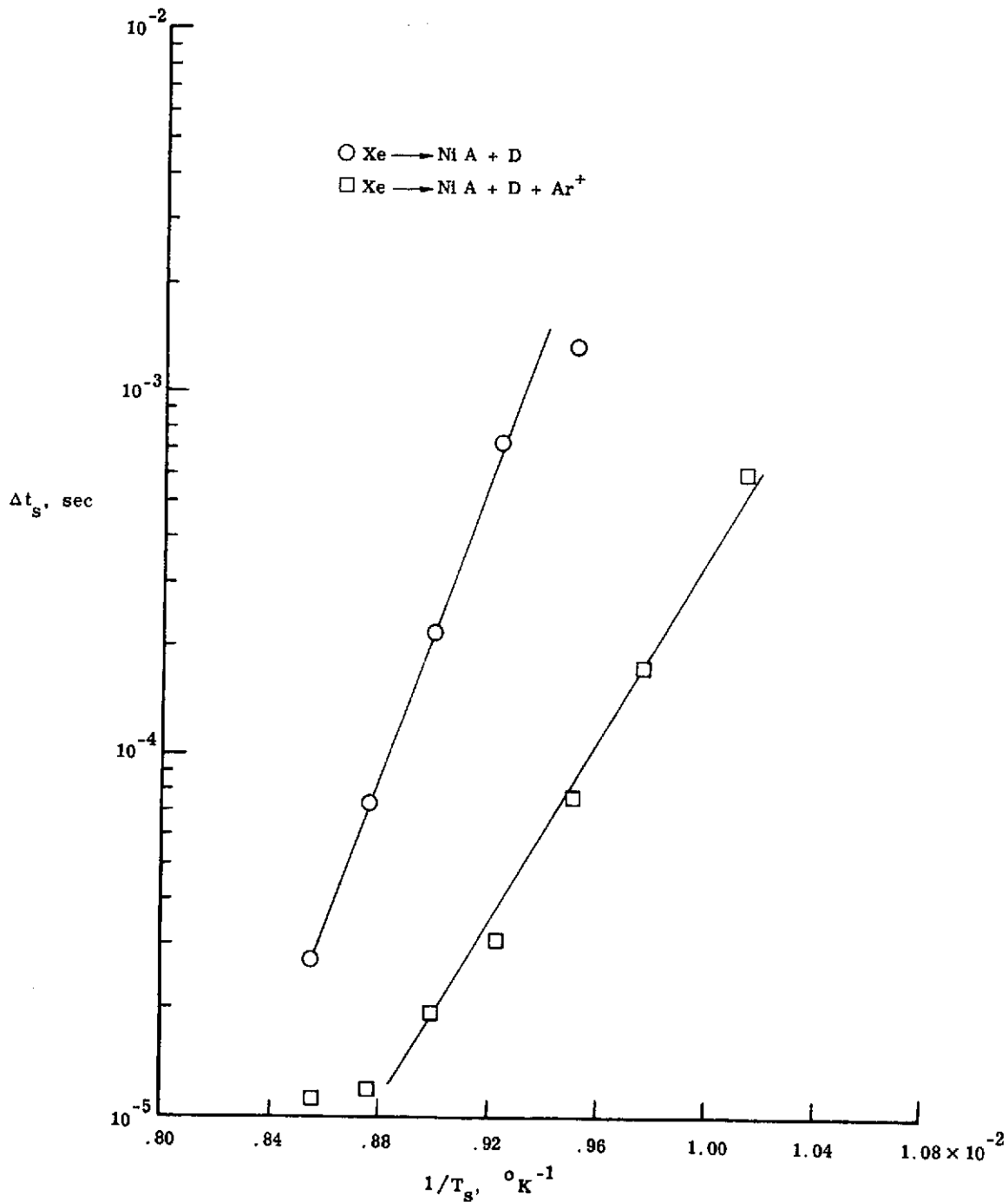
6.3.3 Effect of Argon Ion Bombardment During Xe Adsorption

The effects on the peak shifts of argon ion bombardment of the target are shown in Fig. 6.3.3(a) for Xe \rightarrow NiA+D and in Fig. 6.3.3(b) for Xe \rightarrow NiB+D. At fixed T_s , ion bombardment leads to a factor of 10 to 20 decrease in the peak shift. This result is somewhat surprising, since ion bombardment is usually thought of as a means for creating a cleaner surface and therefore presumably one with higher binding energy for adsorption.

The surface changes that are most likely to occur during ion bombardment are due to:

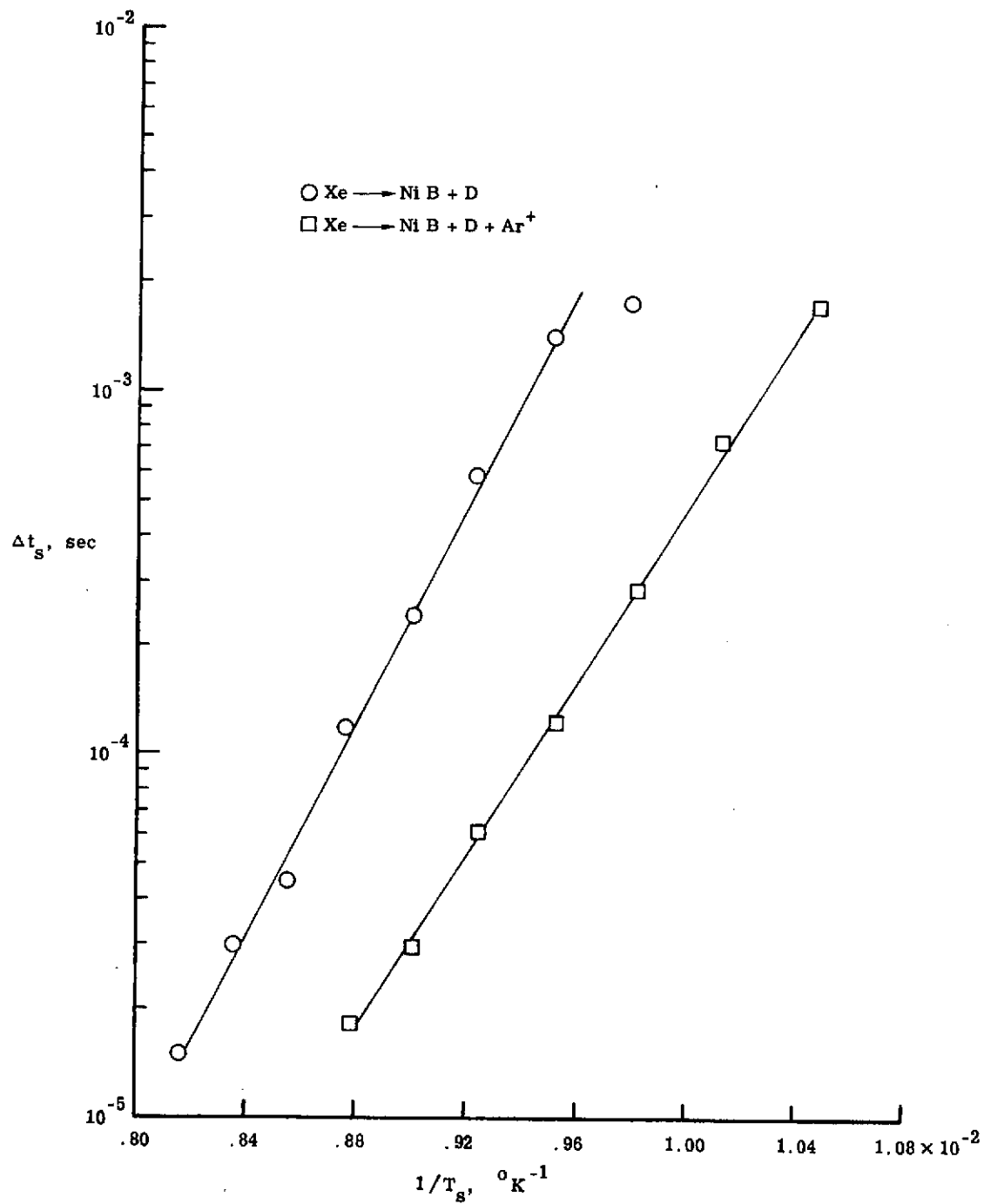
- (1) sputtering of adsorbate;
- (2) sputtering of bulk material;
- (3) implantation of neutralized ion species.

For the present experiments, the ion flux was much less than the



(a) Ni A+D Target

Figure 6.3.3 Variation of Peak Shift with Target Temperature with and without Argon Ion Bombardment



(b) Ni B+D Target

Figure 6.3.3 concluded

flux due to either the beam or the background gas. Thus, ion bombardment should not significantly alter adsorbate coverage from these sources. Although the ion flux was low, the surface was exposed to this beam for a significant time. Based on a sputtering probability of unity⁽³¹⁾ for 300 eV Ar⁺, it is estimated that about 0.1 of the surface atoms should have been sputtered. However, such sputtering should, if anything, increase the effective binding energy and therefore increase the stay time. Thus, the most likely explanation for the observed decrease in peak shift is that the argon ions bury themselves near the surface and reduce the binding energy between the surface and the Xe atoms. For 300 eV argon ions, Johnson⁽³²⁾ estimates the average penetration distance in nickel to be about 4Å. The high desorption energies⁽³³⁾ expected for atoms (neutralized ions) buried even one atomic layer from the surface would result in a negligible desorption probability at these temperatures. The degree to which these buried atoms could affect the binding energy depends on their number density. For a total ion dose of $5 \times 10^{-6} \text{C}$, the argon surface coverage could be at most about $10^{14} \text{ atoms/cm}^2$, about 0.1 monolayer. If the net adsorbate-solid attraction were simply a sum over two-particle attractions and assuming that the attractive force between Xe - Ar is much less than between Xe - Ni, a coverage of 0.1 monolayers of Ar might at

most give rise to a 10% decrease in binding energy for Xe. Because of the exponential dependence of τ on E_0 , a 10% decrease in E_0 can easily result in a factor of 10 decrease in τ . Thus, the observed effect of ion bombardment could easily be attributed to ion burial near the surface.

6.3.4 Effect of Ion Bombarding Species for Xe Adsorption

Following Ar bombardment, the NiA+D target was bombarded with He and then Xe ions. In Fig. 6.3.4, peak shift data measured during ion bombardment with each species are compared to those observed prior to ion bombardment. He and Ar ions are seen to produce comparable reductions in the peak shift, while Xe ions produce an even further decrease.

It was observed that, after the ion beam was shut off and with T_s fixed, the peak shift would increase with time. The rate at which this increase occurred was quite low; even after several days, the peak shift would not return completely to its value prior to ion bombardment. This indicates that a relatively permanent change in the surface occurred during ion bombardment. Thus, the chronological order of the tests could be very important. Time dependence of the measured stay time under various experimental conditions is discussed further in Sec. 6.3.7.

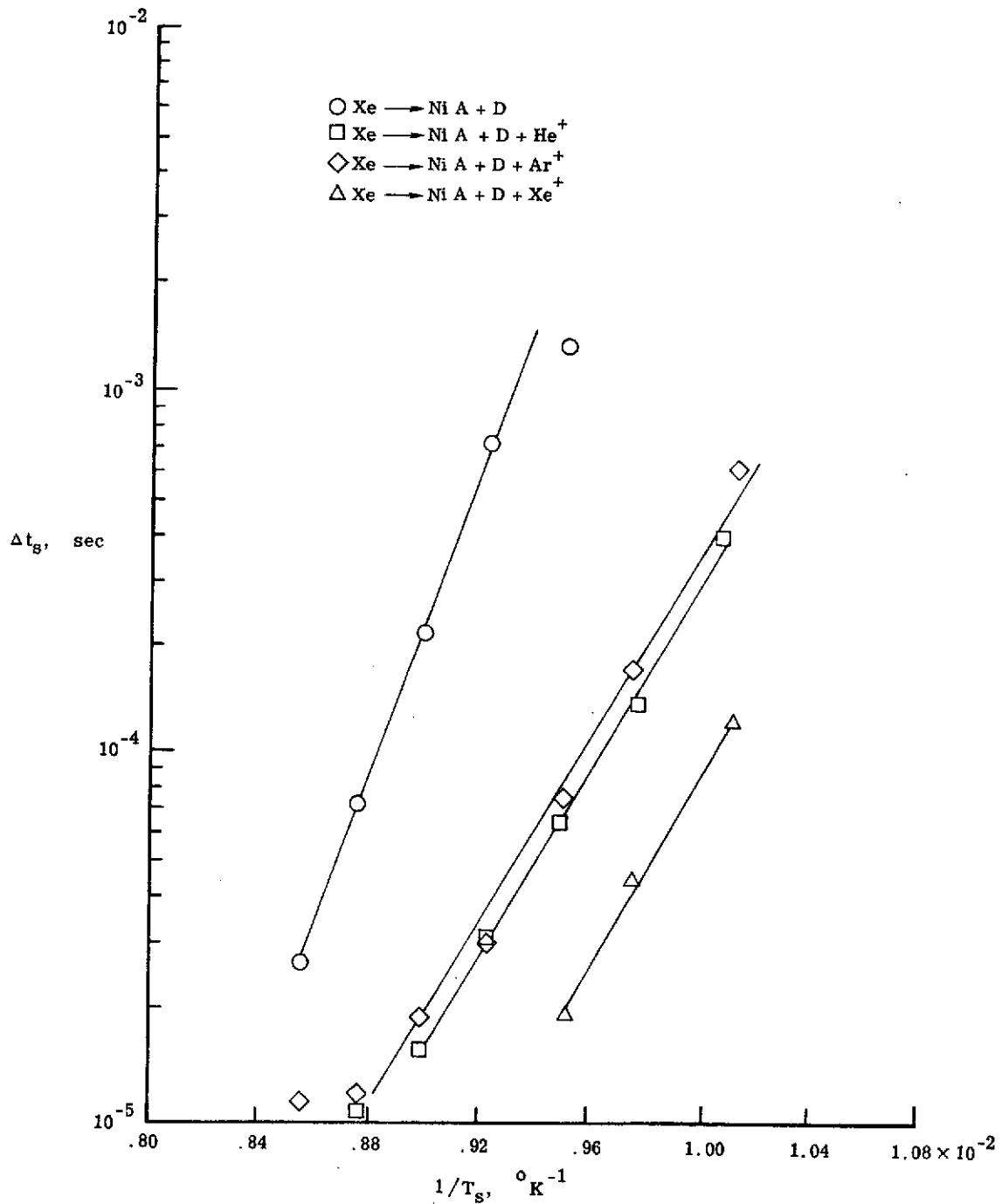


Figure 6.3.4 Variation of Peak Shift with Target Temperature for Different Ion Bombarding Species, Ni A+D Target

6.3.5 Effect of Incident Flux Variation for Xe Adsorption

The effect on the peak shift of varying the incident flux, accomplished by varying the source pressure (flux proportional to $\sqrt{p_0}$ ⁽²⁵⁾), is shown in Fig. 6.3.5. The peak shift is seen to increase by about 50% between $p_0 = 1$ torr and $p_0 = 3$ torr and to reach a broad maximum near $p_0 = 6$ torr. In the absence of adsorbate-adsorbate interactions, τ should be independent of p_0 . However, the appearance of the previously noted negative dip in the detector signal indicates that such interactions are occurring. An estimate of the total surface coverage of Xe from both the beam and background was made using the incident flux of 3.4×10^{15} atoms $\cdot \text{cm}^{-2} \cdot \text{sec}^{-1}$ given in Chapter 3 for $p_0 = 10$ torr and the stay time estimated from the peak-shift data in Fig. 6.3.5. The value obtained for this coverage was about 5×10^{11} atoms $\cdot \text{cm}^{-2}$ or about 10^{-3} monolayers of Xe. Such low coverage would not be expected to give significant Xe - Xe interaction. Of course, adsorbate-adsorbate interactions may have occurred between Xe and some other species adsorbed from the background, but again due to the low coverage of Xe, the peak shift should be independent of p_0 . Thus, in the absence of additional information about the state of the surface, the observed dependence of τ on p_0 cannot be interpreted.

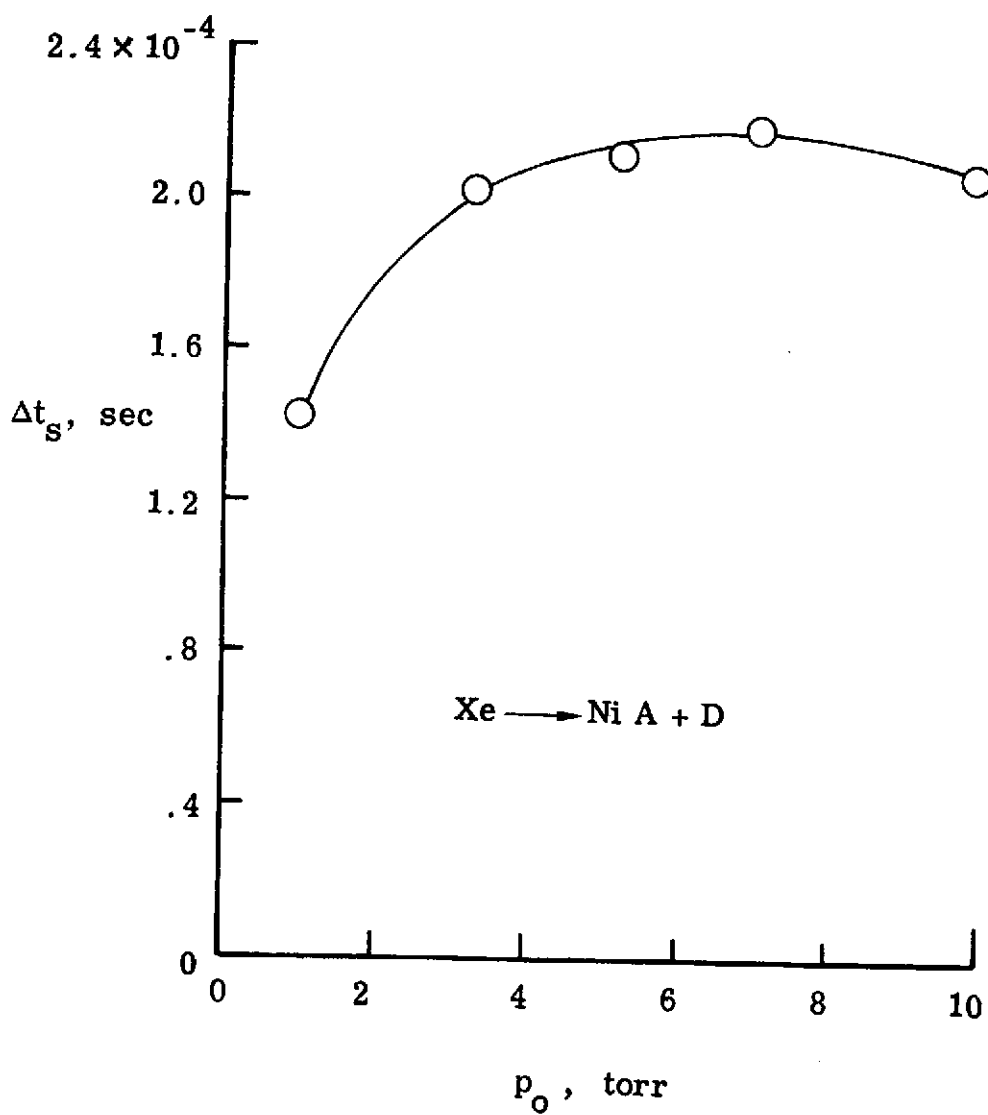


Figure 6.3.5 Variation of Peak Shift with Source Pressure, $\text{Xe} \rightarrow \text{Ni A} + \text{D}$, $T_s = 111^\circ\text{K}$

6.3.6 Stay Times for CO₂ and Kr Adsorption

Peak shift data for CO₂ and Kr adsorbing on NiA are compared to those obtained for Xe in Fig. 6.3.6. The peak shifts for CO₂ are comparable in magnitude to those for Xe but exhibit a smaller slope versus T_s^{-1} . The temperatures at which Kr shows comparable stay times are about 20% lower than those for Xe. This would be expected on the basis of known differences in atom-atom attractive well depths for Xe and Kr⁽³⁴⁾. While the molecule-molecule well depth for CO₂⁽³⁴⁾ falls between those for Xe and Kr, it is not surprising that stay times for a polyatomic gas do not scale exactly with this well-depth.

6.3.7 Variation of Peak Shift with Time

Bailey⁽¹⁵⁾ observed that after cooling his surface to a given temperature, the stay time decreased with elapsed time. This decrease was attributed to the adsorption of gases present in his chamber. Since the present vacuum system and pressures are similar to those in Bailey's work, the time dependence of the peak shift was investigated in this work also.

First, the peak shift was measured as a function of time both with and without simultaneous ion bombardment. These data are shown in Fig. 6.3.7. Also shown in this

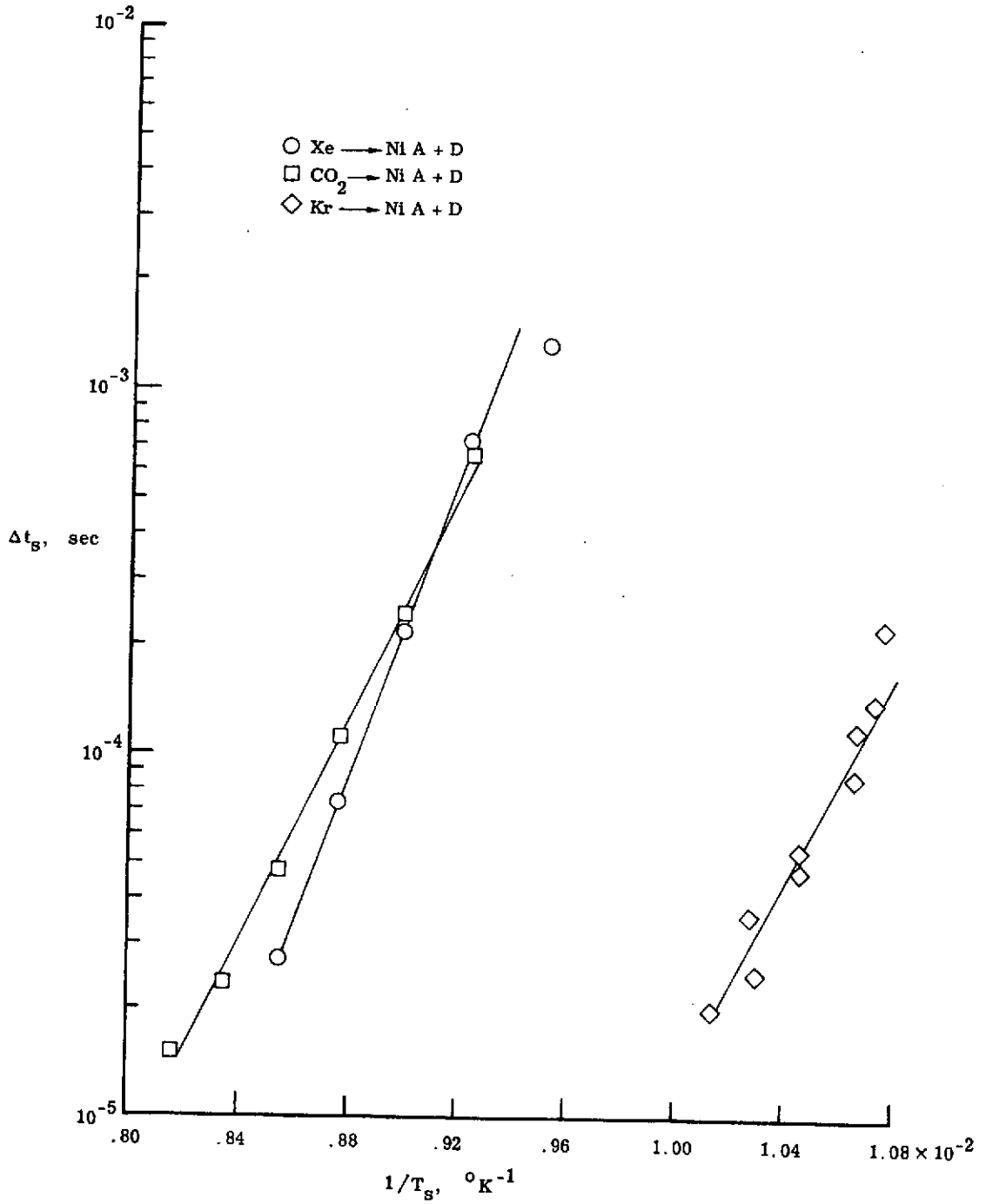


Figure 6.3.6 Variation of Peak Shift with Target Temperature for Different Incident Gas Species, Ni A+D Target

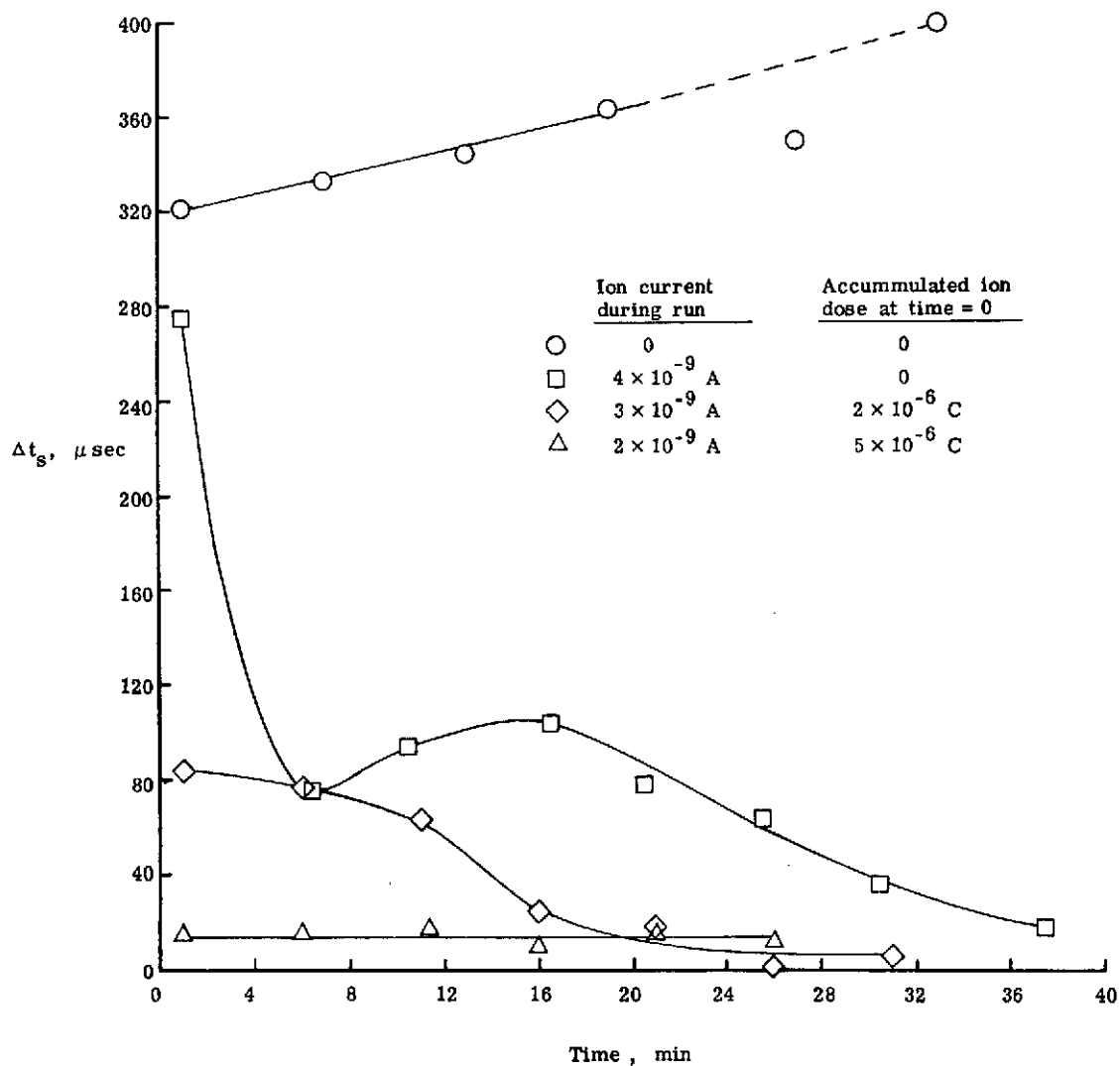


Figure 6.3.7 Variation of Peak Shift with Time During Argon Ion Bombardment for Different Initial Ion Dosages, $\text{Xe} \rightarrow \text{Ni A+D}$, $T_s = 108^\circ\text{K}$

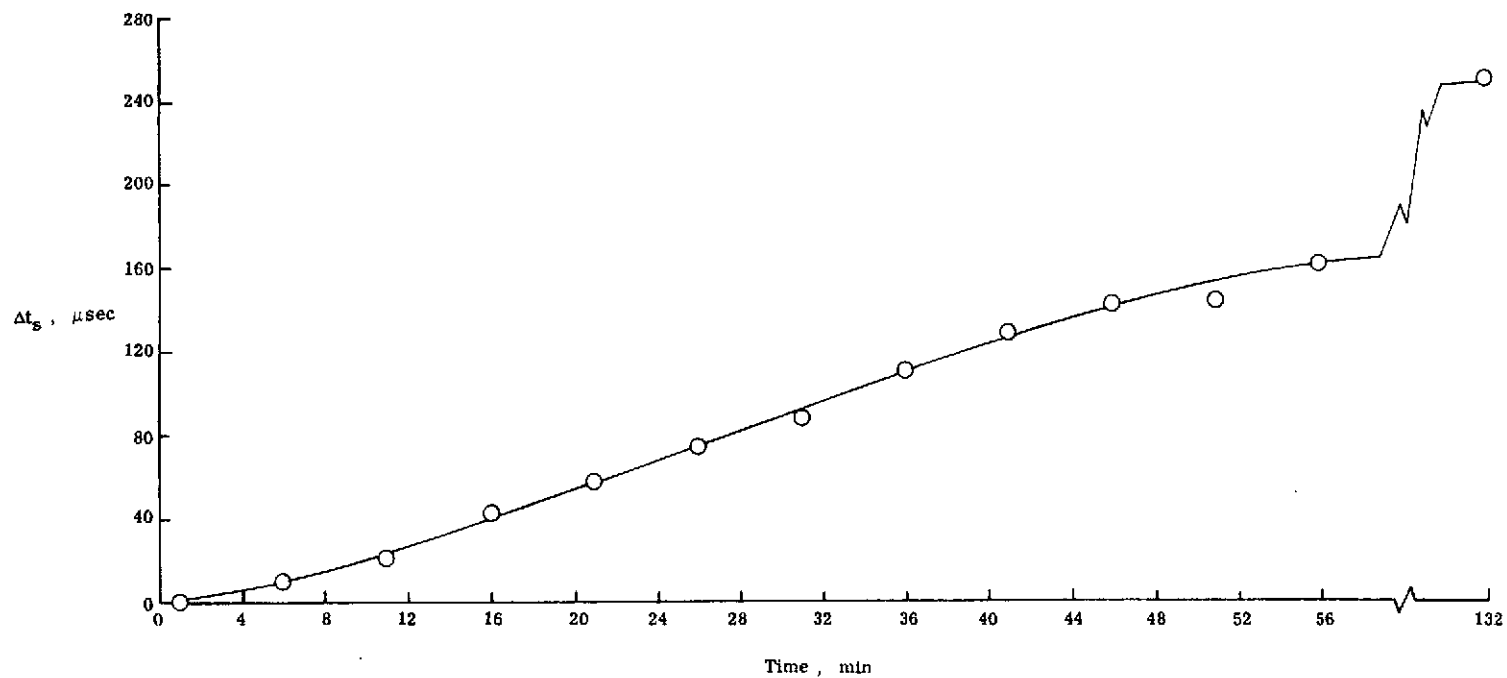
figure are data obtained for different accumulated ion doses at time = 0. (The rate prior to $t = 0$ for these data was that shown for $t > 0$. This accumulated dose is the total charge due to ions received by the sample immediately prior to recording the data; it is not the total dose the target has received since initial installation.)

For no ion bombardment during the recording of the peak shift data (circles), the peak shift shows a gradual increase with time. The target received an accumulated dose of about $5 \times 10^{-6} \text{C}$ on the day previous to this run, and this increase with time is similar to that noted in Sec. 6.3.4 upon cessation of ion bombardment. However, similar increases in Δt_g with time were observed for targets having received no previous ion bombardment.

For ion bombardment beginning at $t = 0$ (squares), the peak shift first decreases sharply with time, levels off, reaches a second maximum and decreases toward some asymptotic limit. The sharp initial decrease is probably due to a larger ion gun current known to occur during the first few minutes of operation. For an initial ion dose of $2 \times 10^{-6} \text{C}$ (diamonds), Δt_g shows a gradual decrease with time, leveling off after about 26 minutes. After an initial dose of about $5 \times 10^{-6} \text{C}$ at $t = 0$ (triangles), Δt_g remains essentially constant. Assuming the previously discussed ion-burial theory is correct, the data in this figure suggest that the

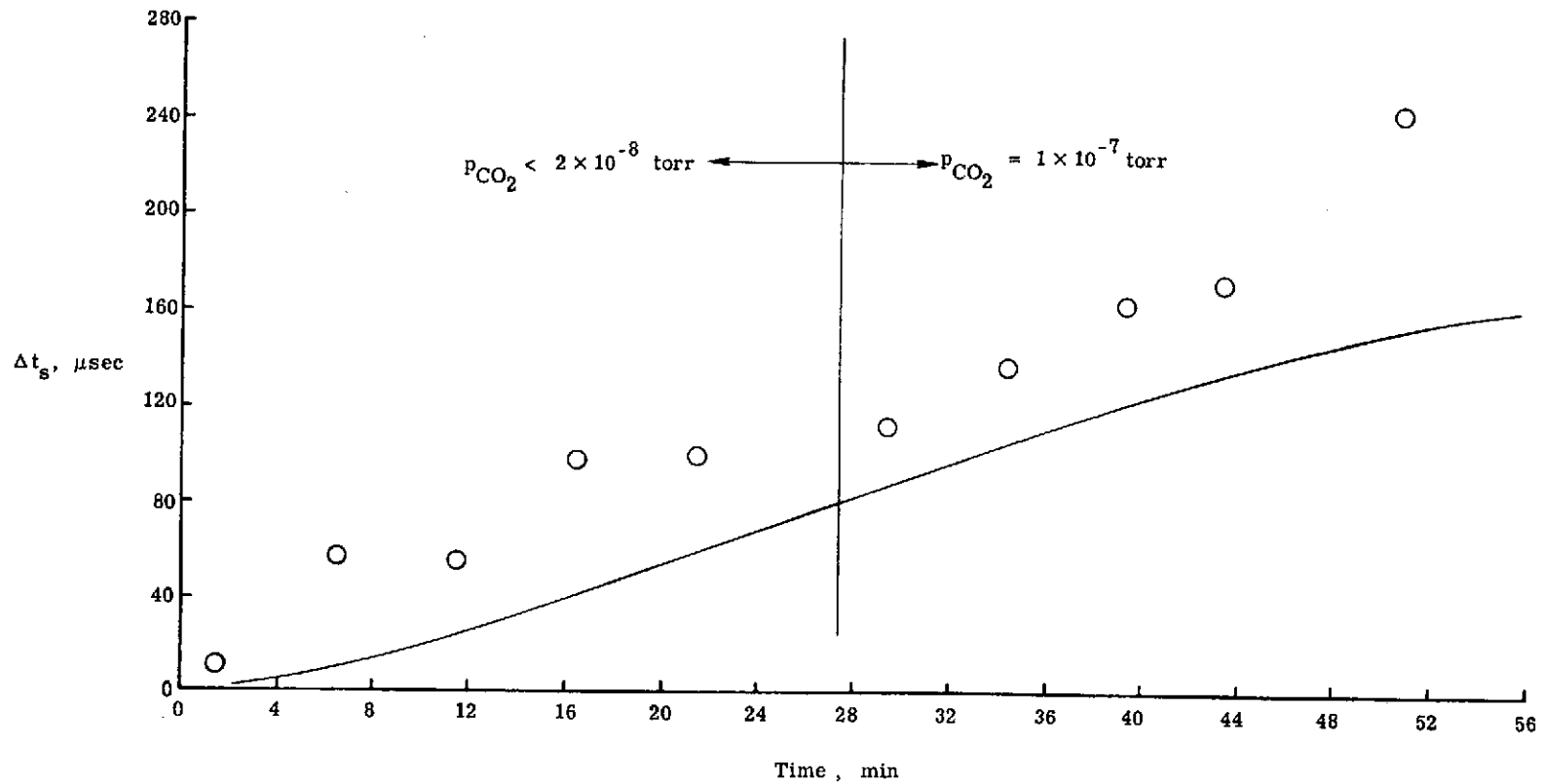
surface becomes saturated after an ion dose of about 5×10^{-6} C and that bombardment at a rate of 2×10^{-9} A can maintain saturation.

Time variations of the peak shift following cessation of ion bombardment are shown in Fig. 6.3.8. For each set of data, the ion dose prior to time zero was at least 5×10^{-6} C and ion bombardment was stopped at time zero. For Fig. 6.3.8(a), the sample was exposed only to the residual background gas. The background was at a pressure of 3 to 4×10^{-7} torr and consisted mostly of Xe from the molecular beam. Other gases, primarily N_2 , O_2 , H_2O and CO_2 , as determined by a mass spectrometer, contributed a partial pressure of about 2×10^{-8} torr. The effect of this exposure is seen to be a gradual increase in the peak shift with time which continued to very long times. For the data in Fig. 6.3.8(b)-(d), the partial pressures of CO_2 , H_2O , and Xe in turn were intentionally increased during the measurement sequence. For comparison, the data from Fig. 6.3.8(a) are shown as a solid line in these latter figures. If the increase in peak shift with time was due to adsorption of these gases, an increase in the partial pressure of these gases should alter the rate at which Δt_s increased. Both CO_2 and H_2O show a possible effect. After about 20 minutes exposure to CO_2 , the rate at which Δt_s is increasing seems to increase (based only on the last data point).



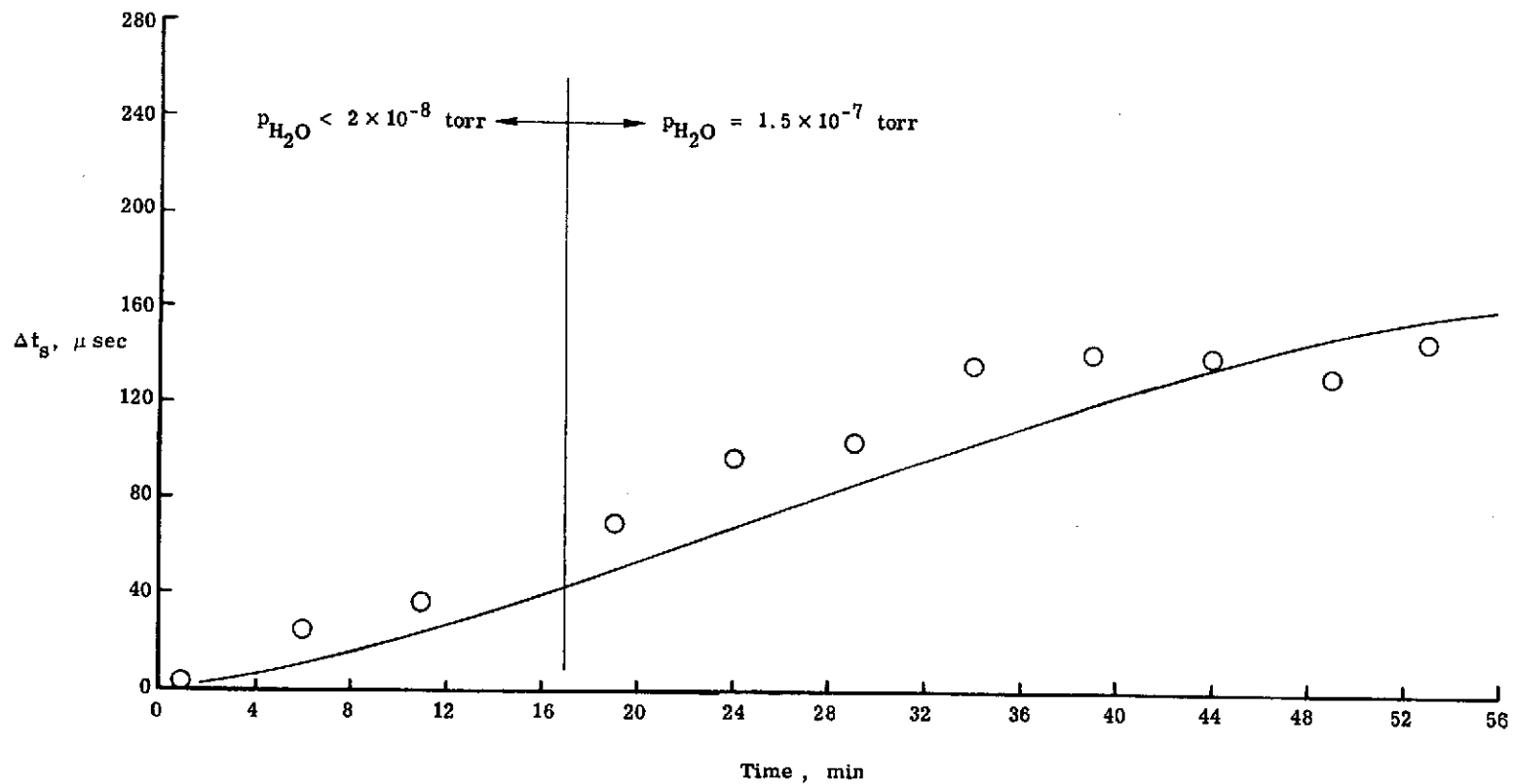
(a) Background only, $p_{\text{Xe}} = 3 \times 10^{-7}$ torr, $p_{\text{other}} = 2 \times 10^{-8}$ torr

Figure 6.3.8 Variation of Peak Shift with Time after Ion Bombardment for Different Background Pressures and Species, $\text{Xe} \rightarrow \text{Ni A+D}$, $T_s = 108^\circ\text{K}$



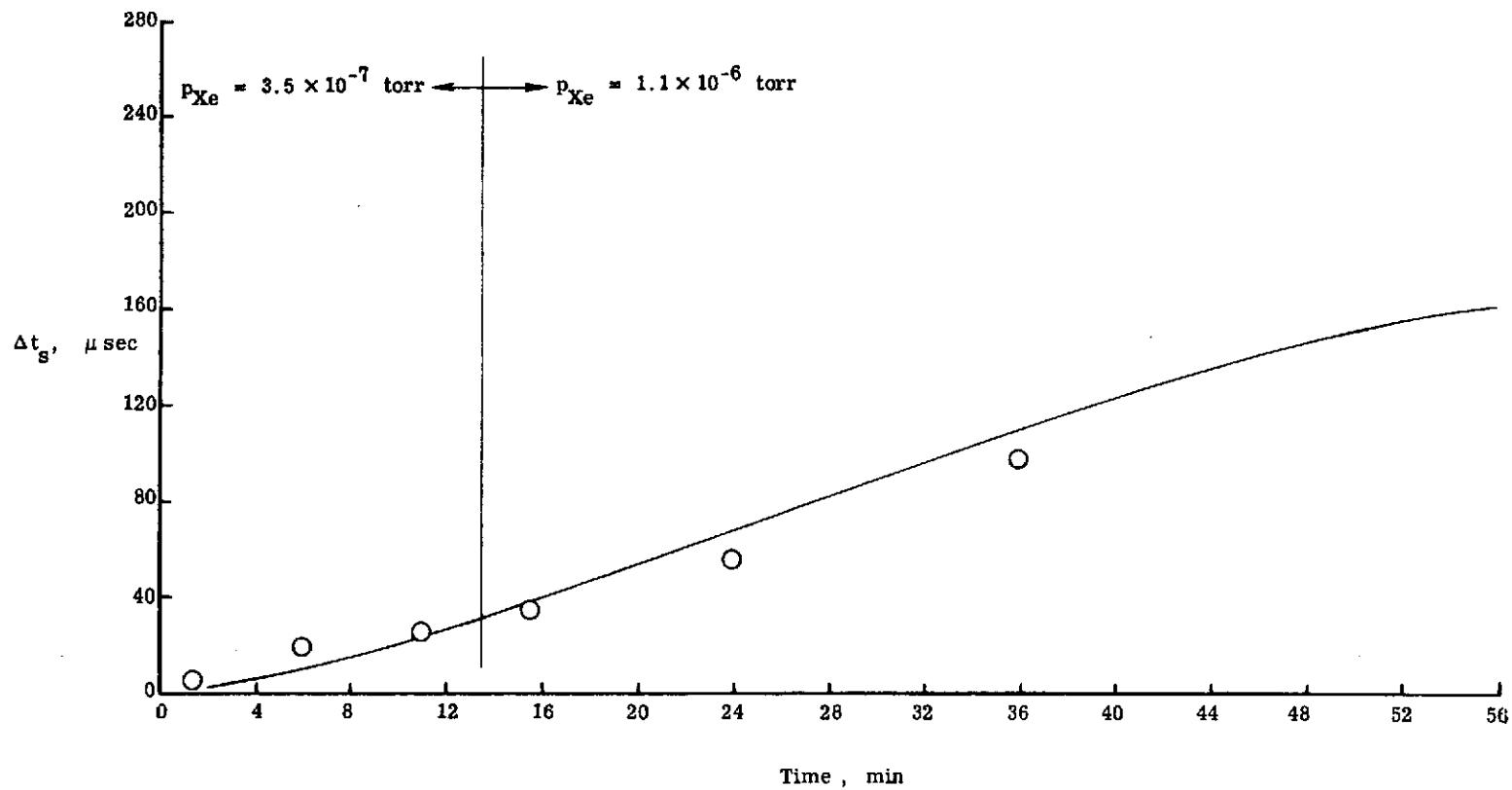
(b) Effect of increasing P_{CO_2}

Figure 6.3.8 continued (Solid curve is from part (a) of this figure.)



(c) Effect of increasing $p_{\text{H}_2\text{O}}$

Figure 6.3.8 continued (Solid curve is from part (a) of this figure.)



(d) Effect of increasing p_{Xe}

Figure 6.3.8 concluded (Solid curve is from part (a) of this figure.)

After about 20 minutes exposure to H_2O , the peak shift begins to level off with further exposure time. On the other hand, additional Xe exposure, even at much higher pressures, shows no significant change in the rate of Δt_s -increase. Thus, while CO_2 and H_2O adsorption may contribute to this change in Δt_s with time, it seems that some other factor is the driving force. It may be adsorption of some other species in the chamber or possibly the slow release of buried argon from the surface.

6.4 Binding Energy Results

The slopes and intercepts, E_0 and τ_0' , obtained by a least-squares fit of Eq. (5.2.3) to each set of peak-shift data are listed in Table 6.4.1. The 95% confidence intervals for each curve fit are listed in parentheses in terms of decades for τ_0' and in terms of percent of listed value for E_0 . The values of τ_0' are much smaller than typical vibrational periods for adsorbed atoms (10^{-12} to 10^{-14} sec) and show large fluctuations (comparable to the confidence intervals) from set to set. The values of E_0 are physically reasonable and fall within the range of values for heats of physical adsorption ($E_0/k = 500$ to $5000^\circ K$). However, the values of E_0/k for Xe and Kr on nickel are higher than those obtained by Baker and Fox⁽³⁵⁾ from equilibrium

TABLE 6.4.1

PREEXponential FACTORS τ_0' AND BINDING ENERGY TEMPERATURES E_0/k
 OBTAINED BY FITTING PEAK SHIFT DATA TO $\Delta t_s = \tau_0' \exp(E_0/kT_s)$

DATA SET	τ_0' , sec	E_0/k , °K
Xe → Cu	6.5×10^{-18} (10^{-19} - 10^{-16})	3397 (± 10%)
Xe → NiA	6.4×10^{-17} (10^{-17} - 10^{-16})	3213 (± 5%)
Xe → NiA+D	1.2×10^{-20} (10^{-24} - 10^{-16})	4155 (± 24%)
Xe → NiA+D+He ⁺	6.3×10^{-17} (10^{-18} - 10^{-16})	2916 (± 8%)
Xe → NiA+D+Ar ⁺	1.7×10^{-15} (10^{-17} - 10^{-13})	2594 (± 21%)
Xe → NiA+D+Xe ⁺	7.5×10^{-18} (10^{-32} - 10^{-3})	3010 (± 110%)
Xe → NiB+D	1.5×10^{-16} (10^{-18} - 10^{-15})	3116 (± 12%)
Xe → NiB+D+Ar ⁺	6.3×10^{-16} (10^{-16} - 10^{-15})	2735 (± 4%)
Kr → NiA+D	7.0×10^{-20} (10^{-23} - 10^{-16})	3278 (± 22%)
CO ₂ → NiA+D	4.2×10^{-18} (10^{-19} - 10^{-16})	3526 (± 8%)

95% confidence intervals for curve fit are given in parentheses.

adsorption measurements who found variations between 2200°K and 2700°K for both Xe and Kr.

In view of the large uncertainties involved in obtaining both τ'_0 and E_0 in the above manner, it was decided to estimate τ'_0 by some other means and then calculate E_0 from the peak shift data. For this approach, the theoretical predictions for mobile and local adsorption were used to predict τ'_0 and E_0/k was then computed for each data point. The average and standard deviation for the computed E_0/k values for each data set are tabulated in Table 6.4.2 first for the mobile adsorption case and then for the localized adsorption case. The respective values of τ'_0 are also tabulated there. (Since the τ'_0 for the localized model is more sensitive to temperature than τ'_0 for the mobile model, a range of values for τ'_0 is given for the localized case.)

Theoretical estimates of τ'_0 based on the localized-adsorption model agree better with the curve-fit estimates than do the mobile-model results. It follows that agreement for E_0/k is similarly described. Since the observed temperature dependence for Δt_s is not grossly different than that for the actual mean stay time, it is concluded that the localized adsorption model is the better one for these experiments. Moreover, the estimates of τ'_0 and E_0/k based on this model yield more intelligible comparisons between data sets than those derived strictly by curve-fitting.

TABLE 6.4.2

BINDING ENERGY TEMPERATURES OBTAINED FROM $\Delta t_s = \tau_0' \exp(E_0/kT_s)$
 USING THEORETICAL τ_0' BASED ON MOBILE AND LOCALIZED MODELS

DATA SET	Mobile		Localized	
	τ_0' , sec (Theoretical)	E_0/k , °K (Average)	τ_0' , sec (Theoretical)	E_0/k , °K (Average)
Xe → Cu	2.5×10^{-13}	2239 (± 3%)	$7.6-9.4 \times 10^{-17}$	3155 (± 1%)
Xe → Ni A	2.0×10^{-13}	2294 (± 2%)	$3.9-5.2 \times 10^{-17}$	3251 (± 0.3%)
Xe → Ni A + D	"	2302 (± 4%)	$3.9-4.8 \times 10^{-17}$	3239 (± 2%)
Xe → Ni A + D + He ⁺	"	2069 (± 2%)	$3.5-4.4 \times 10^{-17}$	2965 (± 0.4%)
Xe → Ni A + D + Ar ⁺	"	2080 (± 2%)	$3.5-4.8 \times 10^{-17}$	2996 (± 1%)
Xe → Ni A + D + Xe ⁺	"	1971 (± 4%)	$3.5-3.9 \times 10^{-17}$	2845 (± 1%)
Xe → Ni B + D	"	2305 (± 2%)	$3.7-5.2 \times 10^{-17}$	3251 (± 1%)
Xe → Ni B + D + Ar ⁺	"	2132 (± 2%)	$3.3-4.6 \times 10^{-17}$	3026 (± 0.3%)
Kr → Ni A + D	1.9×10^{-13}	1870 (± 1%)	$6.6-7.6 \times 10^{-17}$	2621 (± 1%)
CO ₂ → Ni A + D	2.0×10^{-13}	2281 (± 3%)	$1.4-1.7 \times 10^{-16}$	3108 (± 1%)

95% confidence intervals in average E_0/k based on n values for each data set are given in parentheses.

It can now be seen more clearly that small changes in binding energy produce order of magnitude changes in stay times. For Xe on Ni, the previously shown decrease in stay times by a factor of 10 to 100 due to ion bombardment is associated with a decrease in E_0/k of only about 7%. Similarly, the results for Kr on Ni indicate a binding energy some 20% lower than that for Xe or CO_2 on Ni even though at comparable T_s , the stay times might differ by a factor of 1000. Also, a binding energy for CO_2 on Ni lower than that for Xe and a higher τ_0' for CO_2 than that for Xe are consistent with the qualitative behavior in Fig. 6.3.6 where the peak shift data were comparable in magnitude for the two gases.

6.5 The Negative Dips in the Detector Signal

The negative dip in the detector signal was discussed briefly in Sec. 6.1. For this dip to occur, the background component of the detector signal must decrease temporarily through some interaction with the beam pulse. It was stated earlier that this interaction most likely occurred between molecules adsorbed on the surface. To support this statement, the probability of a number of other possible interactions must be considered. First, it can be stated that the geometry of the apparatus was such that

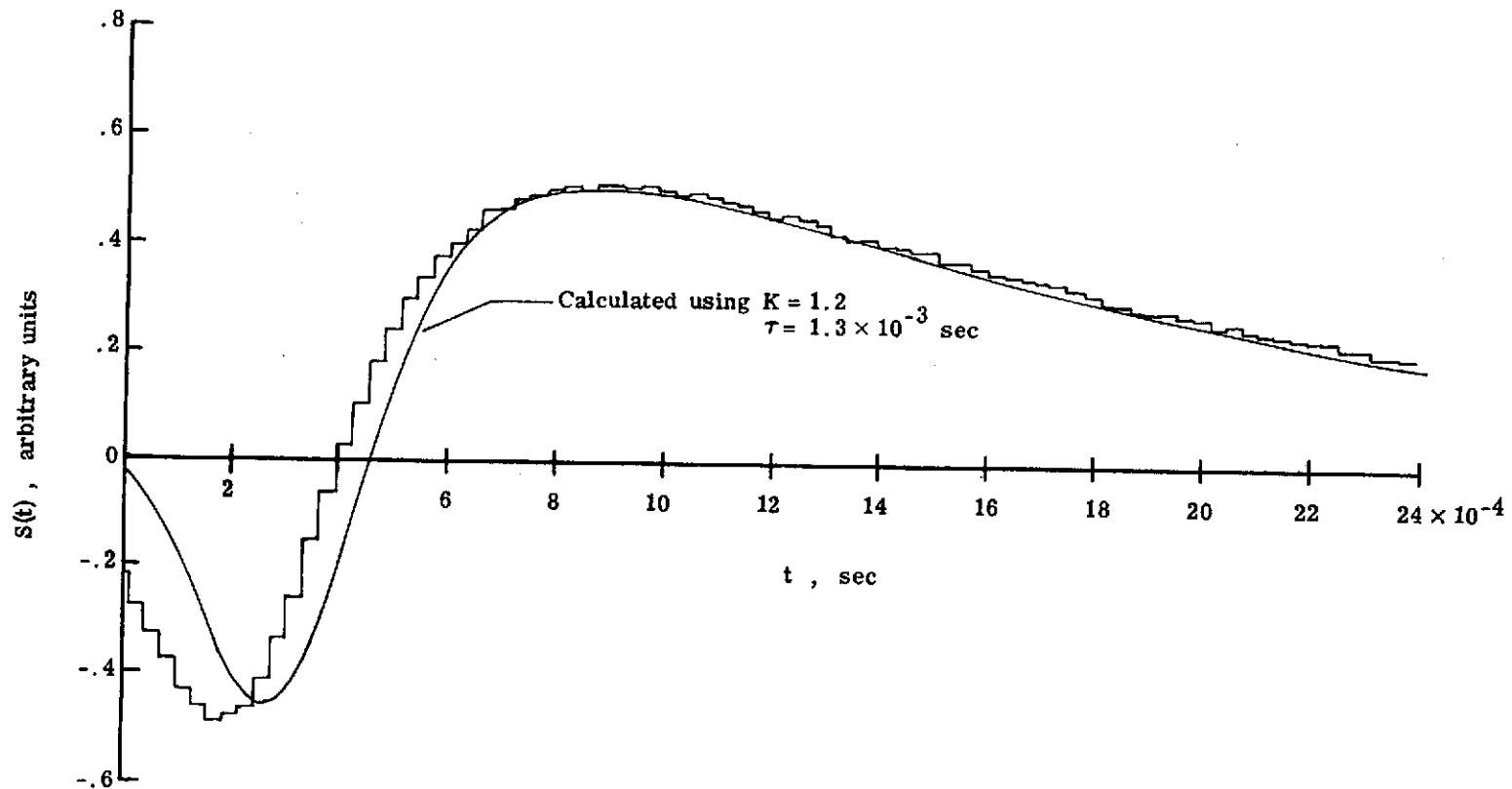
interactions between beam and background molecules passing through the chopper slots and from there directly into the detector did not contribute to this dip. This was verified in separate experiments in which an additional aperture was placed in front of the detector such that no direct line of sight existed between the chopper slots and the detector ionization zone. Second, collisions between beam and background molecules in the regions between the chopper, target and detector should be negligible. The mean free path of background molecules through gas at the density of the beam pulse is estimated to be at least 300 cm, much greater than the flight path lengths involved. Finally, the duration time between pulses was such that no anomalies due to pulse overlap should have occurred. For example, if the τ_2 data are a valid upper limit for the mean stay time for this type of signal, it is estimated that no greater than 5% of the molecules from the preceding beam pulse remained on the surface at the beginning of a new pulse even at the largest τ_2 encountered in these experiments. Thus, barring some unforeseen behavior, it seems that the beam-background interaction did occur most likely on the target surface.

To estimate the effects of these dips on the data reduction, an empirical model was developed. It was observed that the position of the "minimum" occurred near the position of the expected maximum for the detector signal

for zero stay time. This suggested that the observed signal might be modeled by the following superposition of two signals:

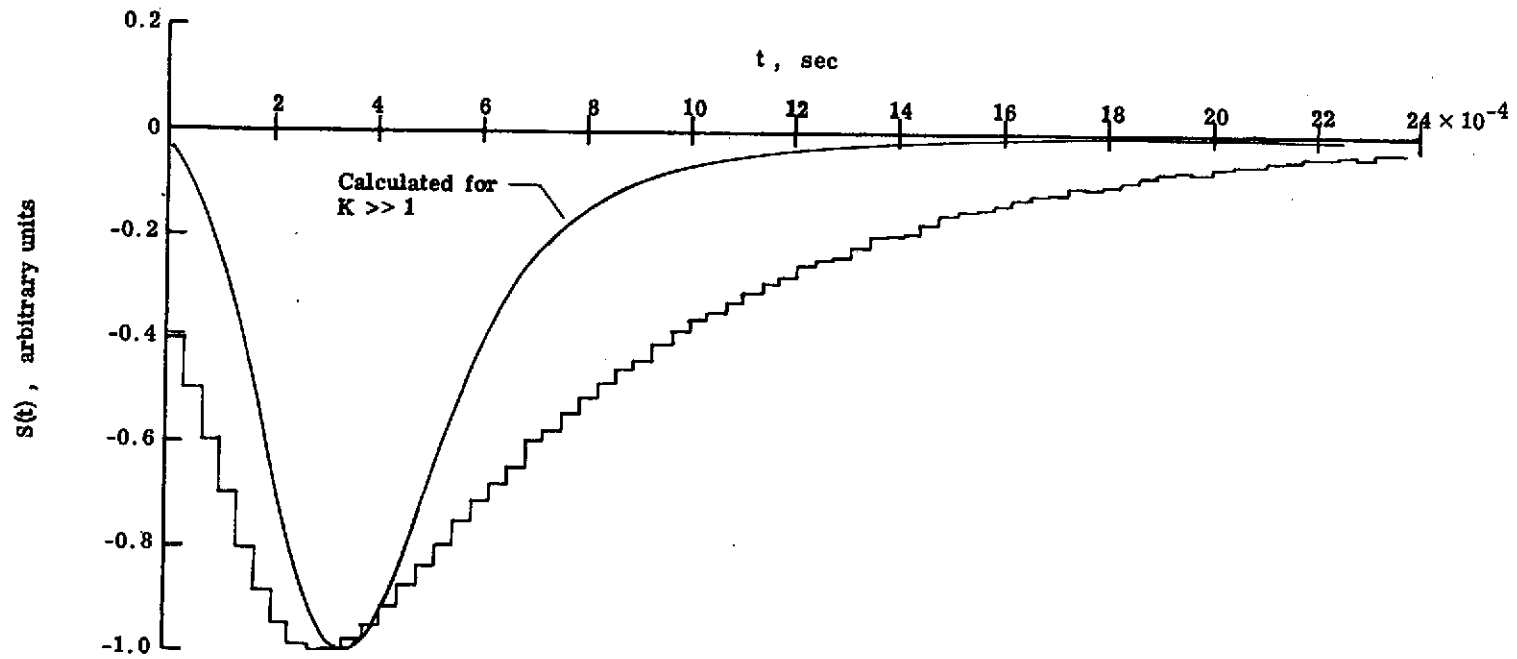
$$S(t, \tau, K) = S(t, \tau) - KS(t, 0) \quad (6.5.1)$$

where K is an adjustable constant. The function $S(t, \tau)$ represents the contribution to the detector signal from the desorbing molecular beam pulse. The term, $-KS(t, 0)$, represents the decrease in the contribution to the detector signal from the background gas. For given τ , temperature, and gas species, the functions $S(t, \tau)$ and $S(t, 0)$ were assumed to be given by Eq. (4.1.6). The combination of τ and K was found which gave the best fit to both the measured peak shift and the ratio of the positive to negative detector signal amplitudes $S_{\max}/|S_{\min}|$. Two typical comparisons of measured to modeled signals are shown in Fig. 6.5.1. In the first example, Fig. 6.5.1(a), the agreement is excellent for $t > t_m$, but the model's minimum occurs at a later time. In Fig. 6.5.1(b), the predicted and measured minimum position are in slightly better agreement, but clearly the model cannot account for the observed exponential-like rise in the negative portion of the signal. Signals of the shape shown in Fig. 6.5.1(b) imply that the stay times are long compared to the measurement times and therefore only the background



(a) $\text{Xe} \rightarrow \text{Ni A}$, $T_s = 108^\circ\text{K}$

Figure 6.5.1 Comparison of Empirical Model Predictions with Typical Detector Signals Showing Negative Dip



(b) $\text{Xe} \rightarrow \text{Cu}$, $T_s = 92^\circ\text{K}$

Figure 6.5.1 concluded

dip is observable in the signal. The majority of the recorded signals showing the negative dip were of the general shape shown in Fig. 6.5.1(a). The appearance of this type of signal depended on the magnitude of the stay time. It did not appear for peak shifts less than 10^{-4} sec for any of the test gases.

For one set of detector signals, values of τ were deduced using Eq. (6.5.1) for those signals showing the dip. The result of these calculations is shown in Fig. 6.5.2. It is seen that τ deduced in this manner shows better agreement with τ_2 than the values given in Fig. 6.1.2. The new analysis seems still to overpredict the stay time at large τ where τ_2 should be a reasonable upper limit for τ . However, this overprediction is not as great as that shown previously in Sec. 6.2.

Obviously, the empirical model gives little insight into the physical mechanisms behind the observed behavior. It seems that dips are indeed due to temporary reduction in the background-component desorption rate caused by the beam pulse. Such a reduction indicates that the effective binding energy increases with coverage. The fact that the magnitude of the dip minimum was observed to increase with decreasing temperature (increasing coverage) also supports this conclusion. Such an increase in binding energy has been observed by Baker and Fox⁽³⁵⁾ for xenon on nickel.

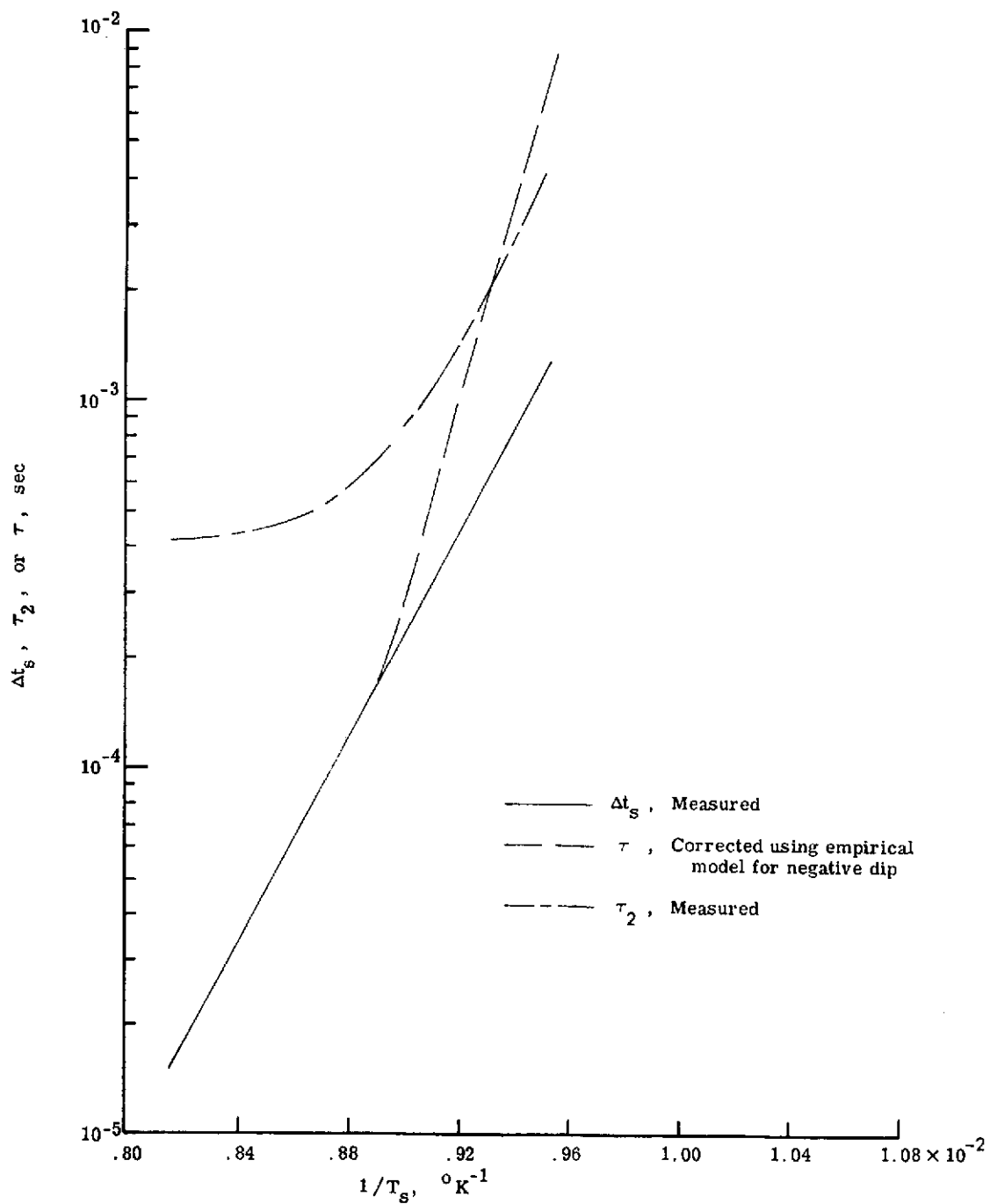


Figure 6.5.2 Example of Stay Time Obtained from Peak Shift Based on Empirical Model for Negative Dip, Xe \rightarrow Ni A

However, since the maximum coverage of beam gas species (beam pulse plus background component) is estimated to be a small fraction of a monolayer, it is difficult to see how interactions between beam-species atoms lead to the observed dip. Of course, there is a high probability that a significant coverage of other background species exists in this temperature. Suffice it to say that, in the absence of supporting information concerning the surface conditions, this behavior cannot be completely explained.

CHAPTER 7

SUMMARY AND CONCLUSIONS

It has been demonstrated that a molecular-beam time-of-flight approach is potentially powerful for the study of physical adsorption under non-equilibrium conditions. Only under non-equilibrium conditions can information about adsorption and desorption rates and probabilities be obtained. In particular, it has been shown that a mean stay time for molecules on the surface is a measurable quantity. It has also been observed that pronounced effects on the desorption pulse can occur due to what are apparently adsorbate-adsorbate interactions.

A model for the detected time-of-flight signal behavior has been developed assuming a first-order desorption process. This model predicts that, for a mean stay time τ comparable to or less than the mean transit times for the experiment, the detected signal is delayed by an amount approximately equal to this stay time. Therefore, the stay time can be estimated from the shift in the signal peak. For stay times much greater than these transit times, the model predicts that the signal decays as $\exp(-t/\tau)$ and τ can be estimated from this decay rate. For intermediate values of τ , no simple relationship between signal shape and τ exists. The shutter open time t_s has been shown to have negligible

effect on the peak shift due to stay time, but unless $\tau \gg t_s$, it may have significant effect on the decay rate.

From the experimental data, mean stay times have been estimated for the adsorption of Xe, Kr and CO₂ on copper and nickel surfaces as a function of surface temperature. The minimum detectable stay time for these experiments was found to be about 10^{-5} sec. For τ between 10^{-5} sec and 10^{-4} sec, τ was estimated from the measured peak shift. However, for $\tau > 10^{-4}$ sec, interpretation of the peak shift in terms of the stay time becomes progressively less certain primarily because of a peculiar negative dip in the detector signals which is attributed to adsorbate-adsorbate interactions.

The mean stay time has been found to be relatively independent of the surface materials and of the pre-vacuum surface preparations used in these experiments. This could be due to obscuring of the bulk material by a layer of physisorbed gases reaching the surface through the background gas as well as chemisorbed gases present prior to the experiments.

Ion bombardment of the nickel surface during Xe adsorption has been found to reduce the mean stay time at fixed T_s . Xe bombardment reduced the stay time typically by a factor of about 100 while Ar and He ion bombardment each reduced the stay time typically by a factor of 10. It is proposed that

this reduction results from burial of the neutralized ions near the surface. For argon ion bombardment, ion doses corresponding to about 0.1 monolayers were sufficient to stabilize the stay time at its reduced value.

Experiments were performed for Xe on Ni at fixed surface temperatures over a range of incident beam flux by varying the molecular beam source pressure. At the highest source pressure employed, the measured stay time and calculated beam flux indicate a surface coverage of about 10^{-3} monolayers. Decreasing the pressure to where the flux was halved had little effect on the stay time. However, reducing the pressure by a factor of 10 (flux by factor of 3) caused the stay time to decrease substantially.

The stay time for CO_2 on nickel was found to be comparable to that for Xe at the same surface temperature. Stay times of about the same magnitude were found for Kr on nickel only at temperatures about 20% lower.

The measured variation of the peak shift Δt_s with surface temperature was used to estimate adsorption binding energy and preexponential factors by fitting these data to a Frenkel-type relation, $\Delta t_s = \tau'_0 \exp(E_0/kT_s)$. However, systematic uncertainty and scatter in the peak-shift data are such that values of τ'_0 and E_0 determined by direct curve-fit to this relation show large uncertainties. Theoretical estimates of τ'_0 based on a localized adsorption

model were found to be in reasonable agreement with the values found by fitting. These values of τ_0' are quite low ($\sim 10^{-17}$ sec) and are not representative of typical vibrational periods for adsorbed atoms. Because of the high uncertainty in the fitted τ_0' and E_0/k values, the localized adsorption model estimates for τ_0' were used to obtain more reliable estimates of the relative values of E_0/k from the peak-shift data. The E_0/k value for Xe on nickel was thus found to be about 3250°K with a reduction to about 2850°K upon ion bombardment with Xe. For CO_2 and Kr on nickel, the values of E_0/k were 3100°K and 2600°K , respectively.

Comparisons of measured signal shapes to those predicted by a first-order desorption model show reasonably good agreement at small stay times (low coverage). The measured signal peak shifts at small stay times behaved with surface temperature as expected. Significant disagreement between measured and predicted decay rates at long detector times had little effect on the peak shift behavior and were attributable to shutter function approximations in the model. At the longer stay times encountered in these experiments, the adsorbate-adsorbate interactions, proposed to account for signals exhibiting the negative dip, obviously violate the assumption of first-order desorption. Still, at long measurement times in the detector signal, the signal decay rate was indicative of first-order desorption.

By far the most serious shortcoming of the present experiments is the uncertainty with regard to the nature of the surfaces. The relatively high partial pressures ($\approx 2 \times 10^{-8}$ torr) in the test chamber of species other than that in the molecular beam could have led to significant adsorption of these species. The presence of such adsorbates may well be the cause for the unexpected negative dips seen in the detected desorption signals. Uncertainty in the constancy and nature of the surface conditions also makes the interpretation of the effects of parameter variations correspondingly uncertain.

To improve on these experiments, the following recommendations are offered:

- (1) employ an ultra-high-vacuum test chamber capable of attaining residual pressures of about 10^{-10} torr (with sufficient pumping capacity to keep the pressure below about 10^{-6} torr with the molecular beam on);
- (2) use single crystal targets;
- (3) use in-situ cleaning techniques that allow the production of atomically clean surfaces (if ion bombardment is used, have the capability of heating the target sufficiently to remove buried ions and to anneal the surface);

- (4) employ in-situ analysis of surface, such as Auger spectroscopy;
- (5) maintain ability to vary incident flux in order to study the effect of adsorbate-adsorbate interactions;
- (6) investigate the effect of ion burial on adsorption (if the effect is as pronounced as it appears, it is potentially useful for altering surface adsorptive characteristics);
- (7) determine the physical mechanism which causes the negative signals (this might provide an approach to studying adsorbate-adsorbate interactions).

BIBLIOGRAPHY

1. Young, D. M. and A. D. Crowell, Physical Adsorption of Gases, Butterworths, Washington, 1962.
2. Langmuir, Irving, "The Evaporation, Condensation and Reflection of Molecules and the Mechanism of Adsorption," *Phys. Rev.* 8, 149 (1916).
3. Frenkel, J., "The Theory of Adsorption and Related Phenomena," *Z. Physik* 26, 117 (1924).
4. deBoer, J. H., The Dynamical Character of Adsorption, Oxford University Press, London, 2nd Ed., 1968.
5. deBoer, J. H., "Adsorption Phenomena," *Advances in Catalysis*, 8, 17, (1956).
6. Lennard-Jones, J. E. and C. Strachan, "The Interaction of Atoms and Molecules with Solid Surfaces: I - The Activation of Adsorbed Atoms to Higher Vibrational States," *Proc. Roy. Soc. A*, 150, 442, (1935).
7. Strachan, C., "The Interaction of Atoms and Molecules with Solid Surfaces: II - The Evaporation of Adsorbed Atoms," *Proc. Roy. Soc. A*, 150, 456 (1935).
8. Lennard-Jones, J. E. and A. F. Devonshire, "The Interaction of Atoms and Molecules with Solid Surfaces: III - The Condensation and Evaporation of Atoms and Molecules," *Proc. Roy. Soc. A*, 156, 6 (1936).
9. Lennard-Jones, J. E. and A. F. Devonshire, "The Interaction of Atoms and Molecules with Solid Surfaces: IV - The Condensation and Evaporation of Atoms and Molecules," *Proc. Roy. Soc. A*, 156, 29 (1936).
10. Pagni, P. J., "Comparison of Diffusion Theory Adsorption and Desorption Rates with Experimental Lifetimes," U. of Calif. Report No. ME-72-9 (1972).
11. Clausing, P., "Measuring Duration Time by Surface Tests," *Physica* 8, 289 (1929), (NASA TT F-13,669).

12. Clausing, P., "On the Adsorption Time and Its Measurement by Flow Experiments," *Ann. der Phys.* 7, 489 (1930).
13. Pollock, F., H. Logan, J. Hobgood, and J. G. Daunt, "Measurement of Molecule-Surface Binding Energies by a Time-of-Flight Diffusion Method," *Phys. Rev. Letters* 28, 346 (1972).
14. Leonas, V. B., "Study of Energy Transfer During the Collision of a Molecular Stream with a Surface," *Zhurnal Prikladnoi Mekhaniki i Tekhnicheskoi Fiziki*, No. 2, 84 (1965).
15. Bailey, W. F. Jr., "Measurement of Adsorption Stay Times of Several Atmospheric Gases on Stainless Steel," U. of Va. Report No. AEEP-4038-111-69U (1969).
16. Shelton, H. and A. Y. H. Cho, "Evaporative Lifetimes of Copper, Chromium, Beryllium, Nickel, Iron, and Titanium on Tungsten and Oxygenated Tungsten," *J. Appl. Phys.* 37, 3544 (1966).
17. Arthur, J. R. Jr., "Interaction of Ga and As₂ Molecular Beams with GaAs Surfaces," *J. Appl. Phys.* 39, 4032 (1968).
18. Cho, A. Y. and C. D. Hendricks, "Mean Adsorption Lifetimes and Activation Energies of Silver and Gold on Clean, Oxygenated, and Carburized Tungsten Surfaces," *J. Appl. Phys.* 40, 3339 (1969).
19. Hudson, J. B., "Mass Spectrometric Studies of Neutral Molecule-Surface Interactions," *J. Vac. Sci. Technol.* 7, 53 (1970).
20. Smith, J. N. Jr., J. Wolleswinkel and J. Los, "Residence Time Measurements for the Surface Ionization of K on W: The Effect of Surface Contaminants," *Surf. Sci.* 22, 411, (1970).
21. Meshcheryakov, N. A., "Investigation of Interaction Processes Between a Molecular Beam and the Silicon Surface," *Fizika i Tekhnika Poluprovodnikov* 3, 1262 (1970).

22. Meshcheryakov, N. A., "Experiment for Determining the Average Lifetime of Molecules on a Surface," *Zhurnal Tekhnicheskoi Fiziki* 41, 1478 (1972).
23. Ehrlich, G., "Modern Methods in Surface Kinetics," *Advances in Catalysis* 14, 255 (1963).
24. Wilmoth, Richard G., "Speed Distribution Measurements of N_2 and Ar Molecular Beams Produced by a Multichannel Source," *J. Vac. Sci. Technol.* 9, 1121 (1972).
25. Giordmaine, J. A. and T. C. Wang, "Molecular Beam Formation by Long Parallel Tubes," *J. Appl. Phys.* 31, 463 (1960).
26. Hagen, O. F., J. E. Scott, Jr., and A. K. Varma, "Design and Performance of an Aerodynamic Molecular Beam and Beam Detection System," U. Va. Report AST-4038-103-67U (1967).
27. Outlaw, R. A., "Gas-Surface Interactions Occurring on Materials within Ultrahigh Vacuum," Ph.D. Dissertation, V.P.I.S.U. (1972).
28. American Institute of Physics Handbook, McGraw-Hill, Inc., New York, 1957.
29. Dushman, S., Scientific Foundations of Vacuum Techniques, John Wiley and Sons, Inc., New York, 1962.
30. Olander, D. R., "Molecular-Beam Sources Fabricated from Multichannel Arrays, II, Effect of Source Size and Alignment," *J. Appl. Phys.* 40, 4650 (1969).
31. Laegreid, N. and G. K. Wehner, "Sputtering Yields of Metals for Ar^+ and Ne^+ Ions with Energies from 50 to 600 eV," *J. Appl. Phys.* 32, 365 (1961).
32. Johnson, R. E., Unpublished calculation, U. Va., 1973.
33. Hobson, J. P., "Pumping at Solid Surfaces," *Brit. J. Appl. Phys.* 14, 544 (1963).
34. Hirschfelder, J. O., C. F. Curtiss, and R. B. Byrd, Molecular Theory of Gases and Liquids, John Wiley and Sons, Inc., New York, 1954.

35. Baker, B. G. and P. G. Fox, "Physical Adsorption of Gases. Part 1. - Xenon and Krypton on Nickel Films," Trans. Farad. Soc. 61, 2001 (1965).
36. Reif, F., Fundamentals of Statistical and Thermal Physics, McGraw - Hill, Inc., New York, 1965.
37. Knuth, E. L., Introduction to Statistical Thermodynamics, McGraw - Hill, Inc., New York, 1966.
38. Kubo, R., Statistical Mechanics, North - Holland Publishing Co., Amsterdam, 1965.
39. Goodman, F., "Quantum-Mechanical Treatment of the One-Phonon Inelastic Scattering of Gas Atoms in Three Dimensions by a Simplified Continuum Model of a Solid," Surf. Sci. 30, 1 (1972).
40. Allen, R. E. and F. W. deWette, "Mean-Square Amplitudes of Vibration at a Surface," Phys. Rev. 188, 1320 (1969).
41. Jones, R. H., D. R. Olander, and V. R. Kruger, "Molecular-Beam Sources Fabricated from Multichannel Arrays. I. Angular Distributions and Peaking Factors," J. Appl. Phys. 40, 4641 (1969).

APPENDIX I

PREDICTED STAY TIMES FOR ADSORBED GASES

It was shown in Chapter 2 that the stay time is related to the number ratio, N_a/N_g , by

$$\tau = \left(\frac{2\pi m_g}{kT} \right)^{\frac{1}{2}} \frac{V}{A_s} \left(\frac{N_a}{N_g} \right) \quad (\text{AI.1})$$

for a steady-state adsorption process with unity adsorption probability. Stay time relations will now be derived for non-interacting, indistinguishable molecules in equilibrium with a surface for some specific models of the gas-surface interaction.

Mobile harmonic-oscillator model. In this model, the adsorbed gas is assumed to move freely in the two dimensions parallel to the surface. Molecules are assumed to be bound to the surface with energy $-E_0$ (the zero-energy level is taken to be at the beginning of the continuum state) and to be vibrating perpendicular to the surface as simple harmonic oscillators. At equilibrium, for non-interacting, indistinguishable molecules, the ratio, N_a/N_g , is given by

$$\frac{N_a}{N_g} = \frac{Q_a}{Q_g} \quad (\text{AI.2})$$

where Q_a and Q_g are the single-particle partition functions for the adsorbed phase and gas phase, respectively (for example, see Reif⁽³⁶⁾). If the gas is of sufficiently low density, the classical limit

$$Q_g = V (m_g kT / 2\pi\hbar^2)^{3/2} \quad (\text{AI.3})$$

may be used. The partition function Q_a may be written as

$$Q_a = Q_a^{\text{tr}} Q_a^{\text{vib}} \exp(E_0/kT) \quad (\text{AI.4})$$

where Q_a^{tr} = translational partition function;
 Q_a^{vib} = vibrational partition function.

The classical limit

$$Q_a^{\text{tr}} = m_g kT / 2\pi\hbar^2 \quad (\text{AI.5})$$

may be used for the translational part. For the vibrational part, however, it is appropriate to use the quantum-mechanical result for a one-dimensional, harmonic oscillator,

$$Q_a^{\text{vib}} = \frac{A_s}{2 \sinh \left(\frac{\hbar\omega_0}{2kT} \right)} \quad (\text{AI.6})$$

where ω_0 = frequency of vibration. (For evaluation of partition functions for adsorbed gases, see Reif⁽³⁶⁾ or Knuth⁽³⁷⁾.) Combining Eqs. (AI.1)-(AI.6), the stay time is found to be

$$\tau = \left[\frac{\hbar\omega_0/2kT}{\sinh(\hbar\omega_0/2kT)} \right] \tau_0 \exp(E_0/kT) \quad (\text{AI.7})$$

where $\tau_0 = 2\pi/\omega_0$ is the vibrational period.

Localized, harmonic oscillator model. In this case, consider the molecules to be bound so strongly in localized sites that their translational freedom is lost entirely. By accounting for the number of ways N_a atoms can be distributed over N_m sites (N_m corresponding to monolayer coverage), it can be shown⁽³⁸⁾ that

$$\frac{N_a}{N_g} = N_m \left(\frac{Q_a}{Q_g} \right) \quad (\text{AI.8})$$

For the localized case, $Q_a^{\text{tr}} = 1$. Treating the molecules as three-dimensional harmonic oscillators with frequencies ω_{\perp} and ω_{\parallel} for vibrations perpendicular and parallel to the

surface, respectively, the vibrational partition function is given by⁽³⁷⁾

$$Q_a^{\text{vib}} = \frac{1}{\left[2\sinh\left(\frac{\hbar\omega_{\parallel}}{2kT}\right)\right]^2 \cdot 2\sinh\left(\frac{\hbar\omega_{\perp}}{2kT}\right)} \quad (\text{AI.9})$$

The result for the stay time then becomes

$$\tau = \frac{4\pi^2\hbar^3 \left(\frac{N_m}{A_s}\right) \exp(E_0/kT)}{m_g(kT)^2 \left[2\sinh\left(\frac{\hbar\omega_{\parallel}}{2kT}\right)\right]^2 \cdot 2\sinh\left(\frac{\hbar\omega_{\perp}}{2kT}\right)} \quad (\text{AI.10})$$

Calculation of the vibrational frequencies. Characteristic frequencies for the surface atoms can be estimated from the Debye temperature θ_D of the solid, i.e.,

$$\omega = k\theta_D/\hbar \quad (\text{AI.11})$$

For surface atoms, a better estimate is obtained if a "surface Debye temperature" such as that defined by Goodman⁽³⁹⁾ is used, viz.,

$$\theta_{D,\text{surf}} = \theta_D / \rho \quad (\text{AI.12})$$

where ρ is the ratio of mean square displacement of a

surface atom to that of a bulk atom. Values of ρ have been calculated by Allen and deWette⁽⁴⁰⁾ and $\rho = 2$ is typically found. (There exists considerable variation in theoretical values of ρ as found in the literature. The quoted value represents the author's best estimate for both inert gases and metals based on the literature.) Assuming $\omega_o = \omega_l = \omega_{||} = k\theta_D/2\hbar$, Eqs. (AI.7) and (AI.10) become

for mobile case:

$$\tau = \left[\frac{\theta_D/4T}{\sinh(\theta_D/4T)} \right] \tau_o \exp(E_o/kT) \quad (\text{AI.13})$$

for localized case:

$$\tau = \frac{4\pi\hbar^2\sigma_m}{m_g k\theta_D} \frac{(\theta_D/2T)^2}{[2\sinh(\theta_D/4T)]^3} \tau_o \exp(E_o/kT) \quad (\text{AI.14})$$

where $\sigma_m = N_m/A_s$. Both relations can be written in the general form

$$\tau = \tau_o' \exp(E_o/kT) \quad (\text{AI.15})$$

These results differ from that of Frenkel only in terms of the preexponential factor τ_o' .

Sample calculations for Xe on Ni. Using $\theta_D = 413$ °K for nickel⁽²⁸⁾ and $\sigma_m = 4.8 \times 10^{14}$ atoms/cm² for the

monolayer coverage of Xe⁽²⁹⁾, the factor τ'_0 was calculated at $T = 100$ °K. The results are:

$$\begin{aligned}\tau_0 &= 2.3 \times 10^{-13} \text{ sec (Frenkel result);} \\ \tau'_{0,\text{mobile}} &= 1.9 \times 10^{-13} \text{ sec;} \\ \tau'_{0,\text{local}} &= 3.6 \times 10^{-17} \text{ sec.}\end{aligned}$$

It is seen that the preexponential factor for the localized case may be orders of magnitude below that for a mobile adsorbed layer. The factor τ'_0 is associated with the loss of entropy upon adsorption⁽⁴⁾ and thus, in the localized case, loses the meaning of a vibrational period.

APPENDIX II

CALIBRATION OF THE DETECTION SYSTEM AND CHARACTERIZATION OF THE MOLECULAR BEAM SOURCE

Ionization Detector. The flow-through-type ionization detector used in this study is sensitive to molecular density in the ionization region. The geometry of the system is similar to that used by Hagena, Scott, and Varma⁽²⁶⁾. It is different in that a 900 Oe magnetic field is used to confine the electron beam (compared to about 350 Oe in Ref. 26) and in that 1% thoriated (rather than pure) tungsten filaments are used, allowing operation at lower filament temperatures. The performance of the detector was determined in a small bell-jar vacuum system. The detector ion current was measured as a function of chamber pressure (indicated by a commercial, calibrated, hot-cathode ionization gauge), filament potential, anode potential and ion collector potential. A plot of measured ion current versus chamber pressure is shown in Fig. AII.1. The potentials listed in this figure are approximately those which gave maximum sensitivity for a given electron emission current. The ion current should be linearly proportional to the gas density within the detector's active zone. The observed variation with pressure is approximately linear with the standard deviation of all individual measurements from a least-

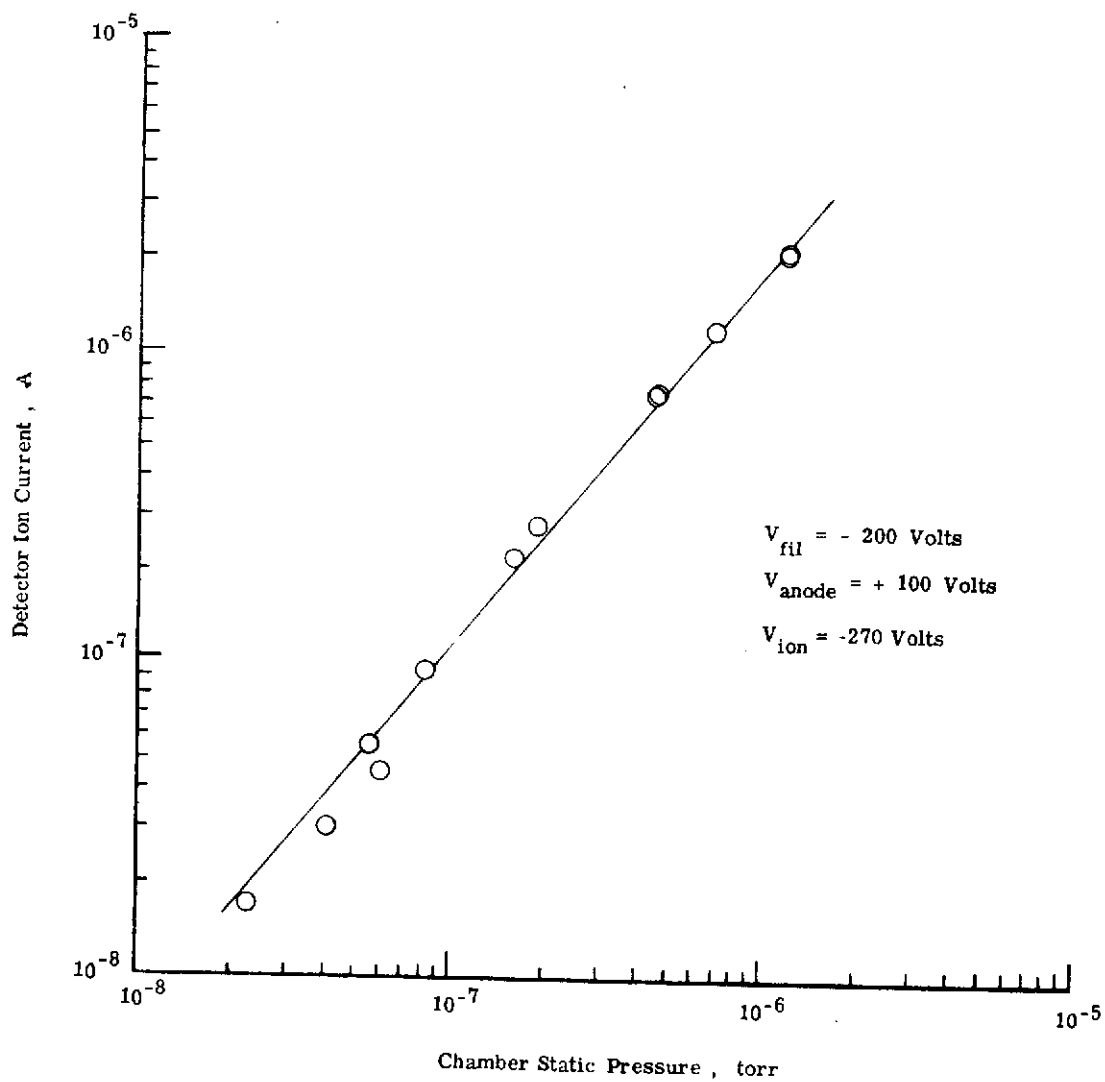


Figure AII.1 Variation of Detector Ion Current with Chamber Pressure, N_2 Gas, Emission Current = 10 mA.

squares straight line being about 9%. This deviation could well be due in part to lack of precision in the instrument used for measuring chamber pressure.

For the stay-time experiments, the signal is a time-varying pulse and the detector time response must be known. A straightforward way to evaluate this response is to use a pulsed molecular beam for which the detector density-versus-time is accurately known. For an orifice operating at a sufficiently large Knudsen number Kn (the ratio of mean free path in the source to orifice diameter) and pulsed with high time-of-flight resolution⁽²⁶⁾, the signal for a density sensitive detector is of the form

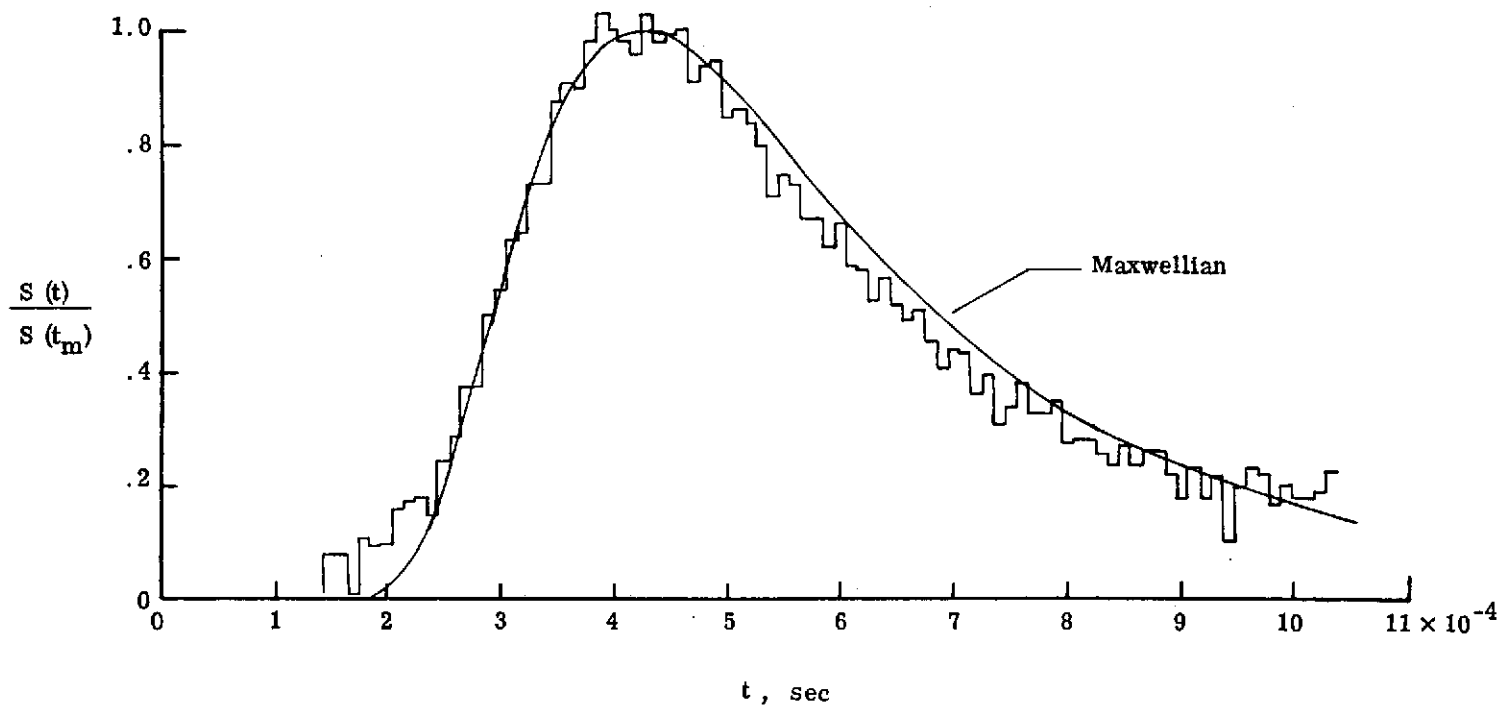
$$S(t) \propto \frac{1}{t^4} \exp(-\beta_0^2 L^2/t^2) \quad (\text{AII.1})$$

where t = flight time,

$$\beta_0 = \sqrt{m/2kT_0},$$

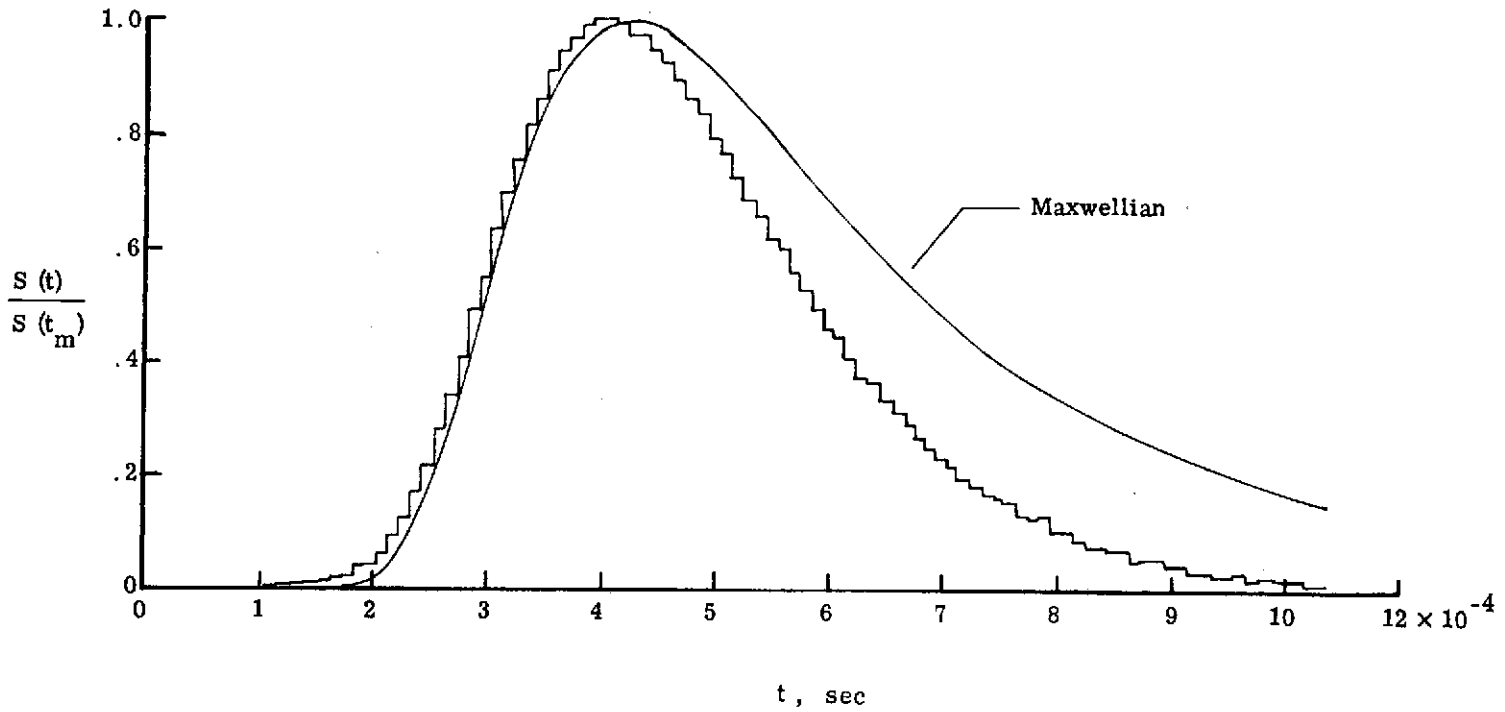
L = flight path length.

Detector signals were obtained using a 0.04 cm diameter single-orifice source with nitrogen gas. The results are shown in Fig. AII.2 for two values of Kn . For comparison, the corresponding Maxwellian distribution from Eq. (AII.1) is plotted in this figure. The agreement between measured and predicted results is very good for $Kn = 5.7$ but not for



(a) $Kn = 5.7$

Figure AII.2 Comparison of Measured to Predicted Incident Beam Time-of-Flight Distributions for a Single-Orifice Source, N_2 Gas



(b) $Kn = 0.6$

Figure AII.2 concluded

$Kn = 0.6$. At $Kn = 5.7$, the measured most probable time t_m was within $\pm 1\%$ of that predicted by free-molecular theory; the measured signal time-width at $\frac{1}{2}S(t_m)$ for $Kn = 5.7$ was within $\pm 6\%$ of the theoretical value. The assumption of free-molecular effusion through the orifice at $Kn = 0.6$ is no longer justified and the actual disagreement is similar to that generally observed in this Kn range.

As a result of a series of measurements of this type and their comparison to theory and previous experiments, it can be stated that the detector signals were representative of the time variation of density within the detector's ionization region.

Multichannel Molecular Beam. Following the tests described above, the detector system was used to characterize the molecular beam produced by the multichannel source. For the stay-time experiments, the properties of interest are the intensity and the speed distribution on the beam axis. Also, since the small diameter channels of the multichannel source were highly susceptible to blockage by dust particles, it was important to periodically determine the intensity during the stay-time experiments to ensure that no blockage occurred. Since direct measurements of the intensity required removal of the target and relocation of the detector, the centerline intensity I_0 was estimated indirectly by

$$I_0 = X^2/\pi \quad (\text{AII.2})$$

where χ is the peaking factor defined by Jones, Olander, and Kruger⁽⁴¹⁾ and λ is the total molecular flow rate. By definition, the peaking factor is the ratio of the center-line intensity to that from an effusive source emitting with a cosine distribution at the same total flow rate. This ratio was determined from intensity measurements using the effusive source described earlier and the multichannel source and was found to be about 6.6 for nitrogen. Although no measurements of χ were made for other gases, χ was estimated to be about 5 for Xe using Eq. (10) of Ref. 41.

The total flow rate through the multichannel source is related to the upstream number density n_0 by the expression

$$\lambda = n_0 C \quad (\text{AII.3})$$

where C is the source conductance. Knowing the source chamber pressure, temperature and volume, this conductance was determined by measuring the decay of the source chamber pressure with time with the gas supply shut off. The results of a typical measurement of the pressure decay is shown in Fig. AII.3. For xenon at a temperature of 295 °K, the conductance was found to be 8×10^{-5} l/sec, within 1% of that predicted by kinetic theory. This result was confirmed by several separate measurements made periodically during the course of the stay-time experiments. Using these results in

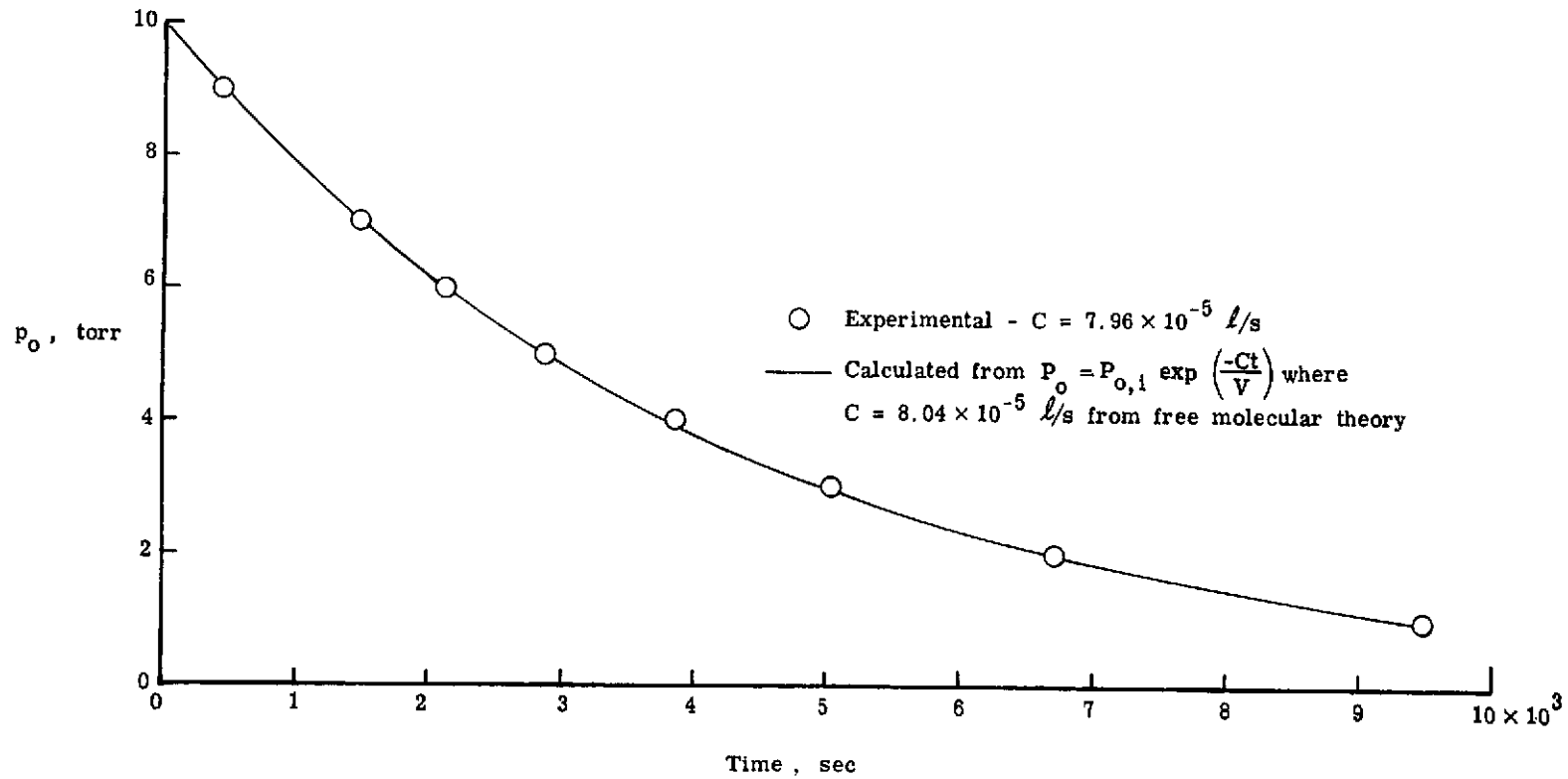


Figure AII.3 Typical Measured Source Pressure Decay with Time
 Used for Multichannel-Source Conductance
 Determination, Xe Gas

Eqs. (AII.2) and (AII.3), the centerline intensity was calculated to be 4.5×10^{16} atoms \cdot ster $^{-1}$ \cdot sec $^{-1}$ for xenon. The corresponding centerline flux at a target 3.6 cm from the source exit is then about 3.4×10^{15} atoms \cdot cm $^{-2}$ \cdot sec $^{-1}$. The uncertainty in the flux determined in this way is primarily due to the uncertainty in the peaking factor. The quoted value for Xe is believed to be accurate only to within a factor of 2. Whatever the factor, the flux was constant within $\pm 1\%$ for the experiments (except when source pressure was intentionally varied).

Characterizations of N_2 and Ar beams produced by the multichannel source have been reported in a separate study⁽²⁴⁾. A typical measured time-of-flight signal for N_2 taken from this study is shown in Fig. AII.4 where it is compared to the Maxwellian time-of-flight distribution predicted by Eq. (AII.1). The measured distribution is narrower than the Maxwellian and results in a mean molecular energy some 25 to 30 % higher than that for the Maxwellian distribution. This is attributed in Ref. 24 primarily to collisions at the exit of the multichannel array. Although no direct beam time-of-flight measurements were made for the gases used in the present stay-time experiments, these gases are not expected to produce significantly different distributions since the Kn for the present study is not much different from that for the distribution in Fig. AII.4.

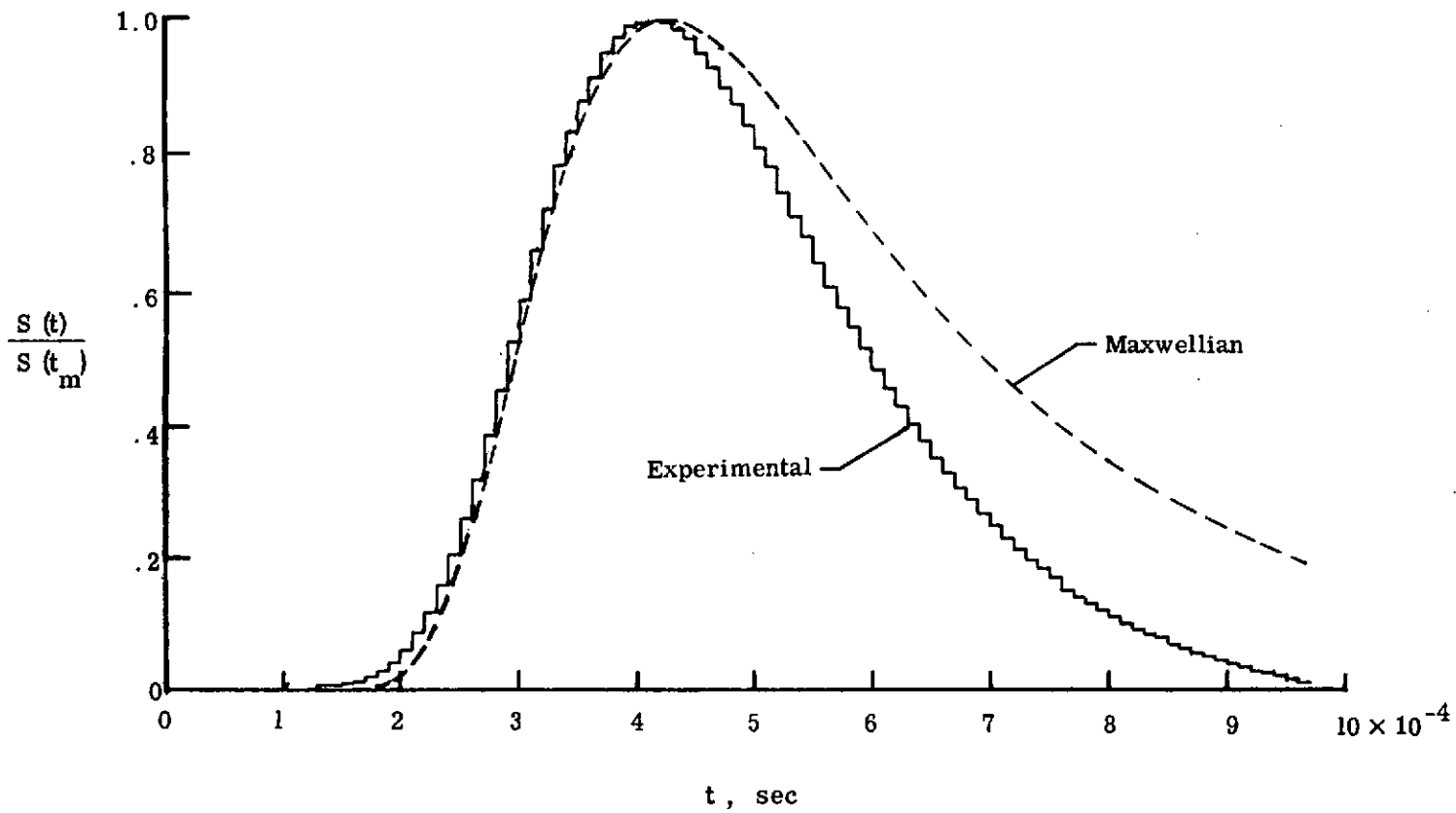


Figure AII.4 Comparison of Measured Incident Beam Time-of-Flight Distribution for Multichannel Source to Maxwellian Prediction, $p_0 = 10$ torr, N_2 Gas

APPENDIX III

DERIVATION OF THE EQUATIONS FOR THE SHAPE OF THE INCIDENT AND DESORPTION PULSES

An approximation for the shape of the incident flux pulse $F_1(t)$ is developed in this appendix. This approximation is then used to predict the form of the desorption pulse for a first-order rate process.

Incident Pulse. Consider a molecular beam with uniform flux F_0 such that the rate at which molecules with speeds between v and $v + dv$ strike an element of area dA_s at a particular downstream location is given by

$$dF_0 = Cv f_0(v) dv \quad (\text{AIII.1})$$

In this expression, $f_0(v)$ is the incident beam speed distribution and C is a constant of proportionality. Since only the timewise shape of the pulse is of interest, all factors affecting only the pulse amplitude will be included in the constant C . A shutter is now introduced between the source and target at a distance x_1 from the target with a function $g(t')$ representing the instantaneous fraction of molecules that pass through this shutter between t' and $t' + dt'$

headed for dA_s . The flux incident upon dA_s at time t is then

$$F_i(t) = \int_{-\infty}^t g(t') \frac{dF_o}{dv} \left| \frac{dv}{d(t-t')} \right| dt' \quad (\text{AIII.2})$$

Substituting $v = x_1/(t-t')$ gives the result

$$F_i(t) = F_o \int_{-\infty}^t \frac{1}{(t-t')^3} f_o\left(\frac{x_1}{t-t'}\right) g(t') dt' \quad (\text{AIII.3})$$

It is now assumed that the incident beam has a Maxwellian speed distribution, i.e., that

$$f_o\left(\frac{x_1}{t}\right) \propto t^{-2} \exp(-\beta_o^2 x_1^2/t^2) \quad (\text{AIII.4})$$

(Although the beam produced by the multichannel source does not have this distribution exactly, it will be shown that, for small x_1 , the shape of $F_i(t)$ is only weakly dependent on $f_o(x_1/t)$.)

The shutter function for a uniform beam of rectangular cross section with width equal to the chopper slot width is the triangular function

$$\begin{aligned} g(t) &= 1 + t/t_s && \text{for } -t_s < t < 0 \\ &= 1 - t/t_s && \text{for } 0 < t < t_s \\ &= 0 && \text{otherwise.} \end{aligned} \quad (\text{AIII.5})$$

where $2t_s$ is the basewidth of the triangle. It can be shown that, if t_s is allowed to become very large compared to any transit times and stay time, the resulting detector signal will approach the shape of $g(t)$. This fact was used experimentally to measure the effective value of t_s (see Sec. 5.2). In addition, based on these measurements, the shape of the true $g(t)$ was approximately determined and found to be nearly Gaussian, i.e., $g(t) \propto \exp(-Bt^2/t_s^2)$. Thus, for the present experiments, Eq. (AIII.5) describes the shutter function only approximately. (It can further be shown that the detector signals predicted in Chapter 4 are sensitive mainly to the effective width and not to the exact shape of $g(t)$, even for $t_s \approx \beta_s x_2$.)

Substituting Eqs. (AIII.4) and (AIII.5) into Eq. (AIII.3) and integrating yields

for $-t_s < t < 0$;

$$\frac{F_i(t)}{F_o} = \frac{1}{2}(1+t/t_s) \exp\left[-\left(\frac{\delta}{t+t_s}\right)^2\right] - \frac{1}{2}\sqrt{\pi}(\delta/t_s) \left[1 - \operatorname{erf}\left(\frac{\delta}{t+t_s}\right)\right]$$

for $0 < t < t_s$:

$$\frac{F_i(t)}{F_o} = \frac{1}{2}(1+t/t_s)\exp\left[-\left(\frac{\delta}{t+t_s}\right)^2\right] - (t/t_s)\exp\left[-(\delta/t)^2\right] \\ + \frac{1}{2}\sqrt{\pi}(\delta/t_s)\left[\operatorname{erf}\left(\frac{\delta}{t+t_s}\right) - 2\operatorname{erf}(\delta/t) + 1\right]$$

for $t_s < t$:

$$\frac{F_i(t)}{F_o} = \frac{1}{2}(1+t/t_s)\exp\left[-\left(\frac{\delta}{t+t_s}\right)^2\right] - (t/t_s)\exp\left[-(\delta/t)^2\right] \\ - \frac{1}{2}(1-t/t_s)\exp\left[-\left(\frac{\delta}{t-t_s}\right)^2\right] \\ + \frac{1}{2}\sqrt{\pi}(\delta/t_s)\left[\operatorname{erf}\left(\frac{\delta}{t+t_s}\right) - 2\operatorname{erf}(\delta/t) + \operatorname{erf}\left(\frac{\delta}{t-t_s}\right)\right]$$

(AIII.6)

where $\delta = \beta_o x_1$. Eq. (AIII.6) was evaluated for several values of t_s/δ covering the range of values expected in the stay-time experiments. The result for $t_s/\delta = 10$ is shown as the solid curve in Fig. AIII.1. The fact that the calculated shape very nearly corresponds to the assumed triangular shutter function shows that the incident beam speed distribution is not of much importance for values of t_s/δ as large as this. To first approximation, only the mean transit time

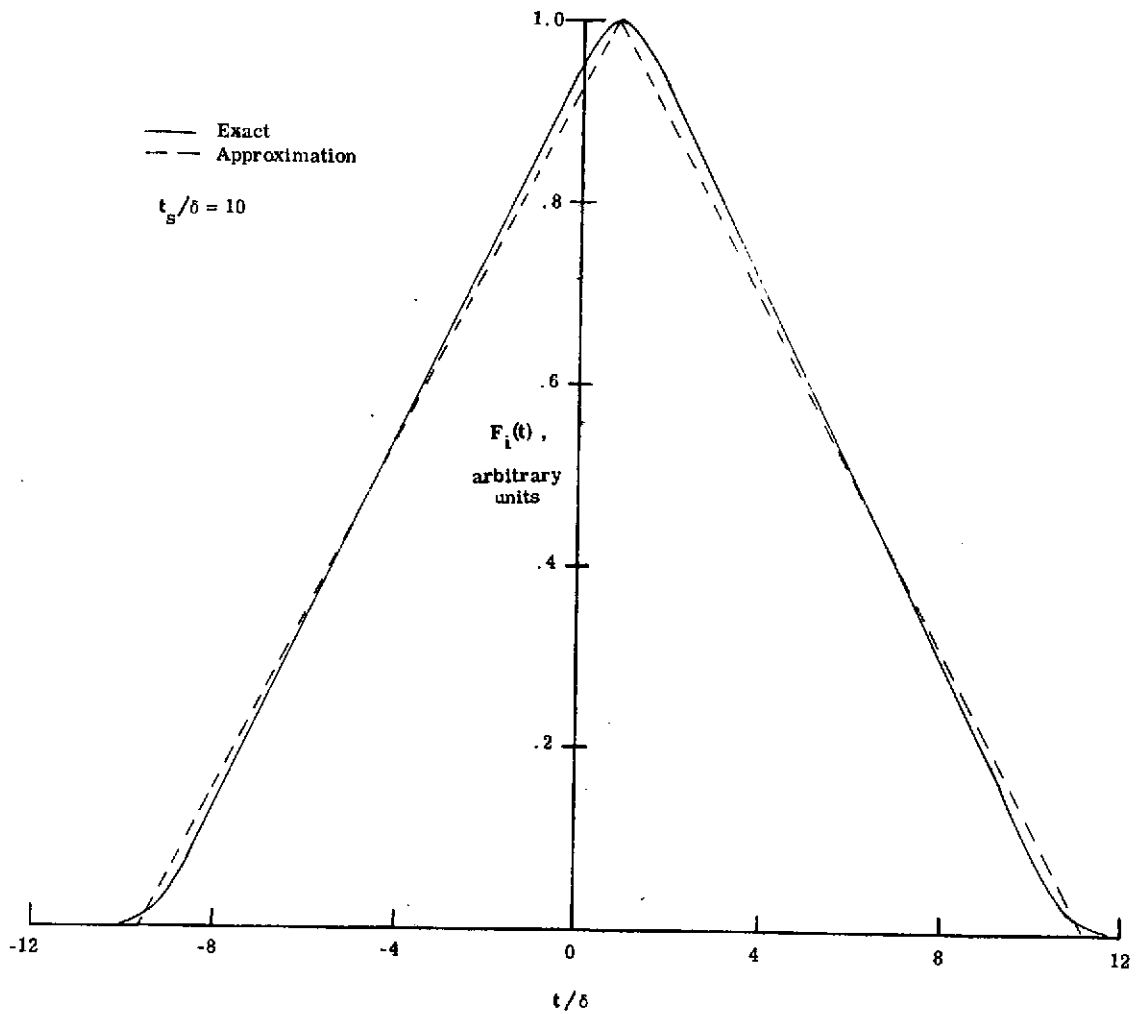


Figure AIII.1 Comparison of Exact with Approximate Prediction for the Incident Beam Pulse Shape

is important. The approximation

$$\begin{aligned}
 \frac{F_i(t)}{F_o} &\approx g(t-t_{o1}) \\
 &= 1 + (t-t_{o1})/t_s && \text{for } -t_s < (t-t_{o1}) < 0 \\
 &= 1 - (t-t_{o1})/t_s && \text{for } 0 < (t-t_{o1}) < t_s \\
 &= 0 && \text{otherwise}
 \end{aligned}$$

(AIII.7)

where $t_{o1} = \delta/\sqrt{2}$, is also shown in this figure for comparison. Since t_s/δ was always greater than 10 in these experiments, the approximate expression for $F_i(t)$ is used in interpreting the recorded detector signals.

Desorption Pulse. For first-order desorption, the adsorbate coverage is related to $F_i(t)$ through the following integral expression:

$$\sigma_a(t) = \tau F_o \exp(-t/\tau) \int_{-\infty}^t \frac{F_i(t')}{F_o} \exp(t'/\tau) dt'$$

(AIII.8)

Substituting Eq. (AIII.7) into the above and integrating

gives

for $-t_s < (t-t_{o1}) < 0$;

$$\frac{\sigma_a(t)}{\tau F_o} = 1 + (t-t_{o1}-\tau)/t_s + (\tau/t_s) \exp\left[-\left(\frac{t+t_{o1}-t_s}{\tau}\right)\right]$$

for $0 < (t-t_{o1}) < t_s$;

$$\begin{aligned} \frac{\sigma_a(t)}{\tau F_o} = & 1 - (t-t_{o1}-\tau)/t_s - 2(\tau/t_s) \exp\left[-\left(\frac{t-t_{o1}}{\tau}\right)\right] \\ & + (\tau/t_s) \exp\left[-\left(\frac{t-t_{o1}+t_s}{\tau}\right)\right] \end{aligned}$$

for $0 < (t-t_{o1})$;

$$\begin{aligned} \frac{\sigma_a(t)}{\tau F_o} = & (\tau/t_s) \exp\left[-\left(\frac{t-t_{o1}-t_s}{\tau}\right)\right] - 2(\tau/t_s) \exp\left[-\left(\frac{t-t_{o1}}{\tau}\right)\right] \\ & + (\tau/t_s) \exp\left[-\left(\frac{t-t_{o1}+t_s}{\tau}\right)\right] \end{aligned}$$

(AIII.9)

The quantity, τF_o , is simply the surface coverage that would be obtained if the beam was not pulsed (i.e., chopper removed). (It should be noted that, if the actual beam cross-section is greater than the chopper slot-width, the maximum coverage for the pulsed case will differ from τF_o by some fixed geometrical factor.)

The ratio, $\sigma_a(t)/\tau F_0$, is plotted versus the non-dimensional time t/δ in Fig. AIII.2 for several values of τ/t_s . For $\tau/t_s = 0.1$, the shape of the desorption pulse (desorption flux equal to $\sigma_a(t)/\tau$) is essentially the shape of the incident pulse only delayed by an amount τ/δ . On the other extreme, for $\tau/t_s = 5$, the desorption pulse decays at large t/δ approximately as $\exp(-t/\tau)$.

An important feature of the predicted desorption pulse is shown by examining the behavior of $\sigma_a(t)$ at large τ/t_s . It can be shown that

$$\lim_{\tau/t_s \rightarrow \infty} \frac{\sigma_a(t)}{\tau F_0} \Big|_{t=t_m} = \frac{t_s}{\tau} \quad (\text{AIII.10})$$

Thus for $\tau \gg t_s$, the maximum surface coverage is linearly proportional to the effective shutter open time.

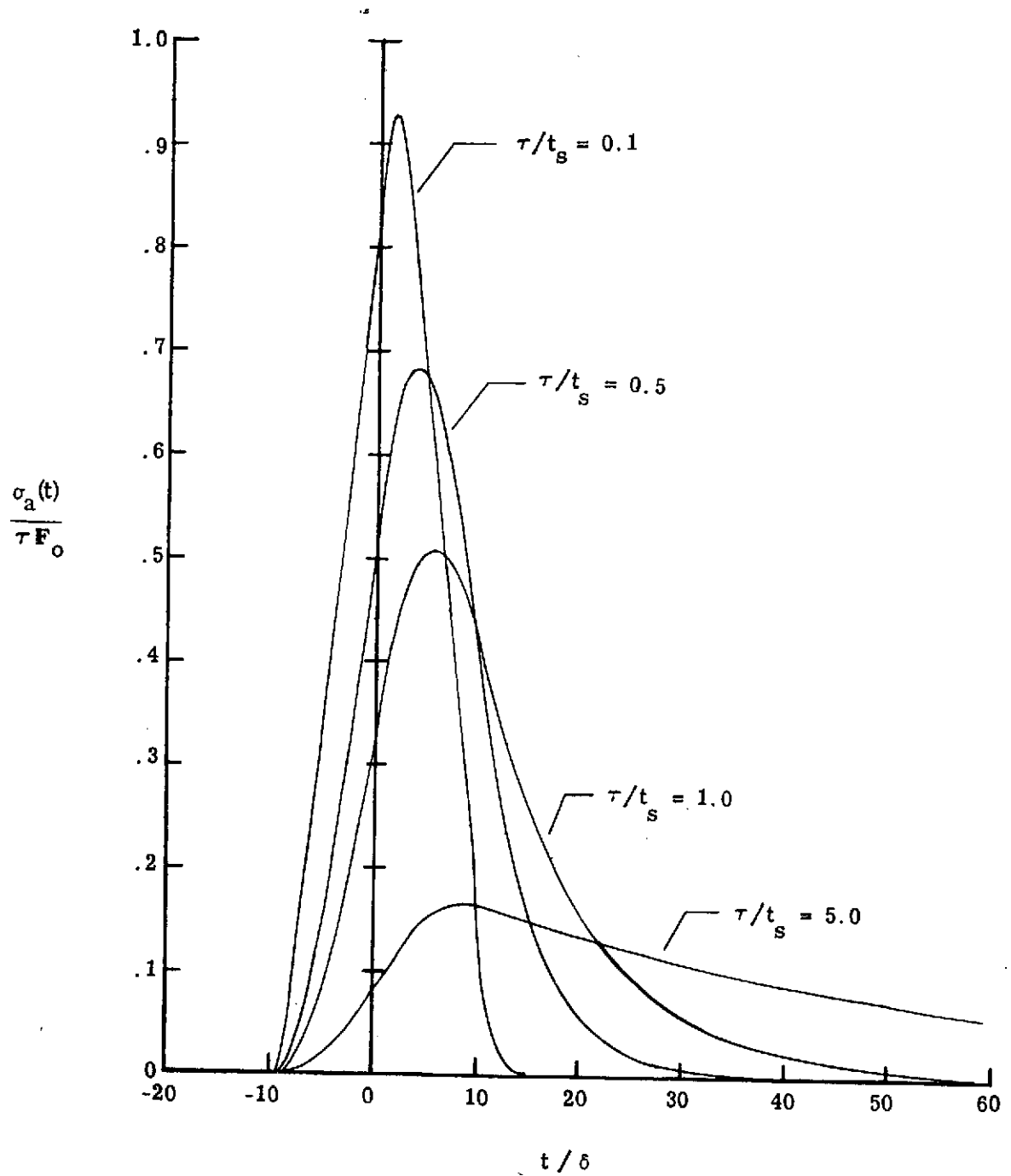


Figure AIII.2 Predicted Shape of the Desorption Pulse for Different Ratios of Stay Time to Incident Pulse Duration Time, $t_s/\delta = 10$

APPENDIX IV

TABULATION OF STAY-TIME PARAMETERS

The stay-time parameters obtained from the recorded detector signals for each of the data sets are listed in Table AIV.1. Although the values of τ calculated from Δt_s are in error for $\Delta t_s > 10^{-4}$ sec, they are listed here for reference and to indicate the relation of τ to the measured peak shift.

TABLE AIV.1

TABULATION OF STAY-TIME PARAMETERS

DATA SET	T_s , °K	Δt_s , μsec	τ_2 , μsec	τ , μsec
Xe - Cu	116.7	25	350	25
	114.1	58	391	60
	110.4	151	517	234
	108.1	308	706	996
	105.3	738	1548	9704
	102.4	1450	3774	$> 10^4$
Xe + NiA	122.7	14	408	14
	119.7	32	431	31
	117.1	55	474	56
	113.7	110	501	140
	111.4	207	822	426
	108.1	538	1637	4069
	104.9	1275	4289	$> 10^4$
Xe + NiA+D	117.0	27	367	27
	114.1	74	415	80
	111.1	218	970	471
	108.2	730	1003	9624
	105.1	1335	--	$> 10^4$
Xe + NiA+D+He ⁺	111.2	16	382	16
	108.3	32	380	32
	105.3	66	430	71
	102.3	139	635	203
	99.1	404	1115	1811
Xe + NiA+D+Ar ⁺	117.0	11	359	11
	114.1	12	354	12
	111.2	19	383	23
	108.3	31	451	31
	105.2	77	407	85
	102.4	176	618	306
	98.6	602	1094	5122
Xe + NiA+D+Xe ⁺	105.0	20	378	20
	102.5	46	426	47
	98.7	126	636	173
Xe + NiB+D	122.6	15	688	14
	119.8	30	730	30
	117.0	45	817	45
	114.2	119	751	157
	111.0	245	1180	602
	108.3	594	2040	5348
	105.2	1404	2611	$> 10^4$
Xe + NiB+D+Ar ⁺	113.9	18	370	18
	111.1	29	344	29
	108.1	62	400	65
	104.9	123	552	166
	101.8	288	946	830
	98.7	736	1786	9077
	95.4	1738	5116	$> 10^4$
Kr + NiA+D	98.6	20	304	21
	97.3	37	314	37
	95.6	55	343	58
	93.8	87	409	102
	91.9	164	737	292
CO ₂ + NiA+D	122.5	15	190	14
	119.8	24	201	23
	117.0	48	235	48
	114.0	112	373	152
	111.1	246	617	983
	108.1	665	1273	$> 10^4$